UNIVERSITY OF BERGEN

Department of Geoscience

MASTERS THESIS

The topographic evolution of post-Caledonian landscapes in the inner Nordfjord, SW-Norway

New insights from AFT dating and thermal history modelling

Author: Ferdinand Mayer-Ullmann

Supervisor: Prof. Joachim Jacobs

Co-supervisor: Åse Hestnes

Co-supervisor: PhD. Hallgeir Sirevaag

August 24, 2021

Abstract

The topographic evolution of the present-day mountains of western Norway is not completely resolved. Long after the breakup of the Caledonides, the mountains along the passive continental margin of Norway remain high, with deep incising valleys and low relief surfaces at the top. The origin of this post-Caledonian landscape is cause of controversy. The ongoing debate revolves around two endmember hypotheses, where the established hypothesis suggests peneplanation at the end of the Mesozoic, with subsequent uplift. A newer hypothesis argues that the same observations can be explained by simply long-term slow erosion, glacial flattening and isostatic rebound. Both these hypotheses are founded on observations ranging from offshore sedimentary depositions, structural analysis, geophysical models and thermochronological data. Despite the multi-disciplinary approach, the interpretations of evidence remain ambiguous and there is increasing evidence that the evolution of the passive continental margin might even be more complex than either hypotheses leave to believe. This study presents the first steep vertical profile from the poorly surveyed inner Nordfjord area and provides new apatite fission track data and evidences for active fault displacement, even on less fractured mountain flanks, as well as new insights into post-Caledonian topographic evolution. The timing of faulting is closely tied to the North Sea Rifting and the development of brittle features have been affected by intrabasement ductile precursor structures. Inverse modelling of time-temperature paths indicate a low relief surface at the end of the Mesozoic. However, it remains unclear at which elevation said surface resided. During the Cenozoic this surface was further worn down and deep valleys were carved out. The results from this study indicate that the passive continental margin of western Norway tells a very complex story that most likely cannot be fully explained by either of the two endmember hypotheses. The methods used in this study and especially the steep profile allow detailed insights into the thermal and structural evolution of the upper most crustal level. Higher resolution in sampling, together with combining multiple thermal dating techniques, would increases our understanding of the Norwegian passive continental margin even further.

Acknowledgment

After compiling my thesis for the first time, I realized – creating a piece of work like this is simply not possible, without the remarkable assistance of all my friends and colleges that never hesitated to help me. First and foremost I'd like to thank Prof. Joachim Jacobs, who right after arriving in Bergen, led me towards the right direction. I'd like to thank him also for his advice and the opportunities he offered me, that filled my stay with plenty of geological content. I'd also like to thank Åse Hestnes. She introduced me to the geology of Norway during an impeccable field trip to Nordfjord. She also aided me with countless suggestions and corrections and I'm so thankful that I could be a part of her project, funded by VISTA. I'd also like to thank Hallgeir Sirevaag for showing me and helping me with the thermochronological software, hardware and digital modelling that I encountered during my work. I am especially grateful for his swift answers to my questions, even though he was occupied with more important matters. Without the supervision and the invaluable insights into scientific work and discussion, a thesis like this is simply impossible. So, thank you, tusen takk and dankeschön to all of you. Over hundred pages of thesis include a lot of text and I am incredible grateful for everyone that took their time to patiently correct my chapters. That includes not only my supervisors but also Hannes Lauter, who read almost all chapters even though geology is not even part of his expertise, but just because he is a dear friend. I also thank Stefanie Handl for her enthusiasm in my thesis and her comments and corrections. Without the help of my parents this endeavour would have not been possible. While Norway is a great place to be during a pandemic, I am thankful for my parents calling me, when I didn't call them on a regular basis, and reminded me that I still have a family in another country. I also thank them for their unasked financial support, that helped me out when student jobs couldn't.

Finally, I'd like to thank my friends that I had the pleasure to meet and spent my recreational time with, during my stay. I especially want to thank Chanakan Boonnawa and Simon Lefevere for our everyday morning-coffee, where we would have intense discussions about geology, home-brewing, cooking, irish music and all the other good things in life.

F.M.U

Contents

List of Figures

List of Tables

List of abbreviations

AFT - Apatite fission track

FT - Fission track

MTL - Mean track length

Tt- - Time-temperature

PCM - Passive continental margin

UHP - Ultra-high pressure

MTFZ - Møre-Trøndelag Fault Zone

NSZ - Nordfjord Shear Zone

SSZ - Sandane Shear Zone

GSZ - Geiranger Shear Zone

NSDZ - Nordfjord-Sognefjord Detachment Zone

BASZ - Bergen Arc Shear Zone

HSZ - Hardanger Shear Zone

LGF - Lærdal-Gjende Fault

MCC - Metamorphic Core Complex

AHe - Apatite helium

EDM - External detector method

TEM - transmission electron microscope

PAZ - partial annealing zone

FCT - Fish Canyon Tuff

DUR - Durango

TINT - track-in-track

TINCLE - track-in-cleavage

TINDEF - track-in-defects

Chapter 1

Introduction

Mount Skåla is 1848 m a.s.l. and is the highest mountain in Norway with its base at sea level. It is part of the high elevation and low relief surfaces of the post-Caledonian landscape, that dominates SW-Norway. Despite a long-lasting and heated debate about the origin of this high elevation topography, the tectonomorphological evolution of the post-Caledonian mountains remains incompletely resolved (e.g. Nielsen et al., 2009; Gabrielsen et al., 2010). The debate revolves around two end-member hypotheses that try to explain the topographic evolution of the passive continental margin of Norway: 1) a Late Mesozoic peneplanation of the passive margin with subsequent Neogene uplift (e.g. Gabrielsen et al., 2010) or 2) a continuous slow erosion of a high elevation, Cenozoic glacial flattening and isostatic rebound (e.g. Nielsen et al., 2009). Even though both hypotheses describe a different topographic development, both are based on the same multi-disciplinary observations that have been interpreted in different ways. In previous apatite fission track (AFT) studies in Norway, widely spaced thermochronological data are interpreted to show domal uplift of SW-Norway during the Neogene (Rohrman et al., 1995). Later studies along the Møre-Trøndelag Fault Zone show that the earlier interpreted domal uplift might rather be the result of fault block movement along the North Atlantic passive margin (Redfield et al., 2004, 2005). Extensive AFT studies in the Bergen and Hardanger area showed that thermal ages are significantly offset by fault block displacement (Johannessen et al., 2013; Ksienzyk et al., 2014). This faulting is connected to the two North Sea Rift Phases during the Permo-Triassic and Late Jurassic (Fossen et al., 2021), making the Norwegian passive margin evolution arguably more complex than the two opposing hypotheses leave to believe (Johannessen et al., 2013; Ksienzyk et al., 2014). The main issue for interpretation of the passive margin is the wide spacing and altitude of analyzed samples. While the continuous research of others steadily increased the number of data (Hendriks et al., 2007), hardly any thermochronological studies have been conducted in the area south of the Møre-Trøndelag Fault Complex and north of Sognefjord,

around the Nordfjord area, leaving a sizable gap in the available data set.

In this study, 19 samples will be analyzed using Apatite Fission Track and inverse modelling to reconstruct the thermal history of the inner Nordfjord area. The samples include one ca. 1800 m high vertical profile at Skåla to draw more detailed conclusions on exhumation through time and five additional samples from the area around. Additionally, remote sensing will be used to inspect lineaments in the area, which ought to help in the interpretation of fault systems and their influence on inferred ages. The aim of the study is to reconstruct a detailed thermal history of the inner Nordfjord area and to evaluate the influence of faulting in the topographic evolution. The obtained data will culminate in a cohesive model that that outline the post-Caledonian topographic evolution of the inner Nordfjord area. This model will then be compared with previous hypotheses, to test if they can stand newly acquired data and its implications on the evolution of the Norwegian passive continental margin.

1.1 Study area

The study area is located in the inner Nordfjord of Western Norway and covers an area of about 1750 km² (Fig. 1.1). The largest towns in the area are Sandane (2446 inhabitants) and Stryn (2553 inhabitants) (SSB.no). The approximately E-W striking Nordfjord dominates the study area. Several side valleys cut into the mountain with steep flanks on both sides, most notable the major N-S striking Oldendalen and the NW-SE striking Lodalen adjacent to mount Skåla. Skåla is with 1848 m asl. the highest mountain in the study area. It is also the mountain where the vertical profile is located (Fig. 1.1). In the south-eastern part of the study area, we find the large Jostedalsbreen that feeds into several minor glaciers mostly perpendicular to the main valleys. The snow line starts around 1100 and 1500 m asl. (depending on wind, Dahl and Nesje, 1992) meaning that even Skåla is partially covered by snow all year round.

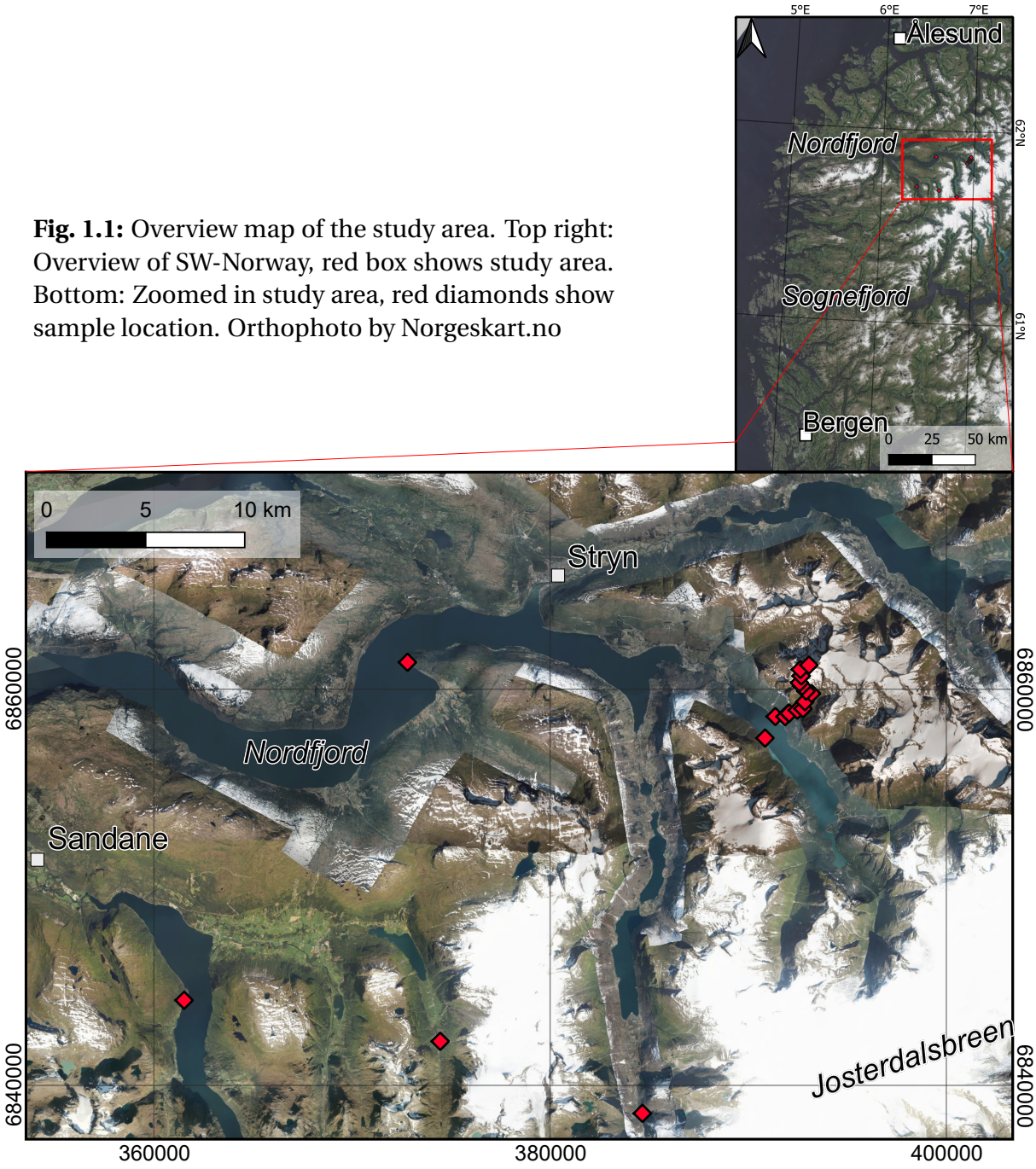

Fig. 1.1: Overview map of the study area. Top right: Overview of SW-Norway, red box shows study area. Bottom: Zoomed in study area, red diamonds show sample location. Orthophoto by Norgeskart.no

Chapter 2

Geological background

As part of the Baltica, SW Norway has a long and complex geological history and has been part of at least two supercontinents. The study area itself is considered part of the central Western Gneiss Region (WGR) – a metamorphic window of the precambrian baltic basement, that is superimposed by later Caledonian Allochtones (Wiest et al., 2021). The Caledonian orogeny stretches over 1500 km from Stavanger in the south to the Barents Sea in the north (Corfu et al., 2014; Gee et al., 2008). This chapter is a short overview of the geological history of SW-Norway from Precambrium to Caledonian, continuing with the post-caledonian collapse and rifting.

2.1 Pre-Caledonian Evolution

The assemblage of the Baltic shield took place between 1.8 – 1.5 Ga in three major stages while it was situated at the edge of the supercontinent Columbia (Roberts and Slagstad, 2014). With the Sveconorwegian orogeny (1.1-1.0 Ga; Bingen et al., 2005), Fennoscandia finalizes its accretion during the amalgamation of the subsequent supercontinent Rodinia, forming a part of the Greenvillian orogeny (Bogdanova et al., 2008; Roberts and Slagstad, 2014). Zircon U-Pb ages from the gneisses show an upper intercept of ca. 1.6 Ga and a metamorphic age of 1 - 0.9 Ga, the latter one probably related to the Sveconorwegian (Skår and Pedersen, 2003; Røhr et al., 2013). The Baltic shield is generally linked to Laurentia, as they form a common boundary in most supercontinents (e.g. Torsvik, 2003; Torsvik and Cocks, 2005; Zhang et al., 2012). After the assembly of Rodinia, a long period of attempted continental rifting (~200 Ma) took place, eventually leading to the opening of the Iapetus ocean between Baltica and Laurentia (Jakob et al., 2019) that would eventually be closed again with the onset of the Caledonian orogeny.

2.2 Caledonian Orogeny

The Caledonian Orogeny describes the last major mountain building event in Scandinavia (Soper et al., 1992). In Norway, the orogeny is visible in E-vergent thrusts or nappes derived from allochthonous Baltoscandian rocks, but also material from the oceanic terranes, derived from the Iapetus Ocean, and even exotic Laurentian rocks (Gee et al., 2008). This process comprises several events from the Late Cambrian to the Early Devonian, resulting in the closure of the Iapetus Ocean and the development of the Scandian mountain range. Roberts (2003) reviews the chronology of the Caledonian in more detail. The study distinguishes between four different compressive/transpressive stages and a following Post-Caledonian orogenic collapse in the Early Devonian. The Finnmarkian (Late Cambrian) and the Trondheim (Early Ordovician) period involved subduction of oceanic crust, and the accretion of microcontinents. This happened while Baltica rotated anticlockwise to face Laurentia. According to Roberts (2003), seafloor spreading peaked during the Cambrian and the first accretionary event (Finnmarkian) took place. The Taconian (Mid-Late Ordovician) describes arc-accretion of the Iapetus arcalong the Laurentia Margin. This led to ophiolite obduction prior to the Laurentia-Baltica collision. The Scandian (Mid Silurian – Early Devonian) is marked by rapid subduction of the Baltica margin beneath Laurentia to a depth of at least 120 km to reach UHP conditions and ultimately leading to an oblique continent-continent collision between Baltica and Laurentia. The collision had an NW-SE direction from today's continental orientation (Corfu et al., 2014). The Scandian is therefore a major thrusting event during the Caledonian Orogeny emplacing tectonic nappes onto Precambrian sediments and basement. These Caledonian Nappes can be grouped into Lower, Middle, Upper and Uppermost Allochthon (Gee et al., 2008, after Gee et al., 1985) and represent the rocks from the Laurentia-Baltica convergence (Gee et al., 2008; Roberts, 2003) with their respective setting. Neoproterozoic to Silurian Metasediments formed a sliding horizon i.e. decollément, over which the Caledonian allochthonous thrust nappes have been translated and now rest upon (Fossen and Dunlap, 1998; Gee et al., 2008).

2.3 Post-Caledonian evolution

After the Caledonian Orogeny in the Early Devonian, a series of extensional deformation phases and sinistral transtension took place (e.g. Fossen, 2010). Roberts (2003) points out that the Late Caledonian sinistral strike-slip movement is also recorded for the British Isles, Canada, New England and Eastern Greenland, implying that there was a significant relative plate movement immediately after the suturing of Baltica.

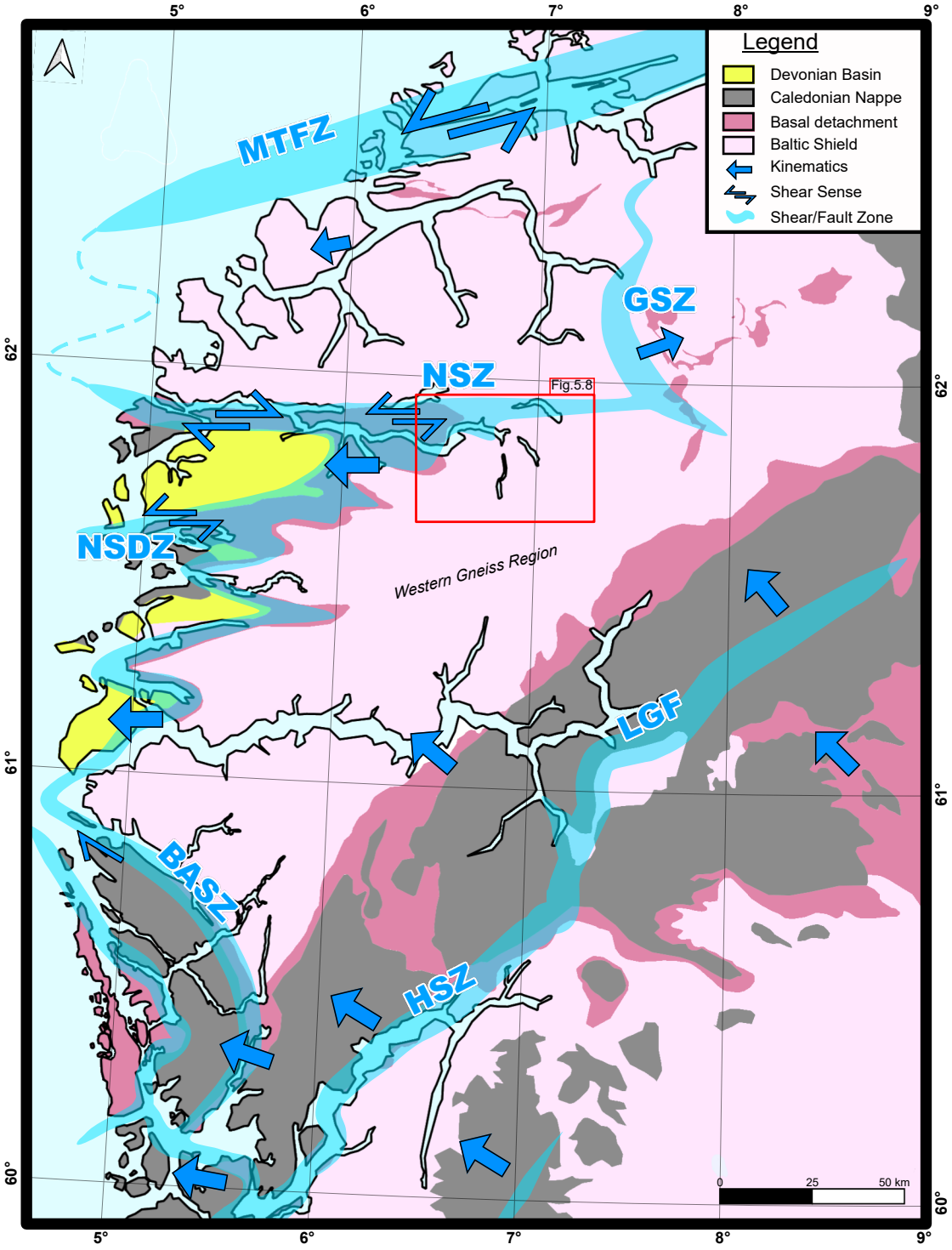

Fig. 2.1: Shear- and Detachment Zones in SW-Norway. MTFZ=Møre-Tøndelag Fault Zone; NSZ=Nordfjord Shear Zone; NSDZ=Nordfjord-Sognefjord Detachment Zone; LGF=Lærdal-Gjende Fault; BASZ=Bergen Arc Shear Zone; HSZ=Hardanger Shear Zone; Study area highlighted with a red square. Redrawn and simplified after Fossen (2010); Wiest et al. (2020, 2021); Bedrock map from the Geological Survey of Norway (NGU)

2.3.1 Devonian extensional stages

At the maximum of the Caledonian collision, the mountain range in southwestern Norway built up to possibly 8 km hight comparable to the Himalayas today (Gee et al., 2008). The best explanation for the transition from collision to post-orogenic collapse and extension is the onset of plate-scale divergence, as a result of sinistral transtension between Baltica and Laurentia (Fossen, 2000; Krabbendam and Dewey, 1998; Butler et al., 2015). Models show that coeval with the collapse, slab eduction and delamination from the retreating slab of subducted plate (proside) took place. The UHP material was then thrusted upwards along a subduction channel and rapidly exhumed, as can be observed in the UHP zone just N and NW of the study area (Hacker et al., 2010; Duretz et al., 2012; Bottrill et al., 2014; Butler et al., 2015). Age constraints from $^{40}Ar/^{39}Ar$ and U/Pb dating, as well as sediment records, indicate that thrusting of nappes onto Baltica ceased ~410 Ma and the post-orogenic extensional deformation started shortly after, at ~400 Ma (Fossen and Dunlap, 1998; Fossen, 2000, 2010; Young et al., 2011). Some extension may have started syn-orogenic, but the major extension stages took place post-orogenic (Fossen, 1992, 2000). The stages can be separated into three modes (Fossen, 1992):

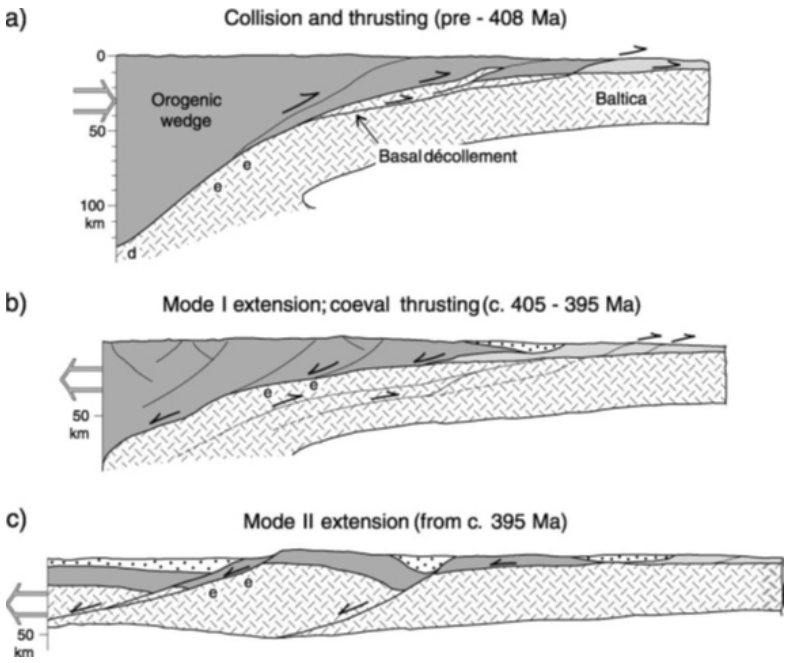

Fig. 2.2: Simplified WNW-ESE profiles showing contractional and extensional development of southern Scandinavian Caledonides. a) Collission phase b) Stage of initial orogenic collapse and backsliding/low-angle decollement, e = Eclogites, dotted = Devonian sediments/formation of Devonian basins; c) Main crustal collapse stage with steeper down-W shear zones cutting earlier, extensional detachments. The last phase of extension might have continued at least into Late Devonian, possibly until Early Carboniferous. Roberts (2003); based on Fossen (2000) and Fossen and Dunlap (1998)

Mode I: Backsliding of the orogenic wedge

The Scandian thrusting structures are overprinted by subsequent backsliding during post Caledonian extension. There is clear evidence for large-scale overthrusting for hundreds of kilometres caused by the transport of Laurentia derived nappes over the décollement with top-to-the-ESE shearing (Fossen, 2000). However, these were overprinted and locally obliterated by a reverse movement of top-to-the-WNW simple shearing with a slightly weaker metamorphic imprint (Fossen, 1992, 2000). This Mode I extension can be seen as a translation of the orogenic wedge i.e. backsliding. The reactivation of the basal thrust zone resulted in a low-angle extensional shear zone (Fig. 2.2 b) Fossen, 2000). The removal of overburden during backsliding induced rapid cooling of the upper crust into the brittle regime within ~10 Myr after the onset of extension, progressing towards the NW (e.g. Fossen, 2000). The Mode I extension has been estimated to roughly 20-36 km (Fossen and Holst, 1995). Backsliding allowed for rapid removal of massive amounts of overburden, revealing a large UHP region (Hacker et al., 2010).

Mode II: Crustal Collapse

After the low-angle back-sliding (Mode I), several steeper extensional shear zones develop and extend through the Caledonian nappe (Fig. 2.2 c) Fossen, 1992, 2000, 2010). Seismic data even reveals that the Mode II shear zones extend even further and affected the Proterozoic basement (Fossen and Hurich, 2005). Mode II extensional shear zones are W and NW dipping with km-scale displacement. Examples of major NW-dipping Mode II shear zones are the Hardanger Shear Zone (HSZ) (Fossen, 2010) and Nordfjord Shear Zone (NSZ) (Labrousse et al., 2004). Coastal parallel shear zones (W-dipping) are the Bergen Arc Shear Zone (BASZ) and the Nordfjord Sognefjord Detachment Zone (NSDZ) and dip in a more curved map pattern (Fossen, 2010). The NSDZ is the largest (in terms of strain, offset and thickness) Mode II extension in western Norway (Fossen, 2010). The NSDZ probably connect with the Møre-Trøndelag Fault Zone (MTFZ) in the north and with the BASZ in the south (Fig. 2.1 Fossen, 2010; Fossen et al., 2017). The NSDZ is a 5-6 km thick mylonitic shear zone with a consistent top-to-the-west sense of shear (Fossen, 2000; Fossen et al., 2017). The estimated displacement is about 50-100 km (Norton, 1987). Even though the present-day dip is rather shallow (~5-10°), the initial dip may have been steeper (Fossen, 2000, 2010). The NSDZ defines several fold structures, with gently west-plunging fold axes and subvertical axial surfaces. The resulting scoop-shaped supradetachement basins host Devonian sandstones (Fossen, 2010). The upright folding affects not only Proterozoic and Caledonian structures but also Devonian sediments, indicating that N-S shortening must have taken place before, during and after the deposition i.e. Mode II extension (Fossen et al., 2017; Krabbendam and Dewey, 1998). Krabbendam and Dewey (1998) interpret this extension as a result of partially partitioned

transtension in the Western Gneiss Region (WGR) . This transtension could be a result of sinistral shearing along the ductile precursor structures of the ENE-WSW striking MTFZ and oblique plate divergence between Laurentia and Baltica. Krabbendam and Dewey (1998) show that the transtensional angle increases towards the MTFZ. The transtension is also is the proposed mechanism for the exhumation of UHP lithologies juxtaposing them to the Devonian sandstones of the hanging wall of the NSDZ (Fossen et al., 2017; Krabbendam and Dewey, 1998; Labrousse et al., 2004; Hacker et al., 2010). According to Hacker et al. (2010), the main top-to-the-W extensional deformation took place at crustal levels from 410 – 400 Ma to 392 – 388 Ma. In a recent study, Wiest et al. (2021) showed that different basement segments of the Caledonian orogenic infrastructure were moved independently from each other. This movement of crustal blocks occurred asynchronously. The temporal break aligns with metamorphic discontinuities across sinistral transfer shear zones, e.g. NSZ in the study area (Fig. 2.1). The youngest segment is recorded in the central WGR (which includes this study area) with a minimum absolute age of 375 Ma , based on a variety of geochronological data (Wiest et al., 2021). As a result of the extension, the WGR crops out in dome-like structures, that can be described as metamorphic core complexs (MCC). The UHP zone just north of the NSDZ is the largest MCC of an array of MCCs along the west-Norwegian coastline (Wiest et al., 2021; Labrousse et al., 2004). The transition from Mode I to Mode II is likely due to the exhumation of the décollement zone in the hinterland. This would have lowered the dip of the décollement and (vertically) rotated it out of a position suitable for Mode I extension. This in return favours pure shear (Mode II) extension and brings the décollement into a more horizontal position (Fossen, 2000). According to Fossen et al. (2017) most or all of these Mode II shear zones reached the surface as brittle fault zones, generating Devonian continental basins. However, most of these basins have been eroded and only basins in the hanging wall of the NSDZ remain.

Mode III: Brittle Extension

Mode II extension was followed by brittle faults with semi ductile elements (Fossen, 2000). Mode III structures are usually high-angle faults with striated epidote-coated surfaces forming at depths close to the brittle-ductile transition. This depth was not equal across SW-Norway, due to the progressive backsliding and related rapid cooling, Mode III deformation started earlier in the SE. Mode II structures may have been still active in the NW while Mode III structure started to form in the SE (Fossen, 2000). Mode III features are consistent with an NW-SE extension, though change to more E-W extension in the NW, maybe due to slip partitioning along the MTFZ (Krabbendam and Dewey, 1998; Fossen, 2000). The largest of Mode III structures is the NE-SW trending Lærdal-Gjende Fault (LGF) that dips with 15 – 35° to the NW (Fossen et al., 2017). The time of the ductile-brittle transition was dated to 395 Ma with U/Pb in the Bergen area (Fossen, 2000) in order to determine the age of Mode III structures.

2.3.2 North Sea Rift Phases

Two main rift phases took place in the North Sea area after the Devonian extension. The first in the Permo-Triassic period and a second one in the Middle to Late Jurassic, both contributing to the opening of the North Sea and marking the onset of continental margin evolution along the soon-to-be North Atlantic (Færseth, 1996; Gabrielsen et al., 2010; Ksienzyk et al., 2014, 2016; Fossen et al., 2017). The Permo-Triassic rift basins are described as mostly N-S trending half grabens and a full graben system (Færseth, 1996). These encompass, namely the Horda Platform and Åsta Graben at the eastern part of the northern North Sea. Maximum Permo-Triassic stretching and fault activity is located at the Horda Platform (Færseth, 1996). The rift system generally shows steeper faults that merge with curved extensions of ENE-WSW trending Devonian Mode II shear zones (e.g. HSZ) at depth, brittlely reactivated during rifting (Færseth, 1996; Fossen et al., 2017; Wiest et al., 2020). Onshore observations show that Devonian NE-SW trending faults have been overprinted by N-S trending faults and dykes of Permo-Triassic age (e.g. Fossen and Dunlap, 1999), indicating a change from Devonian NW-SE to an E-W extension during the Permian (Fossen et al., 2017). Middle to Late Jurassic rifting is constrained by the Shetland plateau at its western flank and behaved more localised, mainly to the Jurassic Viking Graben in the north-western part of the North Sea and a south-western branch (Moray Firth Basin). These younger basins are NNE-SSW striking, partly overlapping Permo-Triassic basins. The extension of Jurassic basins increases towards the north until it eventually encompasses the width of the basin north of 61°N (ca. 200 km, Færseth, 1996). Faults of the first rift phase were reactivated (Færseth, 1996) as well as intra-basement shear zones that left weaknesses in the crystalline fabric. This allowed for a variety of E-W and NE-SW trending faults, while the extension keeps E-W directed (Reeve et al., 2015; Osagiede et al., 2020).

2.3.3 Onshore response to rifting

Various studies infer repeated fault reactivation in established fault zones (e.g. Lærdal-Gjende Fault (LGF), NSDZ, MTFZ) for both rift phases along the Norwegian margin (e.g. Torsvik et al., 1992; Fossen and Dunlap, 1999; Ksienzyk et al., 2014, 2016; Fossen et al., 2017), showing clear Permian to Triassic (~280 – 230 Ma) and Late Jurassic (~165 – 140 Ma) activity (Fossen et al., 2017, 2021). Recent K-Ar data by Fossen et al. (2021) suggest that both rift phases initialized on a wide area, also affecting onshore structures and only localizing to the offshore realm with progressing rifting. The effects onshore of rift phases are, however, still more pronounced in coastal areas, exhuming rocks close to the surface in the Jurassic. The continental interior, on the other hand, was less affected and experienced continuous slow

exhumation, eventually surfacing during the Cenozoic (Ksienzyk et al., 2014).

2.3.4 Opening of the North Atlantic

Contemporary with Permo-Triassic and Jurassic rift events, the North Atlantic started to rift as well driven by the breakup of Pangea (Doré et al., 1999; Faleide et al., 2008). Basins developed northwards during the Jurassic. The North Atlantic rifting is an northern extension of the North Sea rift with the reactivated MTFZ acting as (dextral) transfer fault (Doré et al., 1999; Redfield et al., 2004). Crustal extension during the earliest Cretaceous is also responsible for major crustal thinning, that propagated northwards (Faleide et al., 2008). Complete seafloor spreading and continental break up along the NW European Atlantic margin likely did not commence before 53 Ma (Doré et al., 1999; Faleide et al., 2008).

2.4 Topographic evolution

The evolution of present topography in Norway is a highly controversial subject. This discussion combines observations in geochronology, structural geology, geophysics, geomorphology, sedimentology etc. which makes this not only very interesting, but also challenging to aquire full understanding of the complexity of the problem.The main observations are accordant summits and low relief surfaces at high elevations in combination with deeply incised valleys across western Norway (e.g. Japsen et al., 2018). The established hypotheses include peneplanation by the end of the Cretaceous with subsequent uplift in the Cenozoic (e.g. Gabrielsen et al., 2010). However, Nielsen et al. (2009) suggested that the modern topography is the result of consistent slow erosion, climate and glaciation in combination with isostatic re-equilibrium. A brief overview of the debate is given below (Fig. 2.5):

2.4.1 Peneplanation hypothesis

The first mention of elevated low relief surfaces as a result of peneplanation was made by Reusch (1901) and has been proposed as a result of Neogene uplift (e.g. Japsen and Chalmers, 2000; Mosar, 2003). Since low-relief surfaces along passive margins are not unique to Scandinavia, a general explanation of the evolution of these landscapes is required, which rules out glaciation-based mechanisms (e.g. Chalmers et al., 2010; Osmundsen and Redfield, 2011).

Gabrielsen et al. (2010) conclude that changes of the ENE-SWS-topographic elevation gradients (i.e. hillslopes) describe three different stages that can be identified and solidified them with thermochronology studies. They provided a model for the topographic evolution

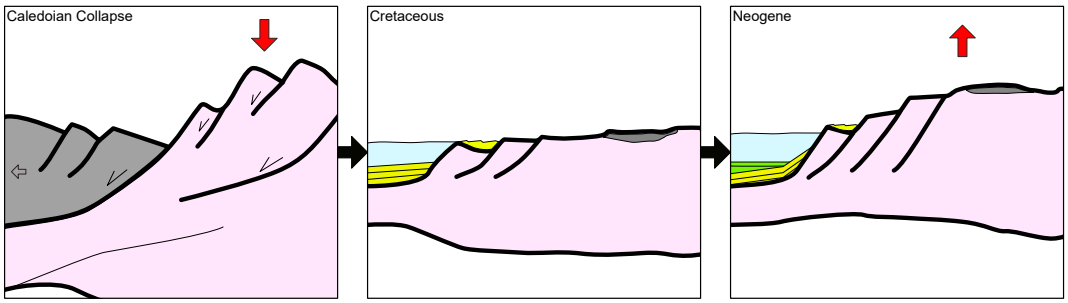

Fig. 2.3: Simplified topographic evolution following the peneplanation hypothesis (Gabrielsen et al., 2010). Left: The Devonian collapse and complete obliteration of Caledonian orogenic heights as a consequence of Mode I+II extension. Middle: Peneplanation during the Cretaceous and reduction of relief to local sea level and sedimentation in basins. Crustal thinning due to rapid erosion. Right: Neogene tectonic uplift that causes Cenozoic sediment to truncate older sediment and lifts low relief surfaces to modern heights. The red arrow indicates uplift/denudation. Grey=Caledonian Nappes; Pink=Baltic Shield; Yellow=Devonian to Cretaceous sediments; Green=Cenozoic sediments

over the past 400 Ma for these three stages: Stage 1 (Devonian – Late Permian): describes an ongoing collapse of the orogen even before the collision ceased. Together with erosion, this reduced the Caledonides in height from approx. 8 to 9 km down to 500 m whitin 77 Myr. This is in agreement with Allen (2008) a reasonable lifespan of an orogen of this size. Stage 2 (Late Triassic – Late Cretaceous): was dominated by uplift, assumed to be caused by rifting in the North Sea and therefore to be seen as rift-flank uplift (e.g. Rohrman et al., 1995; Mosar, 2003). At the end of the Cretaceous, the topography was completely removed down to sea level (e.g. Doré, 1992), resulting in a peneplane (see Fig. 2.3 and 2.5). Stage 3 (Cenozoic): uplift took place again, in the south-central parts of Norway. During the Neogene, the maximum elevation ceased to increase while the slopes increased and westward flowing rivers incised. The trigger for this uplift may have been intraplate compressive stress, diapirism or underplating (Doré et al., 1999).Gabrielsen et al. (2010) interpreted upper Pliocene and older sequences on the continental shelf that are tilted away from the mainland as evidence for a recent uplift event of south Norway during the Pliocene - Pleistocene. Sømme et al. (2013) used the volume of point source depocentres along the Norwegian margin to make predictions about hinterland topography, suggesting that by the Late Jurassic the maximum relief was about 1.6 km high (Fig. 2.5). By Cretaceous times, the absence of coarse siliciclastic sediments (i.e. only mud deposition offshore), as seen in wells and seismic data offshore, suggests a significantly reduced size and relief of the onshore drainage catchment with a maximum elevation of ~0.5 km Sømme et al. (2013). Most recently, Japsen et al. (2018) proposed even two peneplains in southern Norway (Hardangervidda). Based on previous studies and new thermochronological data , they propose a sequence of post-breakup uplift and erosion events

resulting in a tilted (onshore) Mesozoic peneplain and a subhorizontal Miocene erosion surface that has been uplifted during the Pliocene to create modern accordant summits. The main counterargument however is that the same set of observations can be explained simpler without the necessity of an Neogene uplift and the poorly regarded effect of glaciation and isostacy along the passive margin (Leighton, 2007; Nielsen et al., 2009).

2.4.2 ICE - hypothesis

Nielsen et al. (2009) sparked a passionate debate about the evolution of elevated landscapes in Norway. They present a detailed interdisciplinary approach to explain elevated low relief surfaces along the passive margin solely with glacial erosion, isostatic rebound and climate. Nielsen et al. (2009) emphasize that these triggers alone can explain the modern topography and that additional tectonic uplift during the Cenozoic (most often cited as Neogene) (e.g. Donelick et al., 1999; Japsen and Chalmers, 2000; Mosar, 2003) is not necessary.

Nielsen et al. (2009) point out, that a negative Bouguer anomaly indicates that the crustal root of the mountain range is still intact. That would contradict the assumption of peneplanation during the Mesozoic, as this hypothesis implies that the mountain root has been eroded to create a peneplain. Instead, Nielsen et al. (2009) propose that climate-induced erosion e.g. by glaciation, accompanied by isostatic re-equilibrium, due to unloading and following basin sedimentation on the adjacent passive margin, was enough to create the present-day topography (ICE-hypothesis – Isostasy, Climate, Erosion). As they also point out, several other processes could satisfy the observation, e.g. magmatic underplating to restore the crustal root, though they explain that those processes either have not been ob-

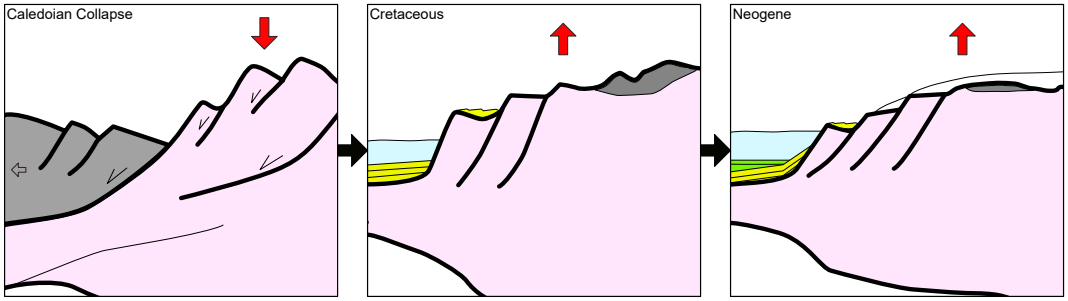

Fig. 2.4: Simplified topographic evolution following the ICE Hypothesis (Nielsen et al., 2009). Left: The Devonian collapse of the Caledonian orogeny, however, the topography is not completely obliterated. Middle: Slow and ongoing erosion fills sediment basins and leads to slow and steady uplift. Left: Climate and glaciation flattens high elevation topography and induces isostatic uplift. The red arrow indicates uplift/denudation. Grey=Caledonian Nappes; Pink=Baltic Shield; Yellow=Devonian to Cretaceous sediments; Green=Cenozoic sediments

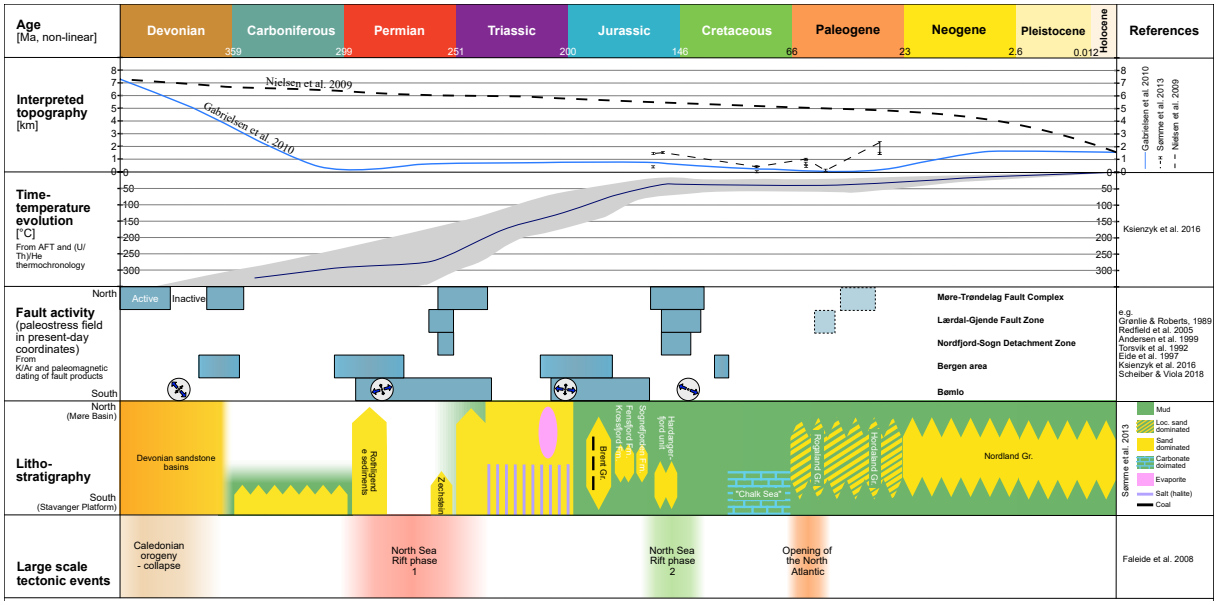

Fig. 2.5: A shortened summary of studies regarding landscape evolution in Norway (figure by courtousy of Åse Hestnes)

served or do not apply to the Caledonides. Also, they propose that the most recent uplift along the Norwegian coastline can solely be explained by a post-glacial rebound and that another Cenozoic uplift event is not necessary. Indubitably, Nielsen et al. (2009) caused a large backlash and defenders of the established Peneplanation hypothesis pointed out crucial oversights in Nielsen et al. (2009)'s conclusion (e.g. Lidmar-Bergström and Bonow, 2009; Chalmers et al., 2010; Gabrielsen et al., 2010; Hall et al., 2013). Further studies of offshore sediment volumes show that erosion from the Fjords can only account for about 35-55% of the volume deposited offshore during the late Pliocene and Quaternary (Steer et al., 2012). That means that the rest is accounted to periglacial erosion at high elevation (Steer et al., 2012). The suggested mechanism for periglacial erosion that creates flat high elevation surfaces is the so-called glacial buzzsaw (Pedersen and Egholm, 2013). Modelling efforts show that glacial erosion at high elevation could have prepared the surface in previous glaciation cycles. Once the surface is flattened down to the local equilibrium line altitude (ELA), the erosion rate decreases while accumulation increases. This allows for high erosion in valleys, resulting in flat high elevation surfaces incised with glacial valleys (Pedersen and Egholm, 2013; Egholm et al., 2017). Later studies present models that combine dynamic uplift in addition to the isostatic rebound along the coastline to explain tilted sediments (Pedersen et al., 2016). A Mesozoic peneplain in combination with tectonic uplift is rejected in favour of mainly climate-driven glacial erosion and subsequent isostatic rebound as an explanation for modern topography. Many critics argue, however, that the hypothesis should be apliable for other passive margins as well, like SW-Africa and should not represent a unique case (e.g. Chalmers et al., 2010).

2.4.3 Previous thermochronological studies on the Norwegian passive continental margin

One of the first AFT studies in SW-Norway describes a multiphase evolution of the passive continental margin (PCM, Rohrman et al., 1995). This study suggests first Triassic-Jurassic exhumation and rift flank uplift and later in the Neogene, a dome-shaped exhumation surface, showing older ages at the coastline and younger ages in the Norwegian interior (Rohrman et al., 1995). A compilation of available fission-track data points to a similar conclusion with older ages at the coastline. Additionally, mean fission track lengths tend to be longer at the coastline and shorter towards the interior, indicating a slower exhumation in the centre of the dome (Hendriks et al., 2007). Interestingly, different conclusions have been drawn from the same set of thermochronological data resulting in vastly different post-Caledonian evolution hypotheses (e.g. Gabrielsen et al., 2010; Nielsen et al., 2009; Japsen et al., 2018). Thermal modelling in a more recent study showed that coastal regions in western Norway have been exhumed close to surface level by Middle Jurassic, while clastic sediments have been deposited in the newly developed basins (Sømme et al., 2013; Ksienzyk et al., 2014). Subsequently resurfaced areas were buried by a thin sediment cover, resulting in mild reheating (30 – 50 °C) in connection with cretaceous transgression (Doré et al., 1999; Ksienzyk et al., 2014), followed by renewed cooling in the Cenozoic (Ksienzyk et al., 2014). Inland samples were not exhumed with the same magnitude during the Jurassic and instead continued slow cooling until they eventually resurface in the Cenozoic (Ksienzyk et al., 2014). However, denudation undoubtedly intensified with severe Plio-Pleistocene glacial erosion (Solheim et al., 1996; Doré et al., 1999; Japsen and Chalmers, 2000).

Simplified models for the evolution of PCMs aim to explain the steep escarpments and elevated low-relief surfaces, typical for many PCMs (Fig. 2.6, Wildman et al., 2019). Since each model describes a different morphological evolution, they also show different AFT transects from coastline to continental interior (Fig. 2.6E). The Downwarp model (Fig. 2.6A) represents an palaeoplain, with the escarpment as a coastal erosion surface and overall limited fautling (Ollier and Pain, 1997). However, this models neglect the isostatic response of unloading of the escarpment and are often viewed critically (e.g. Gallagher and Brown, 1999; Wildman et al., 2019). Alternatively, the Scarp retreat model (Fig. 2.6B, Gilchrist and Summerfield, 1990) and Pinned divide model (Fig. 2.6C, Kooi and Beaumont, 1994) describe an initial escarpment along a syn-rift normal fault. Deudation is focused on the frontal escarpment, were the relief is high. This results in younger AFT ages at the coast than inland (Fig. 2.6E). The difference between the Scarp retreat and the Pinned divide model is that latter includes a drainage divide that leads to seaward fluvial incisions (Gallagher and Brown, 1999). Various studies showed that exhumation along the norwegian PCM might have been heavily

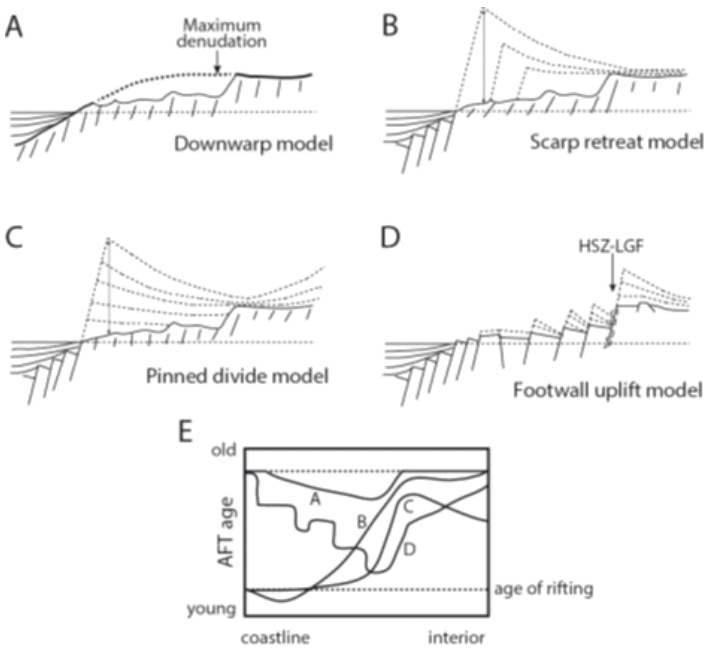

Fig. 2.6: Different landscape evolution models for passive margins. A-D shows the different denudations patterns, E shows the expected AFT-ages from coastline to the interior. Note that model D takes faulting into account. (from Johannessen et al. (2013) and modified after Gallagher et al. (1998))

influenced by faults and tectonic block movement, displacing ages on a short distance (Redfield et al., 2004; Leighton, 2007; Johannessen et al., 2013). An important detail neither the ICE- nor the peneplain hypothesis take into account (Ksienzyk et al., 2014). In a similar study to this thesis, Johannessen et al. (2013) analysed several steep profiles in the inner Hardangerfjord using AFT, concluding that high elevation surfaces are most likely of Cenozoic age and therefore do not derive from a rejuvenated peneplain. Recent cooling of samples of lower elevation along their profiles is attributed to glacial erosion, which aligns with results from Steer et al. (2012). However, Johannessen et al. (2013) also emphasize, that ages were seriously affected by fault-related offset and suggest a conceptual model for PCM evolution that takes the importance of fault block movement into account (Fig. 2.6D). Ksienzyk et al. (2014) show fault-related offset also in a detailed study in the Bergen area and conclude that the evolution of the passive margin cannot be explained by uplift or isostasy of a single tectonic block or dome. The evolution of the PCM is likely to be more dynamic and complex, involving several periods of separated tectonic block movements with differential exhumation rates.

Chapter 3

Methodological Background

Thermochronology exploits the radiogenic decay, in combination with temperature-dependent processes within the crystal-lattice of uranium-rich minerals, to infer the time passed since a specific temperature(-range) was reached. In general, every uranium-rich mineral can be used, like apatite, zircon or titanite, allowing for more variety in dated temperature(-ranges) and answering different geological questions (e.g. Malusà and Fitzgerald, 2019a). For this study, only apatites were analyzed to cover the temperature range that resolves for uplift and erosion event. In this study, two different thermochronological methods were employed: Apatite Fission Track (AFT) and (U-Th-Sm)/He on apatite (AHe) have been used for dating ages of temperatures of upper crustal levels. Results from these methods were additionally modelled to reconstruct a possible denudation history. Most samples are part of a vertical profile at Skåla. To further help interpretation, a lineament map with field data was constructed.

3.1 Apatite Fission Track Analysis

Already in the 19th century, Baumhauer (1894) described fission tracks as 'hair-' or 'snout-like channels' in crystals when exposed to acidic fluids. Silk and Barnes (1959) had the same interpretation with the help of an electronic microscope, as they establish a relation of fission track production to radiation exposure. The possibilities of the geological application were first discussed by (Price and Walker, 1963), followed soon by Naeser (1967) applying fission track analysis on apatites for the first time. However, early fission track studies were mainly concerned with issues like track-revelation, uranium concentration as well as defining time-temperature stability fields for different uranium-bearing minerals, tektites and glasses (Fleischer et al., 1965). Pioneering work in this field resulted in a greater understanding of fission track formation (Fleischer et al., 1975, summarized in) and the introduction of the Zeta-value by Hurford and Green (1983) made the comparison of fission track data

more feasible. Initially, mainly used for absolute dating of glasses (e.g. Gentner et al., 1967) and volcanic or metamorphic rocks (e.g. Naeser, 1967), the potential for dating other thermal events, like burial and exhumation, were already recognized by Wagner (1968). Gleadow et al. (1986) demonstrated how confined track lengths can be utilized for more detailed geological interpretation and reconstruction of low-temperature thermal histories. Over the decades, fission track analysis gained recognition not only as a dating method for glasses, but first and foremost for the evolution of orogenic mountain belts, provenance studies and the thermal history of basins (Gallagher et al., 1998) including its convenient application in hydrocarbon exploration (Gleadow et al., 1983).

3.1.1 Fission track formation

Fission track thermochronology infers ages of temperature(-ranges) based on the number of occurrences of so-called fission tracks and less on the accumulation of daughter isotopes. These fission tracks are formed during the spontaneous fission of ^{238}U and represent microscopic trails caused by radiation damage (e.g. Wagner and Van Den Haute, 1992). Unlike in radioactive decay, in spontaneous fission a heavy isotope splits into two roughly equally sized atoms. This process can happen spontaneously or intentionally. In the latter case, either by bombardment with particles or by irradiation with γ-rays (Wagner and Van Den Haute, 1992). Spontaneous fission occurs only in elements of the actinide group, with an atomic number ≥ 90 and an atomic mass ≥ 230. However, only ^{232}Th, ^{235}U and ^{238}U occur naturally in measurable concentrations, where the latter one contributes by far the most to the observable fission tracks. Other heavy isotopes, like ^{235}U and ^{232}Th have too long spontaneous fission half-lives or are naturally too scarce to contribute significantly to the numbers of tracks observable (Table 3.1, Wagner and Van Den Haute, 1992; Gallagher et al., 1998). Consequently, the analyzed mineral must implement ^{238}U in its crystal lattice to eventually show fission tracks.

A commonly preferred model for fission track formation is the “ion-explosion spike” model proposed by Fleischer et al. (1965) (Fig. 3.1). A heavy nuclide is being split into two positively charged nuclides with similar but unequal mass. During that event around 210 MeV of energy is released, of which on average 170 MeV is liberated as kinetic energy. This ejects both daughter particles in opposite directions, but of unequal distance because of their unequal mass and powerful enough to leave their electron clouds behind (Ketcham, 2018). As both particles are positively charged, they will capture electrons of adjacent elements, slowing them down until they eventually come to rest. This process causes ionization along the distance the particles travel, creating a trail of positive ions in the crystal lattice. Coulomb repulsion causes these ions to relocate, opening vacancies along the pathway of the fission

Tab. 3.1. Overview of ^{238}U abundances, total half-life and fission half-life of ^{232}Th and various U isotopes. Please note that even though ^{238}U has the shortest spontaneous fission half-life, it is still more likely for any heavy isotope to simply decay via α-decay, which would not result in the formation of a track. [a]Steiger and Jäger (1977); [b]Holden (1989); [c]Baard et al. (1989); [d]Geochemical age, from Wagner and Van Den Haute (1992)

	Relative abundance (compared to 238U)	Total half-life (years)	Spontaneous fission half-life (years)
^{232}Th	4[d]	$1.40 * 10^{10}$[a]	$1.0 * 10^{21}$[c]
^{234}U	$5{,}44 * 10^{-5}$	$2.46 * 10^{5}$[b]	$1.5 * 10^{16}$[b]
^{235}U	$7{,}25 * 10^{-3}$	$7.04 * 10^{8}$[a]	$1.0 * 10^{19}$[b]
^{238}U	1	$4.47 * 10^{9}$[a]	$8.2 * 10^{15}$[b]

product. This strains the adjacent lattice, forming a trench that widens by elastic relaxation. The last process widens the trail to a larger extent as the actual pathway, damaging the area (almost) permanently and allowing the observation of fission tracks in the first place (Fig. 3.1 Wagner and Van Den Haute, 1992; Gallagher and Brown, 1999). This model is consistent with the observation that fission tracks only appear in insulating solids, but not in conductors.

Although this model is relatively widely accepted, it does not explain every aspect of fission track formation and thus can only be seen as a first approach (Wagner and Van Den Haute, 1992; Gallagher et al., 1998). Other models include the thermal spike model, which argues that the process is thermally driven and initiated by the energy released during fission (Vineyard, 1976); the gap model, which tries to explain the intermittent character of fission tracks by discontinuities in the crystal lattice (especially in layered minerals) (Chadderton, 1988); or the compound spike model, that combines both thermal and ion spike explosion models (Chadderton, 2003). A successful fission track analysis can therefore be achieved on a large selection of minerals with a wide range of ages, with the limiting factor being the U-concentration. Low U-concentrations coupled with young ages can lead to no tracks, while vice versa old ages with high U-concentrations can lead to such an abundance of tracks that individual tracks become indistinguishable. Consequently, this allows surveying a wide range of (primarily siliceous) lithologies (e.g. Kohn et al., 2019).

3.1.2 Latent tracks and track revelation

The distance between the fission nuclei after travelling is on average 21.2 ± 0.9 µm long (Jonckheere, 2003). However, fission tracks in apatite are, when using standard protocols, in the order of 16 µm (Ketcham et al., 2015), meaning that the stopping distance of fission particles is about 25% longer than the observable/etchable fission track. Latent (i.e. unetched) fission tracks can only be observed with a transmission electron microscope (TEM) because their

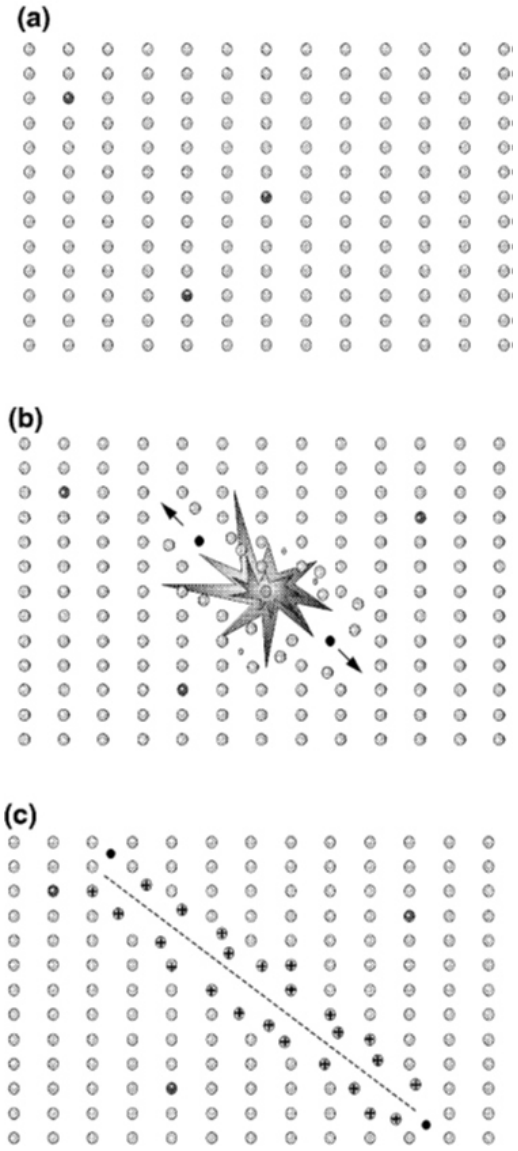

Fig. 3.1: Cartoon representation of the ion-spike model and fission track formation. a) Trace amount of ^{238}U is implemented in host mineral. b) By spontaneous fission two roughly equal-sized daughter ions are repelled, in opposite direction, by the energy released during the event (210 MeV). The charged heavy isotopes interact with the surrounding crystal lattice ionizing atoms along their path of trajectory. c) The ionized atoms repel each other resulting in more lattice deformation. Eventually the heavy isotopes slow down and come to rest as they lose energy. These damages however cannot be observed unless chemically etched (Gallagher et al., 1998).

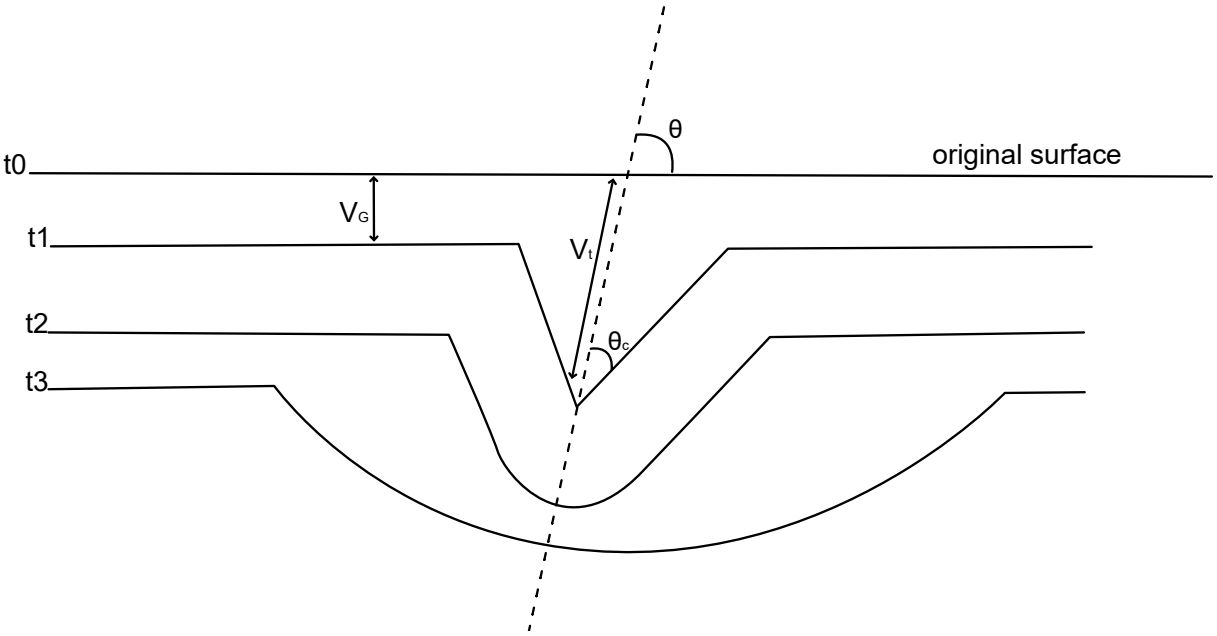

Fig. 3.2: Simplified evolution of an etch pit in time steps t0, t1, t2, t3. With the etchant progressively removing material from the grain (V_G) while increasing the depth of the etch figure (V_t), if etching is continued to long, the etch figure widens. Simplified after Ali and Durrani (1977), (Wagner and Van Den Haute, 1992)

initial width is just a few nm. So, to observe them optically, they need to be etched i.e. chemically widened (Wagner and Van Den Haute, 1992; Gallagher et al., 1998). Other methods of track revelation have been developed, as presented by Fleischer et al. (1975), but chemical etching has become the standard in thermochronological applications (Wagner and Van Den Haute, 1992), so only this particular technique will be covered here. The etchant hereby acts destructive to the whole crystal surface, removing layer by layer of the glass or crystal and ideally revealing more and more tracks (Wagner and Van Den Haute, 1992). The etching rate is generally much higher in tracks, as the atomic bonding is weakened due to the ionization damage, though not constant along the track as it rather diminishes towards the tip (Fleischer and Price, 1964; Fleischer et al., 1975; Tamer and Ketcham, 2020). This also causes the shape and size of a track to change significantly, from being conical in the beginning to rather rounded as etching time progresses (Ali and Durrani, 1977, Fig. 3.2). Testing showed that tracks with an axis inclined less than a certain value, are not being etched and will therefore not be revealed (Fleischer and Price, 1964; Fleischer et al., 1975). Due to the anisotropy of an apatite crystal, the etching rate varies also with orientation, being the fastest parallel to the crystallographic c-axis. This also implies that measurements need to consider the crystal orientation and are commonly carried out parallel to the c-axis (e.g. Green et al., 1986; Sobel and Seward, 2010; Ketcham et al., 2015). Furthermore, the overall composition influences etching rates, as the rates increase with Cl and OH content (Ravenhurst et al., 2003; Kohn et al., 2019).

The etching procedure has a direct influence on the densities and lengths of fission tracks that are actually observed. As these are ultimately used to infer ages, it is paramount to be in full control of the etching time, the concentration and the temperature of etchant during the preparation (Wagner and Van Den Haute, 1992).

3.1.3 Fission track (partial-)annealing

Fission track annealing describes the process at which fission tracks close and eventually disappear, affecting track length and density and therefore the measured age, as well. Extensive laboratory experiments by Fleischer et al. (1965) gave insights into the behaviour of tracks in different minerals under a wide range of physical conditions, like pressure, deformation, ionizing radiation and temperature. Of those, only the latter one has any significant effect on the fading of fission tracks. Other properties are either geologically unlikely or have no effect whatsoever. Deformation (e.g. due to shear stress) also does not result in shortening of fission tracks, but might lead to displacement and fragmentation of tracks (Fleischer et al., 1965). However, experiments on apatite by Wendt et al. (2002) did show a significant sensitivity of pressure, increasing the stability of fission tracks with higher hydrostatic pressures. Wendt et al. (2002) argue that ages therefore tend to be highly underestimated. The closure temperature (i.e. effective retention temperature) of apatites, is the temperature threshold at which the system is considered to be closed and fission tracks start to effectively accumulate. For apatite this temperature is 100 ± 20 °C (Wagner and Van Den Haute, 1992). In truth, however, this must rather be described as a temperature-range of ~70 °C, in which the tracks are partially annealed (Fig. 3.3). This *partial annealing zone* (PAZ) becomes apparent when looking at borehole studies. Borehole studies show a decrease in ages with increasing depth, but not in a linear fashion (Fig. 3.3, e.g. Gleadow and Duddy, 1981). A break in slope can be seen between temperatures of ~120 °C and ~60 °C (e.g. Wagner and Van Den Haute, 1992; Fitzgerald and Malusà, 2018). This temperature range is defined as the PAZ, in which fission tracks already start the annealing process, thus reducing the density of spontaneous tracks and therefore the age. Samples that experience temperatures above ~120°C anneal completely and thus show an age of 0 Ma. For temperatures below ~60 °C the fission tracks accumulate according to the rate of fission and do not anneal, increasing the age upwards. As chemical solubility affects the annealing rate, the effect of partial annealing varies with the mean length of etch pits (Dpars, Fig. 3.3, see below).

As fission tracks are produced continuously, the dispersion of ages is not only dependent on chemical composition, but also on the time remained within the PAZ. Generally, the age spread is larger the more time the sample spent within the PAZ. Furthermore, measuring track lengths and their distribution can provide a kinetic parameter for the thermal history

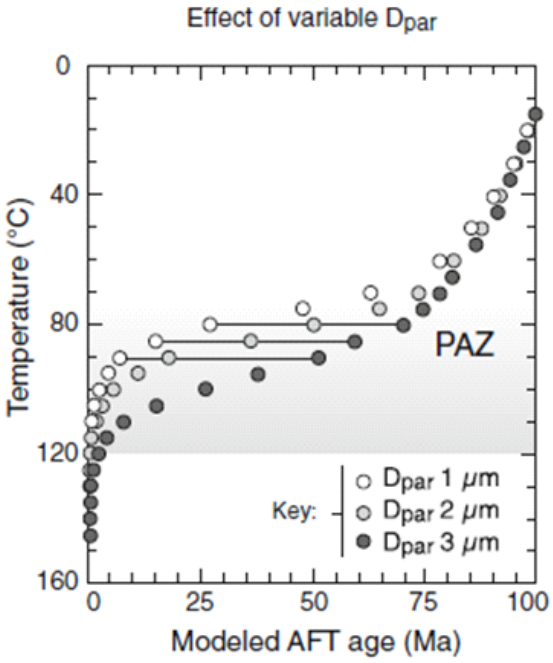

Fig. 3.3: Effect on FT ages in the PAZ, with Dpar as proxy for solubility and additional parameter. Samples with lower solubility (i.e. faster annealing) experience more younging when passing the PAZ, with the greatest age dispersion between 80 °C and 90 °C (Fitzgerald and Malusà, 2018)

in the PAZ (Gleadow et al., 1986, Sec. 3.2.2). Spontaneous fission tracks are generally shorter than induced ones (Bigazzi, 1967; Metha and Rama, 1969; Green et al., 1986), as some studies suggest due to slow annealing over a long period, even when exposed to ambient temperatures (Crowley et al., 1991; Spiegel et al., 2007; Tamer and Ketcham, 2020). The annealing process first leads to shrinking from both ends until, with further progression, the track starts to break into segments until those eventually anneal as well (Metha and Rama, 1969; Green et al., 1986; Paul, 1993). Several studies have shown that the annealing rate of fission tracks is dependent on their orientation, causing a slower reduction in length when parallel to the c-axis. This annealing anisotropy is becoming even more pronounced as annealing proceeds (e.g. Donelick et al., 1999; Green et al., 1986; Green and Durrani, 1977; Crowley et al., 1991; Ketcham, 2003). It has become therefore standard to measure the angle of the confined track to the c-axis and correct this discrepancy (e.g. Ketcham et al., 2015). Furthermore, the tracks' diameter has been reported as factor for annealing rate (Li et al., 2012). Besides these, another major factor that influences annealing is the minerals chemical compositions, in particular the Cl/F ratio for apatites, as demonstrated by Green et al. (1986). In apatite *(Ca5(PO5)3[F, Cl, OH])* the composition of the anions (F, Cl, OH) can vary and experiments have shown that Cl-rich apatites are more resistant against annealing(Green et al., 1986). The initial track length is empirically inferred by the arithmetic mean of the maximum length of etch pits parallel to the crystallographic c-axis (Dpar) (Donelick, 1993,

1995; Carlson et al., 1999; Kohn et al., 2019). It seems to be intuitive to believe that the Dpar therefore correlates positively with Cl wt% and negatively with F wt% of the measured crystal (Donelick, 1995; Burtner et al., 1994). However, Dpar should be viewed as being independent of any chemical composition and rather as a standalone parameter (Donelick et al., 2005). Apatite can also interchange with REE, Mn, Sr, Fe, Si (Green et al., 1986; Kohn et al., 2019) and as the effects of various chemical composition on annealing have not been completely envisioned, the parameter Dpar is only poorly correlatable with the actual chemical composition and therefore cannot be used as a proxy (Carlson et al., 1999).

3.1.4 Track classification and length data

Track lengths can contain thermal information (Gleadow et al., 1986), but only if both ends are visible. Confined tracks are completely preserved in the crystal and revealed as the etchant travels along pathways (e.g. surface tracks or cleavage) into an intersecting confined track (e.g. Ketcham et al., 2015). Lal et al. (1969) and Bhandari et al. (1971) define two different kinds of confined tracks, depending on the pathway. Confined tracks that are etched through other tracks (usually surface tracks) are commonly called TINT's (track-in-track), while confined tracks connected by cleavages or cracks are termed TINCLE's (track-in-cleavage – Fig. 3.4). TINDEF (track-in-defects), being confined tracks that use defects or inclusions as conduit, have been recognized by Donelick et al. (2005). Studies have shown that TINCLE's and TINDEF's may anneal differently or not at all (Barbarand et al., 2003; Jonckheere and Wagner, 2000). Donelick et al. (2005) suggest, in order to avoid unreliable data, that TINCLE's and TINDEF's should not be measured at all. As most etched tracks are intersected by the polished surface, it is unreliable to infer length data from these semi-tracks, but significantly less bias is expected from horizontal, confined TINT's (Laslett et al., 1982, Fig. 3.4). Track length measurements should only be applied on horizontal or close-to-horizontal (to the polished surface) confined tracks as only those, though much scarcer, allow to estimate bias (Gleadow et al., 1986; Laslett et al., 1982; Ketcham et al., 2015). Recent advances in observational technology allow for 3D imaging of mounts to correct the track length after dip angle, to allow the measurement of steeply inclining tracks while minimizing bias (Gleadow et al., 2019). As mentioned above, the annealing properties are also dependent on the orientation of tracks to the c-axis (e.g. Donelick et al., 1999; Ketcham, 2003). This would restrict track length measurements to confined tracks that are parallel to the c-axis. However, modelling efforts allow to correct for divergence from the c-axis for individual tracks and normalize the results (Ketcham et al., 2007).

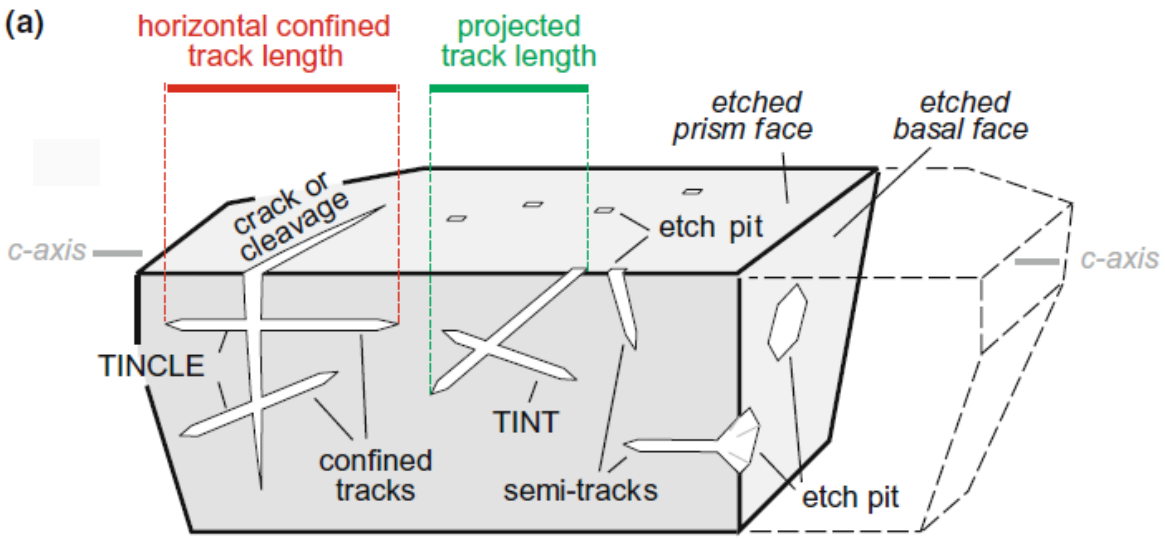

Fig. 3.4: schematic illustration comparing different etch figures. Confined tracks can be etched as long as the etchant can reach the track in some way, however only horizontal TINT (track-in-track) shall be measured for track length analyses as non-horizontal TINT, TINCLE (track-in-cleavage) or semi-tracks may not represent the complete length and lead to bias. Modified after Malusà and Fitzgerald (2019a)

3.1.5 Fission track age equation

It is crucial to keep in mind, that thermochronological ages do not give absolute ages, but rather give the time passed since the mineral last experienced a specific annealing/closure temperature(-range). In glasses and tektites, this temperature is close to their formation age. However, for this study basement rocks were used. So, the age reflects the time the closure temperature was reached and tracks started to accumulate. The age t (in years) for the fission track systems can be generally described by the following equation (Naeser, 1967; Hurford and Green, 1983, after):

$$t = \frac{1}{\lambda_D} ln\left(1 + \frac{\lambda_D \Phi_\sigma Ig \rho_s}{\lambda_f \rho_i}\right) \tag{3.1}$$

λ_D is the total decay rate of ^{238}U, including both spontaneous fission and regular decay of ^{238}U. The values of $1.55125 * 10^{-10}$ for λ_D (Jaffey et al., 1971) and $7.2527 * 10^{-3}$ for the isotopic abundance ratio of ^{235}U/^{238}U I (Cowan and Adler, 1976) have been generally accepted and recommended by the IUGS Subcommission on Geochronology (Steiger and Jäger, 1977; Hurford and Green, 1983; Wagner and Van Den Haute, 1992). σ is the thermal neutron fission cross-section for ^{235}U and g is a geometry factor, describing the ratio of observed area for spontaneous and induced tracks. ρ_s and ρ_i is the track density for spontaneous and induced tracks, respectively. Additionally, λ_f is the spontaneous fission decay constant of ^{238}U and Φ is the thermal neutron fluence, that both pose a special problem in the calculation of

ages. The thermal neutron flux Φ is usually solved by inserting additional monitor glasses with known concentrations of uranium into the irradiation (Hurford and Green, 1983, see Sec. EDM). Φ can be described in following a linear relationship to the neutron-induced track density on a monitor glass ρ_d:

$$\Phi = B\rho_d \tag{3.2}$$

where B is a constant derived from used dosimeter glass and its preparation (Hurford and Green, 1983; Wagner and Van Den Haute, 1992). This allows for determination of the neutron fluence for each position in the irradiation. The spontaneous fission decay constant λ_f led to dispute on which value would be the exact one, as several studies inferred different values (Wagner and Van Den Haute, 1992, presented in). This problem resulted in general doubt of the reliability of the method (Wagner and Van Den Haute, 1992). However, Hurford and Green (1983) suggested the use of the so-called Zeta calibration to circumvent this problem (Sec. 3.1.8).

3.1.6 Age standards

The most commonly used age standards for Apatite Fission Track Analysis, and also used in this study, are Durango and Fish Canyon Tuff apatites (FCT). Wagner and Van Den Haute (1992) formulates different requirements for age standards, including; homogenous age that represents formation (i.e. stratigraphic age) rather than cooling, accessibility and well-studied with independent age determinations. The FCT apatite standard comes from the Fish Canyon Tuff (Colorado, USA) a crystal-rich ash flow with up to 1000 m in thickness (Hurford, 2019). FCT apatites have been dated by ^{40}Ar / ^{39}Ar and K-Ar on biotite, sanidine, hornblende and plagioclase by Steven et al. (1967)and Hurford and Hammerschmidt (1985) to a commonly accepted age of 27.8 ± 0.5 Ma (e.g. Hurford, 2019). Durango apatites are euhedral, up to 3 cm long minerals from the Cerro de Mercado iron mine close to Durango City, Mexico (Paulick and Newesely, 1968; Young et al., 1969). The crystals are usually fragmentated before mounting, due to their size. Durangos have been dated to 31.4 ± 0.6 Ma by K-Ar dating and ^{40}Ar / ^{39}Ar ages on sanidine-anorthosite of the Santuario Fm. and Aguila Fm. as well as (U-Th)/He ages on the Durango directly with affirmative results (mean ages from Mcdowell and Keizer, 1977; Mcdowell et al., 2005; Hurford, 2019).

3.1.7 External detector method (EDM)

To infer the amount of ^{238}U in a grain, the most common method is the *External Detector Method* (EDM). Since the ratio between ^{235}U and ^{238}U is always the same (^{235}U / ^{238}U =

$7.201 * 10^{-3}$) and usually verified by the dosimeter provider (e.g. Roebben et al., 2006), the amount of ^{238}U and ^{235}U in a grain can be inferred by the density of induced tracks (ρ_i). External detectors (e.g. IRMM-540R) are conventionally a low-uranium sheet of muscovite, manufactured to be clear and free of any defects. Muscovite is used, as it shows similar etching properties (like anisotropy) as the minerals it is compared with (Kohn et al., 2019). To apply the EDM, the grain mount is first etched to reveal spontaneous tracks. The mica is then attached to the polished surface of the mount during irradiation. As irradiation with thermal neutrons primarily induces fission of ^{235}U, while other uranium and thorium isotopes are negligible. The resulting induced fission tracks on the external detector are exclusively from the ^{235}U in the grain (Donelick et al., 2005, Fig. 3.5) and imprinted as tracks on the detector. After irradiation, only the detector is etched to reveal the induced tracks. The mount is not etched again, so induced tracks remain undetected on the grain mount (Kohn et al., 2019). The detector therefore shows a mirrored print of the grain mount and henceforth for each grain, making this method also viable for highly heterogeneous U-concentrations. The advantage of inferring uranium in this way, instead of via laser ablation inductively coupled mass spectrometer (LA-ICP-MS), is that it is non-destructive, allowing to repeat the measurements ensuring scientific reproducibility. However, recent advancements in the development of automatic counting technology, incl. automatic c-axis determination (Gleadow et al., 2019), would make the EDM redundant, as using the LA-ICP-MS is much faster, does not require any irradiation (incl. the handling with radioactive material) and reduces manual FT counting (Gleadow et al., 2019). Even though laser ablation destroys the analyzed grain, 3D imaging/image stacking would archive all the necessary information, maintaining reproducibility and will therefore most likely become the state of the art.

3.1.8 Zeta (ζ) calibration

In the early phases of using the EDM, a main issue was the lack of comparability in published ages. A wide range of λ_f values for the spontaneous fission decay were available to choose from, as well as a systematic error in absolute neutron flux values Φ, due to differences in track observation (i.e. counting) (Hurford and Green, 1983). To circumvent these issues, Hurford and Green (1983) developed the Zeta value approach, which has become the standard approach for fission track age determination (Hurford, 1990; Lisker et al., 2009). The resulting Zeta-value can be viewed as a personal "correction"-factor, with which different workers should be able to infer the same results despite variations in counting accuracy. This allows for reliable comparability, also with other laboratories and researchers. By repeated counting of age standard with jointly irradiated dosimeters, a ζ-value can be inferred

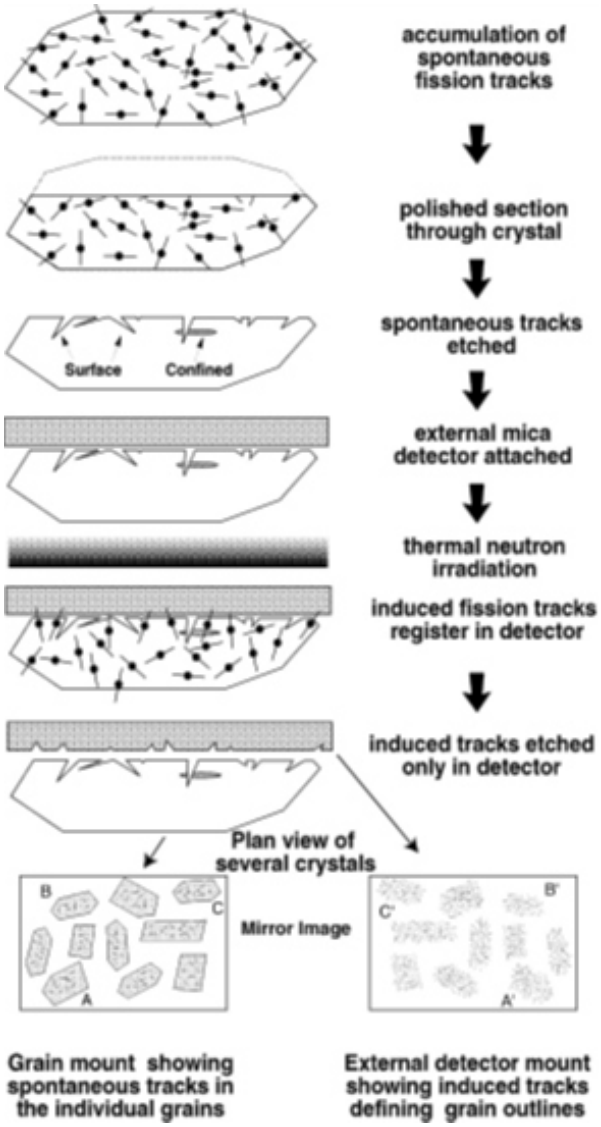

Fig. 3.5: Procedure for the external detector method to determine fission track age and ^{238}U concentration: Grain with accumulated spontaneous tracks is polished and subsequently etched to reveal tracks, including confined tracks. Mica is attached adjacent to the polished surface and irradiated together to register induced tracks. The detector is then etched as well, to reveal the induced tracks, that derive from ^{235}U. Mount and detector are placed next to each other, where the detector represents the mirrored image of the mount. Gallagher et al. (1998) after Hurford and Carter (1991)

and written as follows:

$$\zeta = \frac{\left(e^{\lambda_D t_{Std}} - 1\right)}{\lambda_D \left(\frac{\rho_s}{\rho_i}\right)_{Std} g \rho_d} = QI\sigma \frac{B}{\lambda_f} \tag{3.3}$$

As the age of the counted standard t_{Std} is usually known, only the track densities of spontaneous (ρ_s) and induced (ρ_i) tracks have to be measured, as well as the track density on the dosimeter (ρ_d) to determine the calibration factor ζ. Factor Q can be seen as a procedure factor and is considered to be 1, if the track revelation of spontaneous and induced tracks is identical. The parameters for the total decay rate of ^{238}U λ_D, the isotopic abundance ratio I, the geometry factor g, the neutron fission cross-section σ and the dosimeter specific constant B are as already established in Equation 3.1 and 3.2. This approach removes problems with varying λ_f, while considering possible systematic counting errors, changing the original age equation 3.1 to following equation:

$$t = \frac{1}{\lambda_D} ln\left[\lambda_D \frac{\rho_s}{\rho_i} \rho_d g \zeta + 1\right] \tag{3.4}$$

The inferred value for ζ, however, must be considered as personal and the calibration must be carried out personally by every worker, before measuring fission track ages. Furthermore, the ζ-value is only valid for the mineral used during the calibration (Wagner and Van Den Haute, 1992). For the Zeta calibration, Hurford (1990) recommends at least five different analyses per mineral phase, ideally from different irradiations. Each should have more than one age standard (e.g. Durango and Fish Canyon Tuff). A ζ-value can be inferred for each standard, that has been analyzed using equation 3.3. The final value of ζ is then given by the weighted mean of each Zeta determined, using the inverse of the error as weight.

3.1.9 Chi-square (χ^2) test

When estimating ages for each grain individually, it is almost certain that the grains will show different ages. At least two well-recognized geological processes can explain this dispersion; either the grains originate from different sources, which can be the case for sedimentary rocks, or the chemical compositions of the grains vary within a sample (Galbraith and Laslett, 1993). Also, in scenarios with a sequence of samples with increasing temperature (Sec. 3.2.3), a common pattern is to see the age dispersion to increase and then decrease as the central age decreases. Galbraith and Laslett (1993) explain this pattern with differences in annealing for varying chemical composition, where increasing temperature maximizes annealing spread until eventually some have annealed completely and others remaining. To assess if the age distribution shows one distinct age or several age populations the χ^2 test is com-

monly used (Galbraith, 2005), given by:

$$\chi^2 = \frac{1}{N_s N_i} \sum_{j=1}^{n} \frac{\left(N_{sj} N_i - N_{ij} N_s\right)^2}{N_{sj} + N_{ij}} \tag{3.5}$$

where j = 1,2,...,n with n being the number of grains. N_{sj} and N_{ij} denote the amount of spontaneous and induced tracks in grain j, respectively. N_s and N_i are the total amount of spontaneous and induced tracks. Equation 3.5 assesses if the true ratio of ρ_s / ρ_i is the same for each Poisson distribution i.e. every grain/print pair of a sample. For a sample with a homogeneous true age, the result should be a value within the χ^2 distribution with (n-1) degrees of freedom. A p-value for each grain then reflects the probability that the value from the χ^2 (n-1) distribution does exceed the calculated value for χ^2. For a p-value of 5% and smaller the chi-square test is regarded as failed and multiple age populations need to be considered (Galbraith, 2005). A visual way of estimating the spread of ages are radial plots of single grain ages (Galbraith, 1990). The y-axis, as the standard error, is plotted vis á vis a bent z-axis with the average age centered at y=0. The x-axis shows the precision. Ages in the plot can be read off by extrapolating the radius from (0,0) through the plotted point onto the z-axis. Each plotted age also displays precision (by its placement along the x-axis) and standard error (by its placement along the y-axis). The precision tends to be larger with higher N_i and N_s values, but also results in larger y scatter.

3.1.10 Length calibrations

Length measurement calibrations are usually not standard for the procedure; however, it was applied for this study. Similar to the ζ-calibration, the error on length measurements was evaluated by analyzing Durango mounts to obtain a value quantifying the measuring precision. These Durangos were annealed before irradiation and etched afterwards, to reveal induced tracks on the grains. The arithmetic mean of the track length measurements was then compared to results presented in Ketcham et al. (2015). The ratio $L_{published}$ / $L_{this\ study}$ provides the correction factor that will be used during modelling. The same procedure was also applied for the Dpar measurements.

3.1.11 Error calculations

To gain a proper geological age from the individual estimated grain ages, it is not possible to simply take the arithmetic mean, as it cannot cope well with outliers and asymmetric distributions (e.g. Vermeesch, 2019). For scenarios with no dispersion, the pooled age can

represent the true geological age. However, since that is only the case for discrete ages, e.g. in rapidly cooling rocks, generally the central age is calculated. Besides the Poisson uncertainty, the central age takes also the (over-)dispersion and their respective error into account. This limits the skew of the pooled age to older ages when dispersion plays a role, and also shows similar ages when the dispersion equals zero, but with a larger error (Galbraith and Laslett, 1993). Generally, the analysis of at least 20 grains is recommended per sample, to gain a fairly robust result (e.g. Galbraith and Laslett, 1993; Gallagher et al., 1998; Donelick et al., 2005). The error of the ages $\frac{s_t}{t}$, estimated by the EDM, can then be calculated using following equation:

$$\frac{s_t}{t} = K\sqrt{\left(\frac{S_R}{R}\right)^2 + \left(\frac{S_\Phi}{\Phi}\right)^2} \tag{3.6}$$

where $\frac{S_R}{R}$ is the error of the ratio of spontaneous to induced tracks, $\frac{S_\Phi}{\Phi}$ is the error of the neutron flux and K ≈ 1 for ages <600 Ma. The calculation of $\frac{S_R}{R}$ depends on the procedure. If the detector chosen does not show any etched spontaneous tracks, $\frac{S_R}{R}$ can be calculated by this equation:

$$\frac{S_R}{R} = \sqrt{\left(\frac{S_{\rho_s}}{\rho_s}\right)^2 + \left(\frac{S_{\rho_i}}{\rho_i}\right)^2} \tag{3.7}$$

When using the ζ-calibration, $\frac{S_\Phi}{\Phi}$ refers to the error on the track density on the dosimeter. The error calculated by equation 3.6, include a 1σ error interval. The error of the ζ-calibration itself is relatively low and only accounts for about 1-1.5% (1σ) (Wagner and Van Den Haute, 1992).

3.2 Geological Interpretation

Wagner (1968) made the first attempt at interpreting varying fission track ages not as crystallization age, but rather as indication for an uplift history. Soon after, Wagner (1975) reconstructed the thermal history of the Odenwald, Germany under consideration of a partial annealing zone (PAZ, see below) and track length distributions. As fission track ages resemble the start of track accumulation, it cannot be considered as a formation (i.e. absolute) age, even defining it as the age of a thermal event is only an approximation. Generally, the calculated age is also just the apparent age, as it is usually younger than the entry into the PAZ (e.g. Wagner and Van Den Haute, 1992). It can get even more complicated, as more complex thermal histories influence the calculated age. For example, a sample can experience uplift (i.e. cooling) and subsequent burial (i.e. reheating). The fission track age may not represent only a single thermal event, but several. Furthermore, annealed i.e. shorter tracks are less likely to intersect the polished surface, which results in a lower spontaneous track density and hence

in younger ages (Laslett et al., 1984). To put it simple, as all above is influenced by partial annealing, the samples calculated age is dependent on the time it remains in the PAZ (e.g. Wagner and Van Den Haute, 1992). This feature makes fission track a poor dating method for absolute ages, but a remarkably powerful tool for reconstructing thermal histories, as will be discussed in the following sections.

3.2.1 Exhumation/Denudation

As fission track is a temperature-driven method, the thermal evolution in the upper crust is taken into account to infer geological information. A change in temperature will therefore usually be considered a change in crustal elevation, if it is not immediate cooling after crystallization. If the time-temperature path and the prevalent geothermal gradient is known, the exhumation or denudation rate can be calculated. While uplift refers to the vertical change in elevation with regard to the geoid, exhumation and denudation describe the unroofing of a point or region, respectively, on the Earth's surface (e.g. Summerfield and Brown, 1998; England and Molnar, 1990). This is typically the result of erosion or removal of overburden by tectonic processes. Uplift is therefore somewhat misleading, as uplift alone

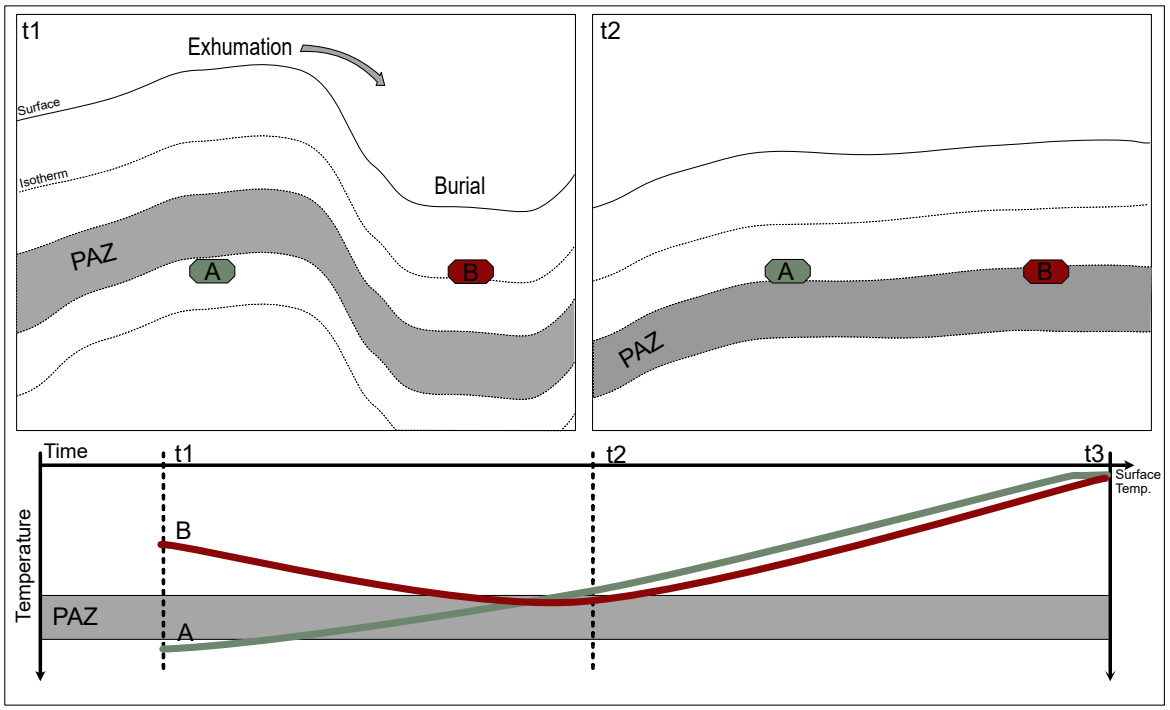

Fig. 3.6: Top: Simple example to describe the effect of exhumation/burial on the time-temperature path (bottom). Sample A: cooling due to unroofing; Sample B: reheating as it gets buried. At timestep t3 both samples resurface. The apparent age of sample A will be between t1 and t3 while it passes the PAZ, the apparent age of sample B will be older than t1. PAZ = partial annealing zone, dotted line= isotherms.

does not mean a change in ambient temperature. Only in combination with erosion does a sample experiences cooling. Typical denudation rates for continental margin are around 100 m/Ma and can be more than a magnitude higher in active orogenic belts (Gleadow et al., 2000). Of course, a sample can also experience burial, which can with sufficient reheating cause annealing. Strictly speaking, in those scenarios above it is not the depth per se, but the isotherms affecting the samples thermal history (Fig. 3.6). When plotting against elevation, the assumption is that isotherms are horizontal. However, isotherms tend to mimic topography (Fig. 3.6). These are not equal along a high relief topography, with relevant isotherms being deeper beneath ridges and shallower under valleys (Malusà and Fitzgerald, 2019b).

3.2.2 Track length distribution

To obtain kinetic parameters for the exhumation rate of a sample in the upper crust, the effects of partial annealing through the PAZ can be used. As previously discussed, within the PAZ tracks are continuously reduced in length due to elevated temperature, whilst new tracks are continuously formed. This leads to track length distributions unique to the path a rock-sample follows in the upper crust (Gleadow et al., 1986), that can aid in forward modelling. Gleadow et al. (1986) distinguishes between 3 arche types of track length distributions, summarized in Figure 3.7. A) Typically, a volcanic system that rapidly cools through the PAZ and experiences only little partial annealing. It remains most of the time in at temperatures lower than the PAZ, with stable track conditions, so the measured age approximately resembles the formation age. The distribution remains narrow, because the track accumulation starts shortly after mineralization with only a little time to partially anneal. B) A slow and steady cooling system is typically for uplifted basement systems. Due to a slower cooling, the sample remains longer in the PAZ. That results in a wider track length distribution. When lower temperatures are reached, the track accumulation continues without annealing and the mean track length increases. The result is a broader but normal distributed spread. C) In cases of tectonic subsidence, samples can be reheated back into the PAZ. The result is a mixed or even bimodal distribution, where shorter track lengths are remainders from the first cooling event, that have been annealed before. Longer tracks were formed more recently during the last cooling event. If the reheating event is too short or does not reach sufficient temperature, no distinct bimodal peaks are formed, rather shaping a broad distribution similar to an undisturbed basement. However, more complex thermal histories, like for mixed distributions, generally show higher standard deviations. On the other hand, the greater the difference between the cooling and reheating is, the more pronounced a bimodal distribution will be. D) In scenarios where the reheating reaches temperatures higher than the PAZ and fission tracks anneal completely, the distribution will resemble case A) or B), depending

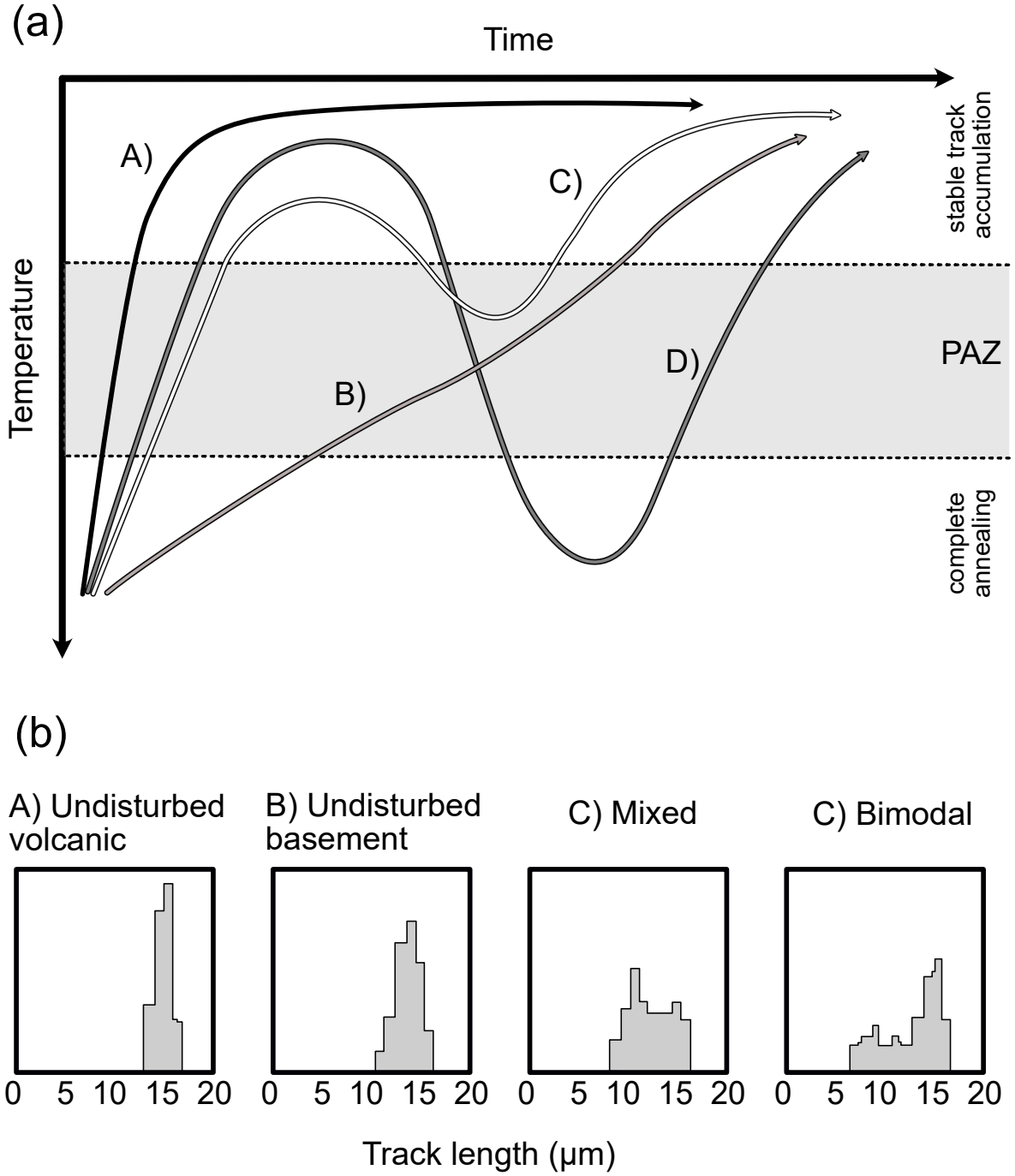

Fig. 3.7: a) Schematic time-temperature path for track-length distribution as described in the text above in more detail: A) fast cooling, undisturbed volcanic system; B) slow cooling, undisturbed basement system; C) mixed system with reheating in the partial annealing zone (PAZ); D) path with extensive reheating, track length distribution will resemble A) or B) and measured age will show the reset age i.e. age of last cooling event. b) corresponding track length distributions to individual scenarios as described in the text. A) fast cooling, narrow distribution; B) slow cooling, broad distribution; C) mixed and bimodal distribution, depending on time and reached temperature of reheating event the distribution can be clearly bimodal or mixed with a broad distribution but larger standard deviation. (redrawn after Hurford, 2019, from Wagner (1972); Gleadow et al. (1986)).

on the subsequent cooling rate. Measured ages would, in that case, also only relate to the second cooling event.

3.2.3 Vertical profiles

Borehole studies have shown that with increasing depth the fission track ages correspondingly decrease (e.g. Gleadow and Duddy, 1981). The same principle applies for samples that have been taken in different elevations, but with short horizontal distance, for example along a steep mountain-side. Here ages would increase with elevation (Wagner and Reimer, 1972). These profiles develop during steady denudation when rock samples cross the isotherm associated with the beginning of track accumulation. Samples that eventually end up in the highest elevation, pass this isotherm before samples of lower elevation, hence accumulating more tracks. The slope of the fission track age against the elevation would then show the rate of denudation (e.g. Reiners and Brandon, 2006). However, this approach is complicated by the possible exhumation of a fossil PAZ (PRZ for AHe), given that the amount of denudation is sufficient. When a period of relative tectonic and thermal stability precedes a rapid cooling, the typical shape of an age-depth graph of a PAZ is preserved in the ages of a vertical profile (Fitzgerald and Gleadow, 1990; Gleadow and Fitzgerald, 1987). The base of the exhumed PAZ can be seen in the profile as break in slope and its age is generally referred to as onset of rapid exhumation (Fitzgerald and Gleadow, 1990; Gleadow and Fitzgerald, 1987). The slope of ages below interpreted onset represents the apparent exhumation rate during the rapid cooling (considering no lateral variations). The break in slope must also rather be seen as a curve, as those samples need to pass the PAZ as well, making the break more continuous than sudden. The samples can experience a significant amount of annealing if the cooling is not rapid enough, skewing the onset towards older ages (e.g. Fitzgerald and Malusà, 2018). The shape of the age-elevation plot and slope of PAZ is dependent on the heat flow, rate of exhumation and the amount of time the system has been stable prior to exhumation. If the period of tectonic and thermal stability is too short (e.g. < 10 Myr) the break in slope becomes indistinguishable (e.g. Fitzgerald and Stump, 1997). Track length distributions in vertical profiles can also reveal exhumed PAZ's as above the break of slope, the track lengths often show a bimodal distribution; one shorter component formed prior to cooling and longer tracks that formed during or after exhumation. Distributions below the break of slope are all expected to be long, as they represent rapid cooling and spend only a short time in the PAZ (Fitzgerald et al., 1995; Fitzgerald and Malusà, 2018, Fig. 3.8). The slopes of an exhumed PAZ can be carefully interpreted, as summarized in Fig. 3.8:

As mentioned in Fig. 3.8, the slope of the PAZ above the break in slope, allows estimating the paleo-geothermal gradient prior to rapid cooling. Considering the existence of an exhumed

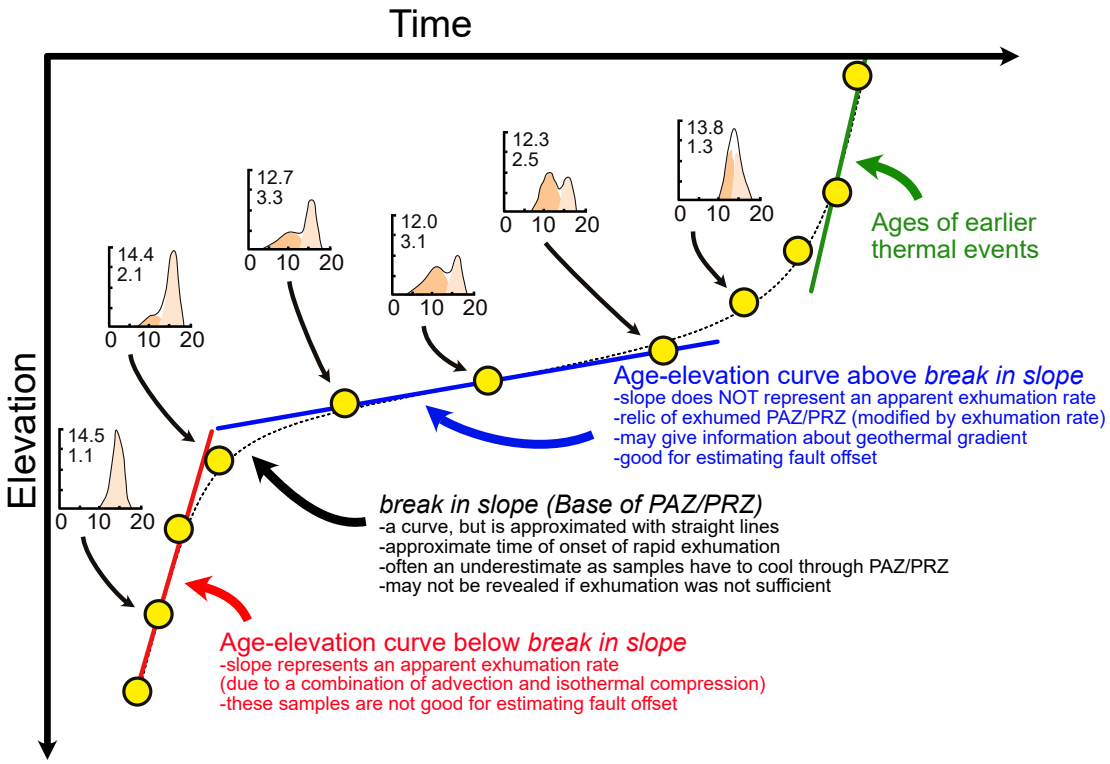

Fig. 3.8: Summary of exhumed PAZ/PRZ features and how to interpret them. Yellow points: Samples from vertical profile. Dashed line: regression line of ages. Example of track length distributions given for some samples: distribution in fossil PAZ/PRZ show two populations, in dark colour the shorter and older component, in light colour long and more recent tracks. Example of mean track lengths in µm as well as the standard deviation is also given (redrawn after Fitzgerald and Malusà, 2018).

PAZ in the profile, a stable geothermal gradient prevailed prior to cooling and the heat flow was not obstructed by intrusions or other events (Gleadow and Duddy, 1981; Bray et al., 1992; Fitzgerald et al., 1995). If the stratigraphy of the profile is well constrained, the gradient can be calculated by simply dividing the overburden by the difference of the temperature at the base of the PAZ to the paleo-mean surface temperature (Fitzgerald and Gleadow, 1990). Various thermochronological methods, with different closure temperatures (namely AFT and AHe), can also be employed to constrain the paleo-geothermal gradient. Alternatively, considering that the gradient has been stable, a continental geothermal gradient of 20 - 30 °C/km can be assumed (e.g. Fitzgerald et al., 1995). The paleo-geothermal gradient is necessary to estimate the amount of removed overburden, but a change in gradient can also give constraints on tectonic processes (Lisker et al., 2009, e.g. rifting,). Bray et al. (1992) suggest inferring the paleo-geothermal gradient from the regression of the modelled maximum paleotemperatures against sample elevation. The advantage of additional AHe data used in a vertical profile is not only verification of AFT data. As AHe has a lower closure temperature, the PRZ is located at higher elevations of a vertical profile, which makes it more likely to expose a closure temperature(-range), whilst further constraining the Time-temperature path (e.g. Fitzgerald and Malusà, 2018).

Chapter 4

Methods

Specific preparations need to be performed to make the observation of fission tracks in apatite possible and to infer an age as well as being able to measure track lengths. The samples were prepared by Åse Hestnes and subsequently analyzed by the me.

4.1 Sample Preparation

Samples collected during fieldwork were between 1.5 to 3 kg of pebble-sized material. Samples were crushed in a discmill (model) to sand, silt and clay size. On a Holman Wilfley shaking table (model) the bulk was separated by size. The <315 µm fraction was used for further processing. The material was then run through Frantz magnetic separator to remove magnetic minerals (1st 0.3 A; 2nd 0.6 A; some samples: 3rd 1 A). The non-magnetic fraction was then separated further by density using LST (density = 2.8 g/cm^3, lithium heteropolytungastate) and subsequently with DIM (d = 3.1 g/cm^3, diiodmethane). LST was used first to provide a clean zircon separate later in the prosess and to reduce the volume of DIM necessary, since DIM is highly toxic. These processes seperate non-magnetic minerals in the sample first at a density of 2.8 g/cm^3 (LST), then by 3.1 g/cm^3 (DIM). After the DIM separation we are left with an enriched apataite separate. The samples were then embedded in epoxy and etched for exactly 20 sec at 20 °C with 5.0 M Nitric acid to reveal spontaneous tracks. Finally, the mounts were packed with an external detector. Grain-Mica couples were sent to the research reactor FRM II in Garching, Munich, Germany for irradiation, using a neutron flux of Φ_{Th}=$1.15 * 10^1 31/cm^2$. The grains were irradiated so the containing uranium is excited and induces a track on the mica. These tracks are used during counting to infer the amount of ^{238}U in a grain and serve as an external detector (s.a.).

After cooling down to 0.92 mSv/h, the detector was etched with 40% HF acid for exactly 20

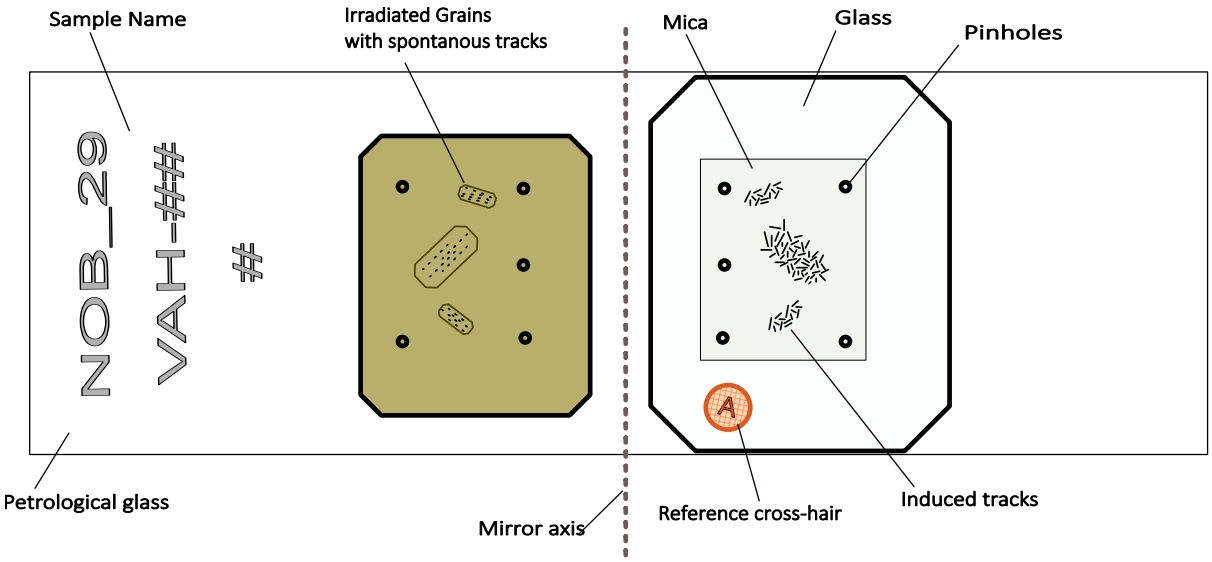

Fig. 4.1: Example of FT-sample, sample name incl. (from top to bottom): Irradiation Nr., sample Nr. (##) and position in column (#), note that the grain mount and mica are mirrored horizontally incl. pinholes as well as induced tracks in respect to grains, grains not for scale

min at room temperature to make the induced tracks visible under the microscope. The mica represents a mirrored print of the grains, only showing the induced tracks. Therefore it is important to be able to find every grain on the respective print accurately on the mica. Pinholes are pinched in the four corners through the mica and into the epoxy, as well as one additional pinhole on the inner side (Fig. 4.1), serving as reference points during analysis. Grain mounts and micas (external detector) are then glued next to each other, on a standard petrological glass, creating a horizontal mirror-axis. The detector was glued on an additional glass to reduce the height difference between mount and detector. A cross hair (A) was added as an additional reference point, on which the microscope can be precisely aligned.

4.2 Counting procedures

The pre-analytical procedures such as training and zeta calibrations took place between February and October of 2020. Due to the measures that were introduced to counteract the ongoing Covid-19 pandemic, these procedures were delayed. The measurements and counting of the actual samples took place between October 2020 and February 2021. Measurements were carried out in the thermochronological laboratory at the University of Bergen. For the analysis, an Olympus BX51 microscope was used with a magnification turret and a U-DA drawing attachment.

4.2.1 Dosimeter and its counting procedure

Before actual grains were counted, the dosimeter glasses were analysed. This is necessary to estimate the decrease in neutron flux and consequently the decrease in track density with distance to a neutron source. In total four IRMM-540R (15 ppm U) dosimeters were installed, with equal spacing within the sample container and the first one at the first position. Tracks were counted with a magnification of 1250x. 25 grids were counted for each dosimeter and repeated three times. The average tracks per grid were plotted over the position of its dosimeter. The linear regression of these provide the density of induced track on the dosimeter ρ_d for each position within the container. The values for ρ_d are being used in equation 3.2, at each position.

4.2.2 Zeta value calibration

Following a recommendation in Hurford (1990), five irradiations have been used with two standards each (Durango and Fish Canyon Tuff) for calibration of the personal Zeta value. Additionally, the standards of the irradiation, yielding samples of this study, were implemented into the Zeta-calibration (s.a.). The Zeta value of each standard and their respective standard deviation has been calculated using the software TrackKey (vers. 4.2) (Dunkl, 2002). A weighted mean was calculated from these single values, using the inverse of their standard deviation as weight, utilizing the software Meanzeta.exe (prob. by Mark Brandon). The calculated personal Zeta value has been additionally confirmed by counting samples with already published ages and determining the same results. The inferred Zeta-value is 213.85 ± 4.19 and was used in all further age calculations.

4.2.3 Samples counting and Standard calibrations

Counting techniques remained the same for both Zeta-calibration and sample counting. To achieve good mount-print counting, the alignment of the microscope needs to be as perfect as possible. The thermochronological setup of the microscope allows automatic centring on the print, given that a proper coordinate system was established. This is done by focusing on matching points on mount and print, prior to the counting. Pinholes are used for approximate alignment and pronounced outlines of grains on the print, i.e. of zircons were used as fine reference points (Fig. 4.1).

Only grains parallel to the c-axis have been counted (Fig. 4.2). These were recognized by a uniform orientation of Dpars parallel to the c-axis. One grid contains 10x10 cells and a frame was chosen that accommodates as many cells as possible covering the grain's surface. The

same area was counted on the respective print. The smallest frame used was 5x5 cells. It was aimed to count at least 20 grains for each sample, but generally, every grain passing the requirements was counted. No grain was counted twice. During the procedure, the quality of each grain was assessed and features such as inclusions, fractures, dislocation and zonations were noted. If possible, such beauty mistakes were avoided in the chosen frame, as they impede errorless counting. If an apatite showed zonation, only the inner core was counted, because the inner core always yielded significantly more tracks.

4.2.4 Track length and Dpar measurements

These measurements were conducted with a magnification of 2000x. For each counted grain, 5 Dpars were added to gain a mean to estimated solubility. Fission track lengths were obtained by measuring horizontal, confined TINT's. These are easily recognizable under reflected light, where they appear clear and bright with their full length in focus (Fig. 4.2). It was aimed to measure at least 100 TINT's for a robust thermal model (e.g. Donelick et al., 2005). The grain must be parallel to c-axis orientation to measure any track, independent of the track's orientation because solubility is dependent on the orientation of the crystal. Therefore, it has become standard to measure the angle of the confined track to the c-axis and correct this discrepancy (e.g. Ketcham et al., 2015). As the print is not necessary for measuring track lengths, TINT's were also measured in the outer rims of the mount, in grains that could have not been counted. As not enough tracks were found in most mounts, additional mounts (non-irradiated, but etched) were made for additional confined tracks. For each

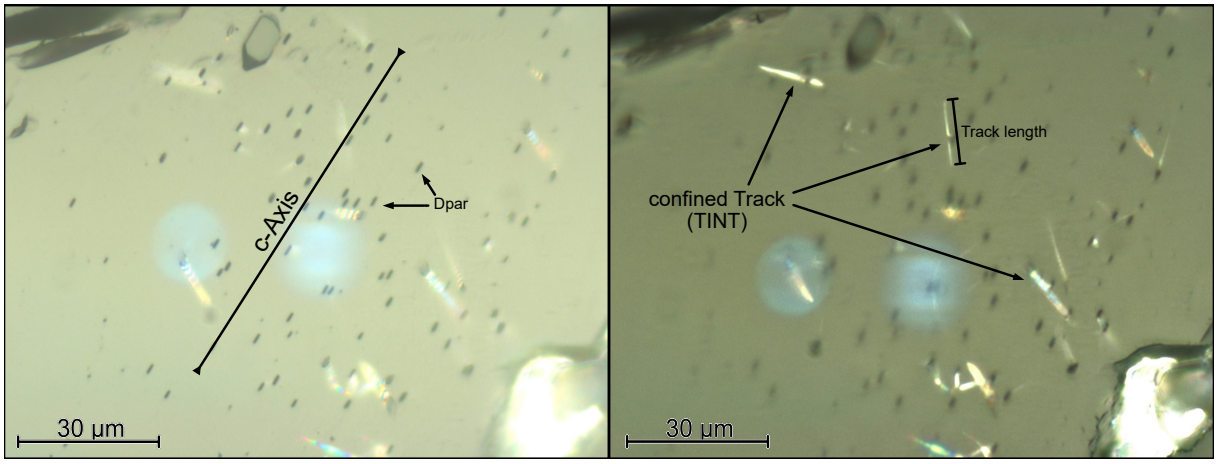

Fig. 4.2: Example (VAH-17) for Dpar and confined tracks, both pictures of same scale and frame under reflected light. Left: Focused on Dpars to identify the c-axis and measure Dpars, if Dpars are parallel to the c-axis the grain can be used for analyzing. Right: slightly zoomed in to highlight confined tracks. Each confined track shows both ends and allows for track length measurement.

measured track, three additional Dpars were measured.

4.2.5 Calculation of fission track ages

The software TrackKey vers. 4.2 (Dunkl, 2002) was used to calculate central ages, chi-square and p-values, dispersion and track densities as presented in table 5.2.

4.3 Thermal Modelling

For the thermal modelling, the software HeFTy 1.9.3 (Ketcham, 2017) was used. Inverse modelling for single-grain ages was applied to every sample. The software was fed with all the available data, including the calibration factors, measurements and countings. The chosen annealing model was by Ketcham et al. (2007). For c-axis projection Ketcham et al. (2007), 5.0M was followed, as this most resembles the etching procedure performed in this study. HeFTy 1.9.3 allows us to drawconstraint boxes through which the modelled Tt-path needs to go. These boxes were drawn according to the geochronological observations by previous studies (e.g. Ksienzyk et al., 2014; Wiest et al., 2021). The type of path was also modified to allow reheating to give the highest degree of freedom to the resulting path. The inverse modelling in HeFTy 1.9.3 uses the Monte Carlo search method to find fitting paths. For each sample, 100 000 paths were tried, before the modelling process was stopped. Paths that have a 'goodness-of-fit' (GOF) parameter >0.5 were drawn and are classified as 'good'. 'Acceptable' paths have a GOF of >0.05. Whilst 'good' paths show a high agreement with the provided data, 'acceptable' paths do not contradict the data. HeFTy 1.9.3 also provides the weighted mean of all drawn paths, based on their GOF.

4.3.1 Start and End constraints

Start and end constraints were chosen for each sample. Start constraints are taken from independent geochronological studies. Muscovite ^{40}Ar / ^{39}Ar ages by Young et al. (2011) on samples in the study area give an age of 395 Ma (T_C= ~450-400 °C) (Fig. 4.3a). Similar studies to this further sourth in Norway (Johannessen et al., 2013; Ksienzyk et al., 2014), chose constraints based on zircon fission track ages ranging from 320 to 230 Ma (Andriessen and Bos, 1986; Leighton, 2007) (Fig. 4.3b). However, Wiest et al. (2021) show that segments of the WGR show offset in crystallization ages, indicating that younger constraints might need to be chosen. Redfield et al. (2004) report an entry age of 200 Ma for their AFT models at the MTFZ. The end constraints for all models are based on the present-day temperature measurements

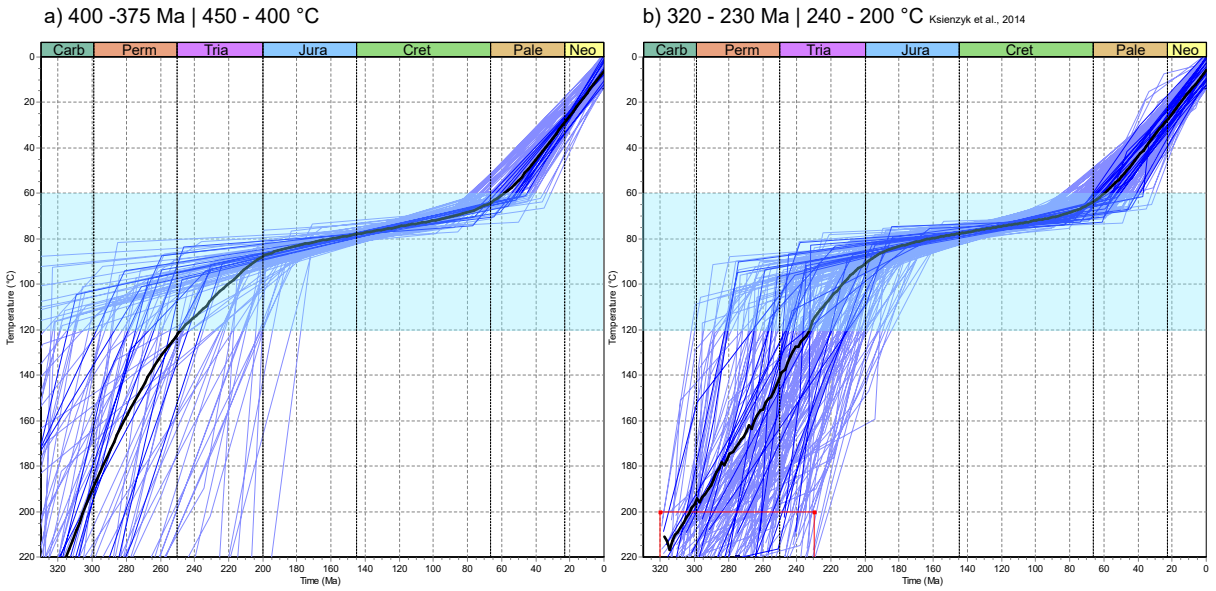

Fig. 4.3: Comparision of start constraints highlighted in red. VAH-01 used as example: a) Start constrain based on ^{40}Ar / ^{39}Ar ages by Young et al. (2011) and Wiest et al. (2021), starting contrain is out of boundary b) Start constrains based on zircon fission track ages as in Ksienzyk et al. (2014), dark blue: Good path; light blue: acceptable path; Blue shade = PAZ; black line: weighted mean average. Note that the end constraint was chosen -2 to 14 °C as for all sample below 1000 m altitude.

(Aune, 1992). A local measurement station in Loen (39 m o.s.l., Fig. 1.1) reports present-day temperatures between -2 and 14 °C (from the year 1971-1988). These constraints were used for samples lower than 1000 m o.s.l. For samples above 1000 m o.s.l., measurements from the closest weather station at this altitude were taken. For Sognefjell (1413 m o.s.l.) temperatures between -10 to 6 °C (1978-1989) were reported.

Both models, as shown in Figure 4.3, show similar results, so for further models, the starting constraints as used in Ksienzyk et al. (2014) were applied, as they are more recent and produce a tighter result.

4.3.2 Bootstrapping for Inverse Modelling

A general suggestion for a stable thermal model states at least 100 TINT for each sample (Donelick et al., 2005), however only in two samples this goal was reached (5). To counter the problem of few confined tracks, one might want to go back to a sample and remeasure tracks to increase the total amount of measurements. However, this process is time-consuming and is susceptible to bias. To circumvent this, a fairly simple code was written, that resamples measured tracks (and their respective <C and Dpar) randomly and alters their length between ± a given value. This is repeated until the sample size equals 100 tracks (incl. original ones). The main concern here is which value to choose to achieve the most resemblance

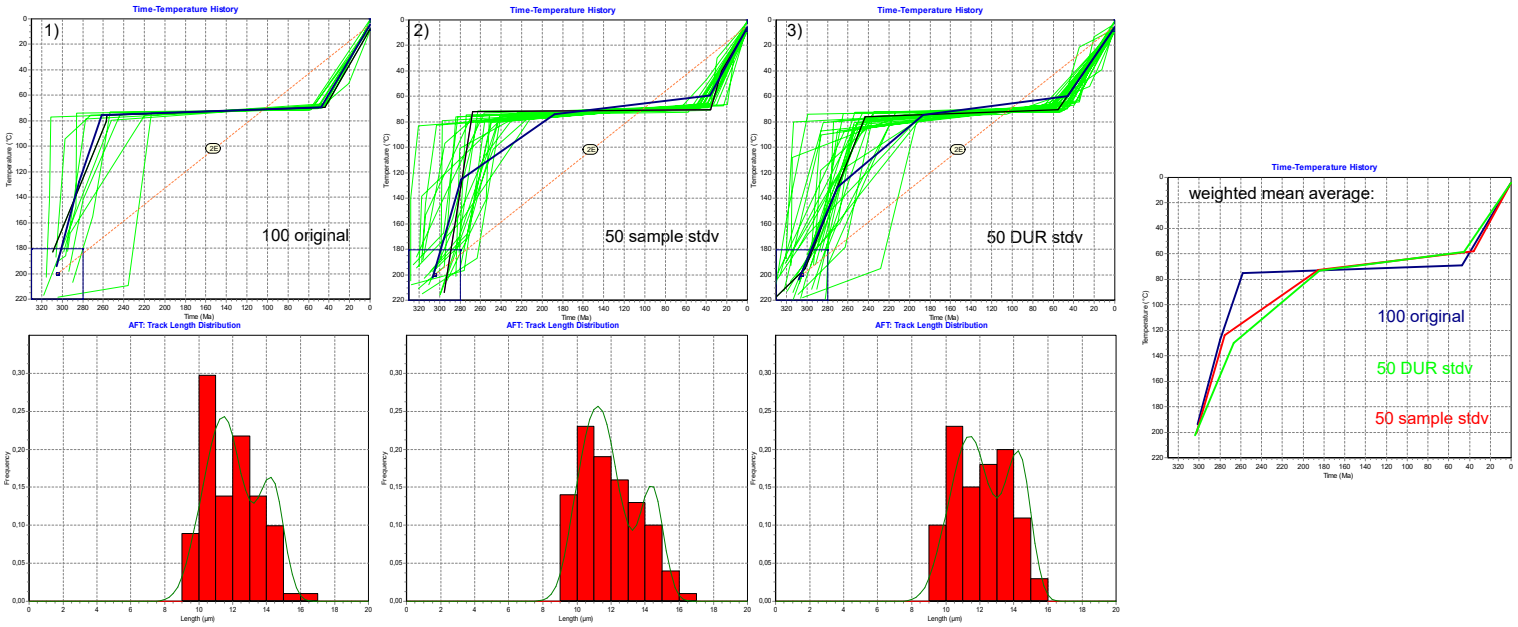

Fig. 4.4: Comparison of bootstrapped results with corresponding track length distribution for sample VAH-01. x-axis = time [Ma] and y-axis = temperature [°C] Green lines=acceptable paths, purple lines=good paths, thick black line=best path; blue line=weighted mean average (also displayed on the right-hand side): 1) modelling result of the original dataset. 2) Result with 50 original measurements and 50 additional ones based on the samples standard deviation. 3) Results with 50 original measurements and 50 additional ones based on 0.2 µm length variation simulating physical remeasuring. Right: comparison of the modelling results with the weighted mean-average of each modelling experiment

to actual data.

To test this, different models were set up by using sample VAH-01 where 100 tracks were measured: 1) 100 measured tracks (VAH-01); 2) 50 measured tracks and 50 additional ones were modelled using the standard deviation (stdv) from the sample itself (~2 µm) and 3) modelling 50 tracks using a value that simply takes re-measuring precision into account (±0.2 µm; e.g. Carlson et al., 1999). The modelling results are compared using their weighted means (Fig. 4.4).

The gathering process for additional tracks using modelling is much quicker and avoids any kind of bias compared to manual remeasuring with the potential of tracks being generated that are possible, but not available in the physical sample. Its left to argue, how beneficial this in a completely probability based system is. Whilst the stdv of the individual sample (model 2) basically "invents" new tracks that could theoretically be found, the choice of value only slightly affects the resulting distribution and testing so far showed that even bimodal distributions remain bimodal. This approach, however, still requires an initial sample size of at least 20 tracks for HeFTy 1.9.3 to produce any Tt-paths. Richard Ketcham however, showed concerns as this approach creates an improper sense of precision (personal email correspon-

dans). Samples with low track counts are supposed to have wider confidence and fabricating new tracks constrains the model in a completely artificial way. For example model 2 shows a higher constrain due to the introduction of some odd tracks as an effect of a larger stdv. Model 3 under-sampled parts of the histogram compared to the full-data model 1) and is therefore slightly less constrained. Ketcham points out that the 100-track aim is a rather arbitrary and statistical test used within HeFTy 1.9.3 will provide a solid model, even with track counts lower than 50.

4.4 Lineament mapping

For remote sensing, the Software QGIS (vers.3.16) was used. A frame of 1:200000 over the study area was chosen for lineament mapping. The lineaments were mapped with the help of hillshades, digital elevation models (DEM) and orthophotos. Only incisions were mapped, meaning only negative landscape features and no ridges. Every lineament was aimed to follow as far as possible under consideration of the terrain, but not of previously drawn lineaments. Lineaments were also extended beyond the marked study area, to reflect the true extent of each lineament. Once most lineaments in a 1:200000 frame were mapped, the same area was post-processed on a scale of 1:100000, correcting lineaments and adding smaller ones. Note that a hillshade makes the detection of lineaments easier, however due to its nature, hillshade illuminates SW facing surfaces and darkens NE facing surfaces and therefore decreases the visibility on these surfaces for lineaments. Since most incisions tend to have at least one area that is not facing one of those general directions, a hillshade is still a viable tool, but this cause for distortion has to be taken into account. The orthophoto was consulted to correct for possibly ‘hidden’ lineament. Lineaments were categorized after size. Fjords and large valley as major lineaments, conjugate valleys and clearly visible lineaments as moderate lineaments and less pronounced features as e.g. faults and joints as minor lineaments. Creeks and other smaller fluvial induced formations were avoided.

Chapter 5

Results

The results of field observations, laboratory analysis as well as modelling efforts are presented in this chapter. Every uncertainty is given in the 1σ-level confidence.

5.1 Field observations

The sample localities consisted of massive monzonite with augen texture. Figure 5.1 shows 5 of the sample localities (VAH-01;-02;-03;-04;-06). Based on their mineral composition they are classified as monzonite (<5 % Quartz). VAH-01 was collected at a roadcut in an N-S trending valley west of Byrkjelo (Fig. 5.8). The sample locality is hetereogenous with layering showing varying augen density, whilst the clast follows the foliation (322/38). The size of the augens varies from mm to ~5 cm, however, they stay more or less uniform in size within one layer. The matrix is darker and contains amphiboles. VAH-02 was collected in an N-S trending valley east of Bykjelo (Fig. 5.8) at a small outcrop along a small river bed. This location showed large cm-scale K-feldspar augens. The gneiss is foliated, with a dark matrix. However, no layering was observed. VAH-03 was found along a roadcut between Utvik and Invik close to the E-W trending fjord (Fig. 5.8). This sample showed a similar composition to the other samples, however showed a more strained texture and a slightly greenish matrix. The augen shaped varied significantly within the outcrop, at some stages showing rather bands than augens. VAH-04 was found at a parking lot at the end of the N-S trending Olden valley. The gneiss appeard very similar with K-Feldspar augens and a dark-greenish matrix. VAH-05 and VAH-06 was sampled on either side of the NW-SE trending Loen water (Fig. 5.8). VAH-06 represents the lowermost sample of the Skåla profile. This sample shows large (1 - 3 cm) K-feldspar augen, though whitish due to weathering. The augen-density is significantly higher in VAH-06 than in other samples, therefore showing less matrix. However, the matrix appears just as green as in other samples. VAH-06 shows only a weak foliation. The

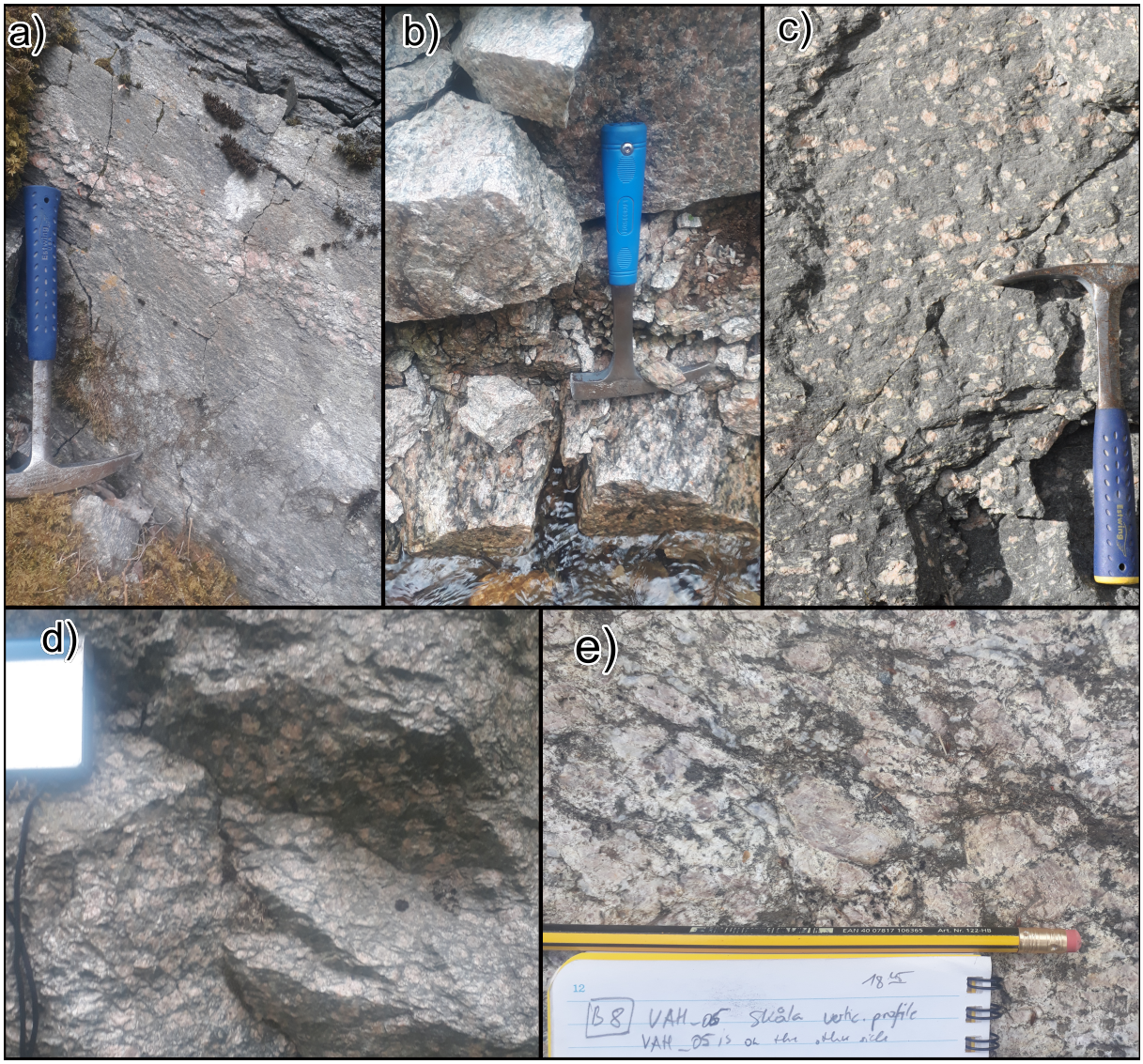

Fig. 5.1: Pictures of outcrops at which samples of this study were taken. a) Sample VAH-01 with a layering of varying augen density, hammer for scale. b) VAH-02, hammer for scale. c) VAH-03, hammer for scale (picture by Åse Hestnes). d) VAH-04, compass for scale. e) VAH-06 at the base of the Skåla profile, pencil and A5 field notebook for scale. More details in the text.

Skåla mountain is earlier mapped as a homogenous massive of monzonite (NGU). Sampling the profile (VAH-06 to VAH-19) confirmes this. The monzonite is similar to that of VAH-06, where some of the samples show a higher degree of shearing (e.g. VAH-19) at higher altitude (personal comment by Åse Hestnes).

5.2 Lineament mapping and remote sensing

Lineaments that were already observed in the field (e.g. Fig. 5.2) were successfully recognized with a Geographical Information System (GIS) . In total 106 lineaments were mapped (Fig. 5.3). The mapped lineaments were measured with QGIS 3.16 to infer length and direction (Fig. 5.4).

The rose diagrams (Fig. 5.4A) show that most lineament strike NW-SE. NE-SW is also a prominent direction, however with a larger spread in direction. Minor lineaments in the study area strike mostly NW-SE to NNW-SSE (and also NE-SW) and form the majority of observed lineaments. Though more common, NW-SE lineaments show smaller extent and are more common between major N-S valleys, to the N-E of the study area and within the Caledonian Nappes. The longest lineaments are up to 25 km long and follow a similar trend with two additional lineaments striking E-W (Fig. 5.4B). These two lineaments also highly influence the course of the Nordfjord itself (Fig. 5.3).

5.3 Pre-analytical calculations and calibrations

5.3.1 Neutron flux gradient ρ_D

The irradiation container included 37 positions with four IRRMM-540R standard glass mica detectors placed with equal spacing. All analyzed samples are included in this container (labelled as NoB-29). To monitor the neutron flux ρ_D through the sample container every detector was counted three times (Fig. 3.2). The values for ρ_D show a linear decreasing gradient from first to the last position. A complete list of ρ_D values at each position and their respective sample can be found in Appendix A.

5.3.2 Zeta calibration

A personal Zeta-value of 213.85 ± 4.19 was inferred by analyzing and calculating the weighted mean of 13 Durango or Fish Canyon standards, including NoB-29. A summary of the standards Zeta values can be seen in figure 5.6 and is presented in more detail in table 5.1.

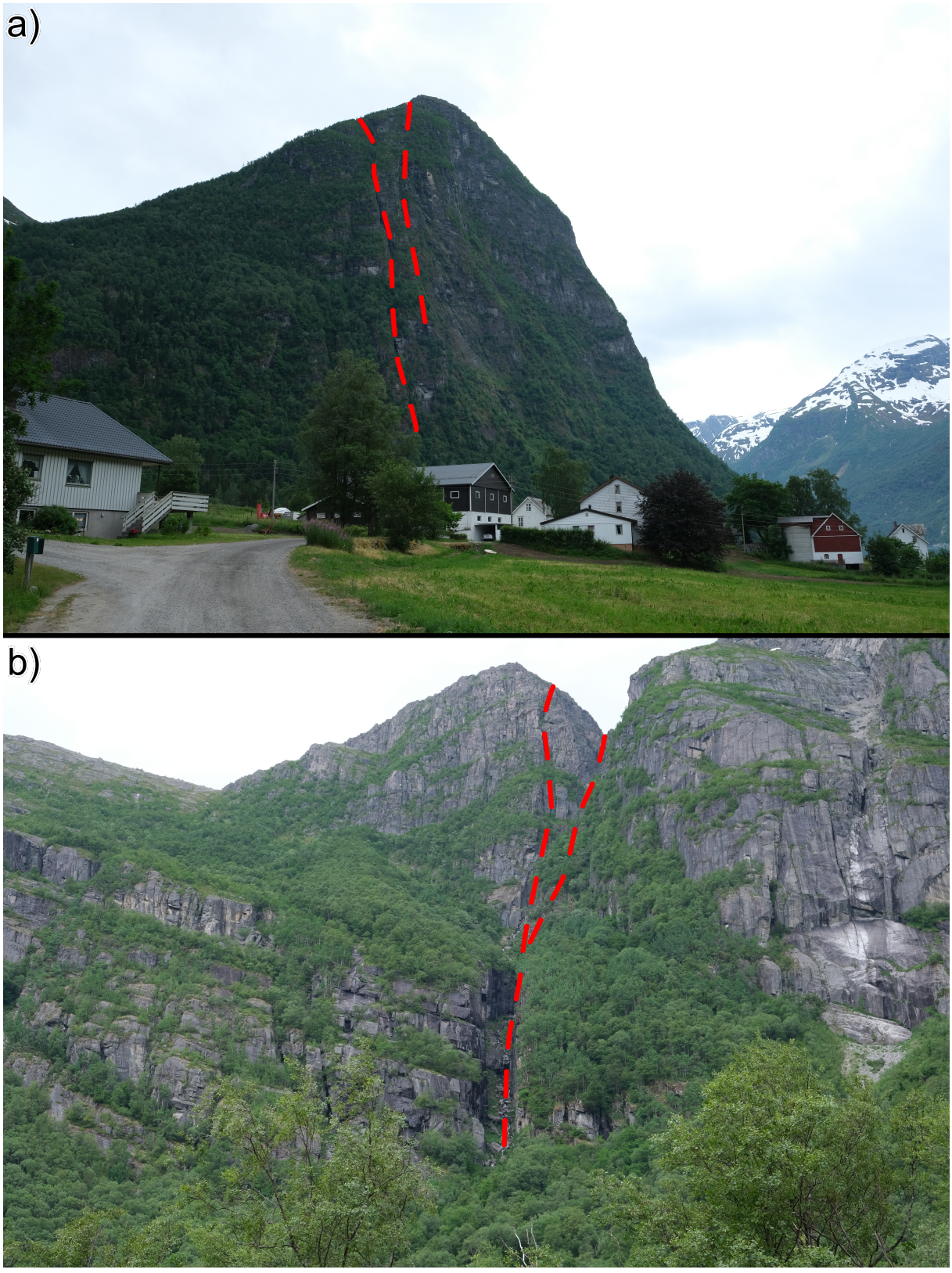

Fig. 5.2: Example lineament in Olden valley (N-S trending) with highlighted fractures (red). Lineament is parallel to the valley direction. Lineament can be traced from location a) to b). a) Kjenuken, facing south. b) close to Briksdalsbreen, facing north.

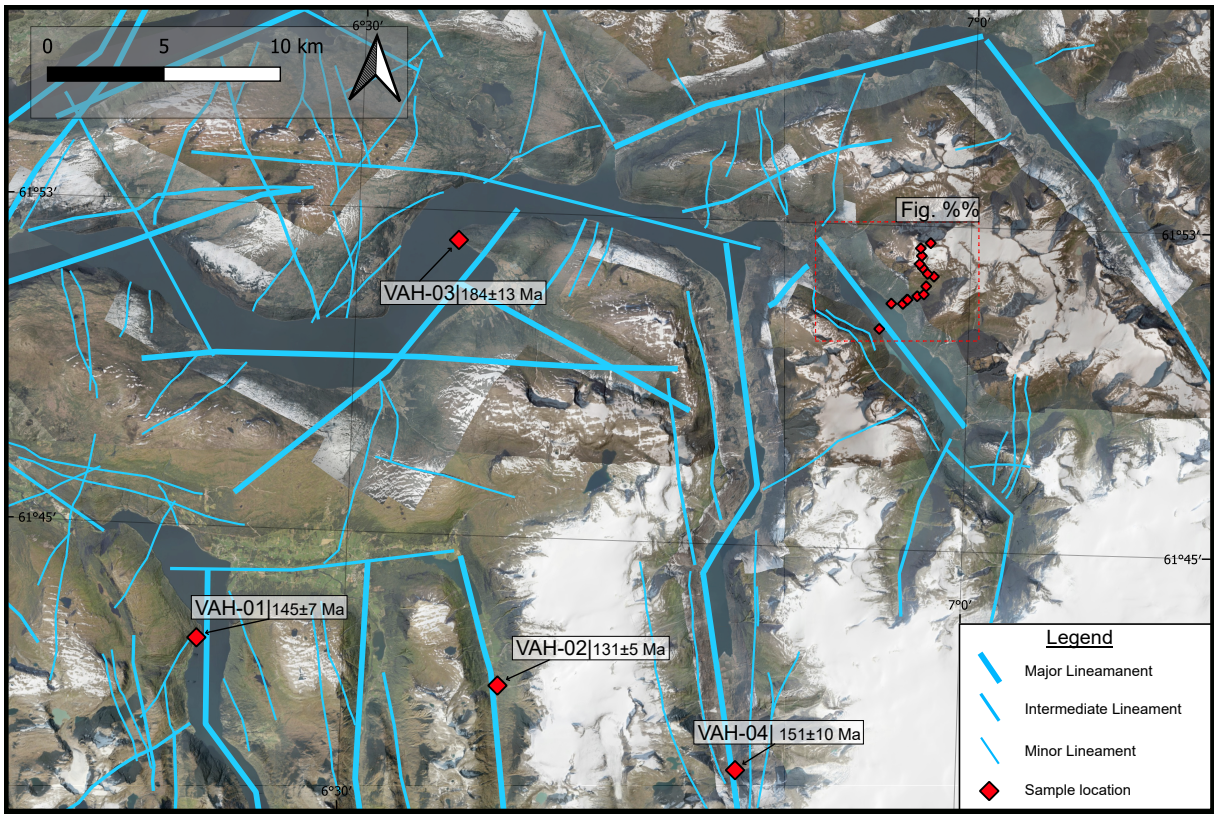

Fig. 5.3: Study area with mapped lineaments (blue) and sample locations. Lineaments were classified into three categories according to their size and visibility. Ortophoto by Norgeskart.no

Irradiation	Standard	Grains	Counted Tracks		Dosimeter		Zeta			
		(n)	N_s	N_i	ρ_d (10^5)	N_d	ζ	±	1σ	weights
NoB-14	Durango	20	339	1843	17.304	31550	197.8	±	12.2	0.0070
NoB-14	FCT	24	345	1854	17.374	31550	173.0	±	10.7	0.0092
NoB-17	Durango	20	246	2212	17.508	24201	323.4	±	22.4	0.0020
NoB-17	FCT	21	276	1796	17.428	24201	208.8	±	14.1	0.0052
NoB-20	Durango	20	329	2331	20.606	27417	216.5	±	13.3	0.0059
NoB-20	FCT	20	266	1987	20.474	27417	204.0	±	13.9	0.0054
NoB-21	Durango	21	354	2337	18.391	40204	226.0	±	13.4	0.0058
NoB-21	FCT	25	248	2240	18.317	40204	275.8	±	19.2	0.0028
NoB-22	Durango	20	412	2421	19.600	42903	188.7	±	10.5	0.0094
NoB-22	FCT	22	204	1668	19.574	42903	233.6	±	16.9	0.0036
NoB-29	Durango	23	342	2248	15.853	25912	261.1	±	15.8	0.0042
NoB-29	FCT1	20	80	507	15.773	25912	224.7	±	27.4	0.0014
NoB-29	FCT2	20	121	754	15.694	25912	225.8	±	22.5	0.0020

Tab. 5.1. Results of Zeta calibration for each AFT standard. Every sample was analyzed using the external detector method (see. Sec. 3.1.7). Following ages were applied in the calculations: Durango (Dur) = 31.4 ± 0.5 Ma (Mcdowell and Keizer, 1977), Fish Canyon Tuff (FCT) = 27.9 ± 0.5 Ma (Hurford and Hammerschmidt, 1985).

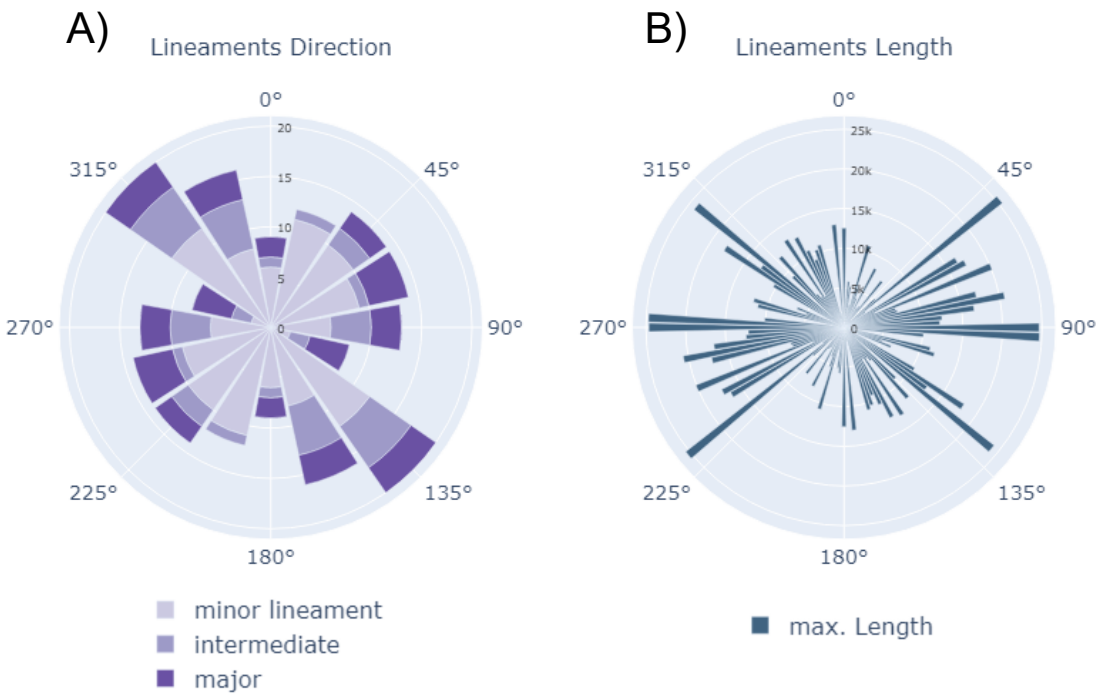

Fig. 5.4: Rose diagram showing direction and length of mapped lineaments. A) Number of lineaments in direction with sub-classification according to their size and visibility. Dark blue represents the longest, normal blue are intermediate and light blue are the smallest lineaments. B) Displays the length of lineaments with their respective direction .

5.3.3 Length calibration

The arithmetic mean of 100 tracks in Durango standards, as well as their Dpars, were put in relation to the measurement from the literature presented in Ketcham et al. (2015). The inferred average length of Durango tracks is 15.37 ± 0.89 µm. The simple ratio $L_{published}/L_{this}$ study equals 1.03, meaning on average my measurements are about 3% shorter, than of the average scientist (15.84 ± 0.61 µm). The same principle was applied for Dpar measurements resulting in a factor of 1.37. These values were included in the modelling as a correction factor. For track lengths, only 19 literature values were available, and for Dpar measurements seven literature values.

5.4 Apatite Fission Track analysis

In total 19 samples were analyzed using AFT. Fourteen of those are part of the Skåla profile. The other five samples are taken close by the Nordfjord. The results are presented in the following sections.

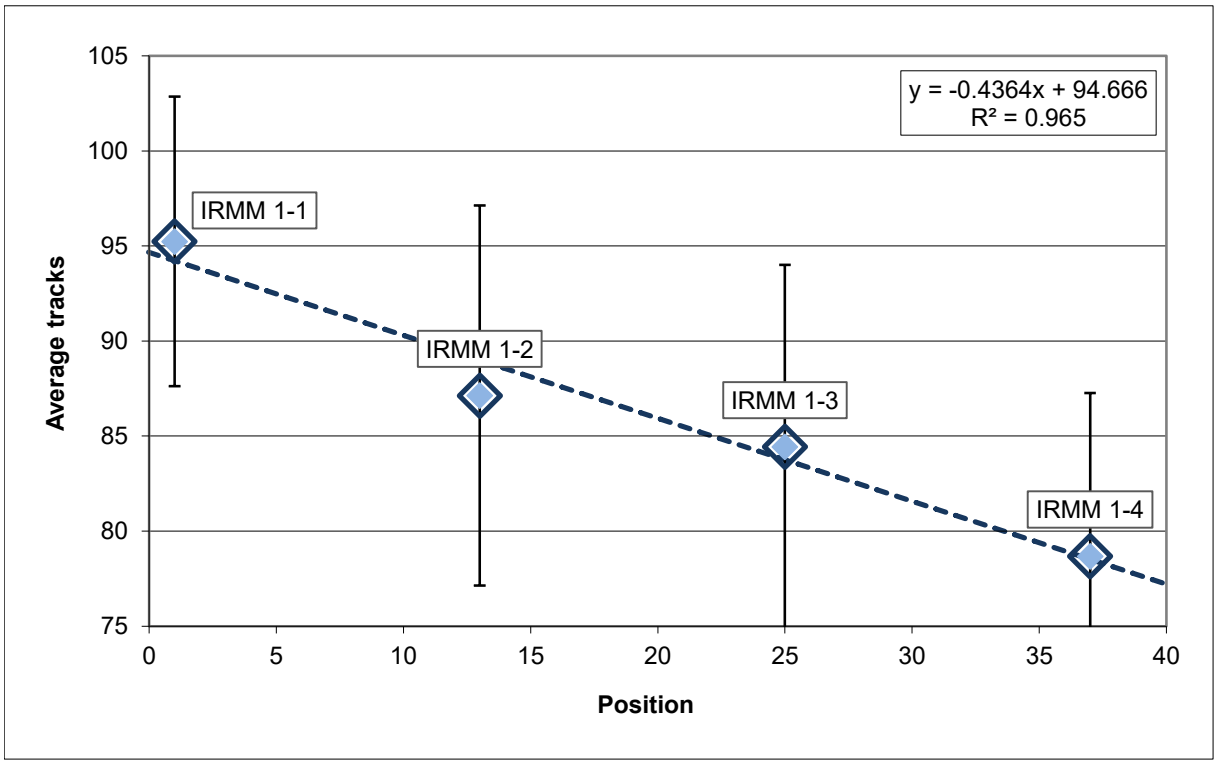

Fig. 5.5: Average tracks over container position in NoB-29. IRMM detection micas plotted with corresponding regression. The regression equation and R^2 coefficient is given in the upper right corner. The value of ρ_D is inferred from the regression equation. IRMM 1-1 shows the highest values of ρ_D as it is closest to the neutron source during irradiation.

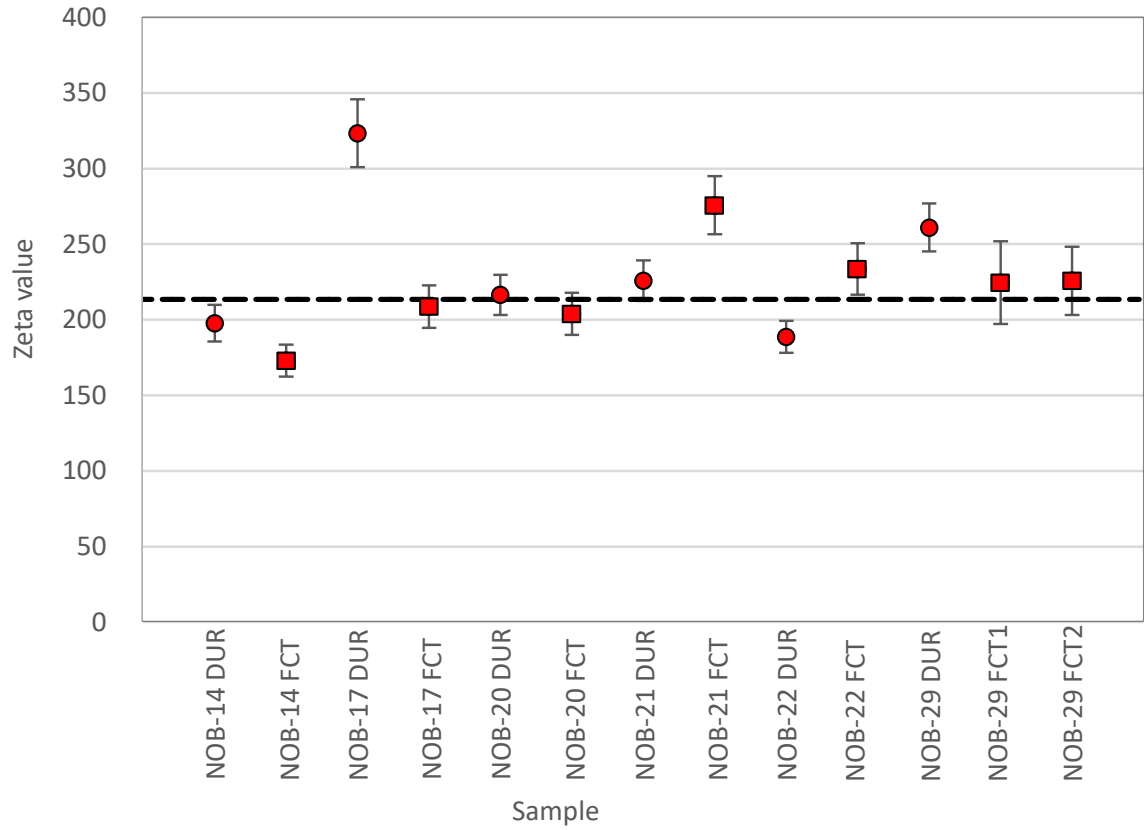

Fig. 5.6: Individual Zeta values for each standard with 1σ error bar. Points = Durango (DUR), Squares = Fish Canyon Tuff (FCT). Dashed horizontal line shows weighted mean Zeta, derived from all samples Zeta using the inverted error of these as weight. Samples with a larger error are therefore less weighted in the mean.

5.4.1 Apatite description and quality

The quality of the grains was assessed during the counting process and graded for each individual grain. It was differentiated between poor (P), fair (F), good(G) and great (Gr) quality. Most grains are of fair or good quality. Most grains are fairly large (~30 μm), most often elongated but rarely euhedral. Some apatites appeared partially opaque (e.g. severely darkened, with dark stripes), hampering the counting of fission tracks. In some cases, apatites were completely opaque, especially common in sample VAH-16, making counting these apatites impossible (Fig. 5.7). For this reason, VAH-16 is the only sample where less than 20 grains could be counted. Features like fractures, dislocations, inclusions and zonation were noted in the counting sheet (Appendix A). Fractures were common in all samples. Fractures can obscure the counting area and prohibit accurate counting. When counting, fractures were avoided and instead smaller counting areas were chosen. Some grains showed dislocations that can be confused with tracks, however easy to detect by their repeating nature. Inclusions were in most cases avoided, though it also never led to anomalous high ρ_i values, otherwise the grain would have been rejected. The occurrence of zonation varies throughout the samples, however with more zonations in the upper part of the Skåla profile. Zoned apatites always show uranium-rich cores, with a high value of ρ_s and a depleted rim (Fig. 5.7). The rim usually showed hardly any track at all. The respective print would also show an elevated ρ_i in the core and lower values in the outer rim, confirming alignment in the process. Weak zonation may occur when the track density of the inner zone is not significantly elevated and the boundary is not easily traceable. During counting the core was consistently counted, however for the AHe data and ejection correction this must be considered. The average grade from each grain gives an estimate of the quality of the sample as given in table 5.2. Most samples are of fair or good quality and don't vary much in general. VAH-18 tend to have the best preserved apatites. VAH-16, as already mentioned, has in particular poor apatites (Fig. 5.7). All samples show a very low U-concentration, with a mean of 7.33 ppm. VAH-02 has the highest U-concentration (17 ppm) and was the only sample where 100 confined tracks could be found without an additional mount (Sec. 5.4). In addition to apatite quality, the mica showed in rare instances a roughened or uneven surface which obstructed the counting. Furthermore, several zircons were found on some mounts, showing a very euhedral shape, usually larger than the average apatite with clearly visible zonation, typical for non-metamorphic zircons.

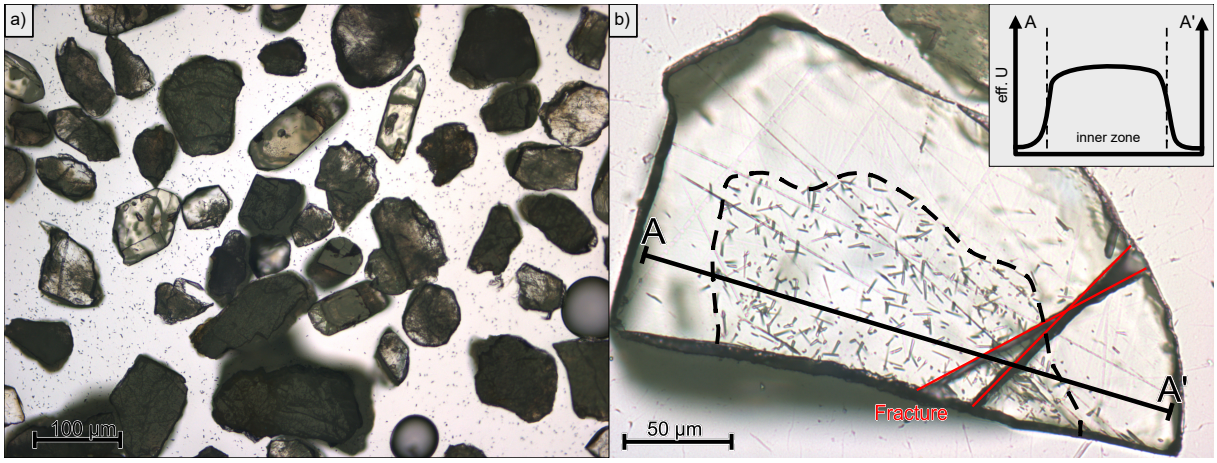

Fig. 5.7: Examples for grain quality: a) VAH-16 poor quality grains, almost opaque making track observation difficult to impossible, also contains (zoned) zircons (mag.: x125). b) VAH-19, zoned apatite with fractures (red), inner zoned marked with dashed lines, indicated profile (A-A') in the upper right corner, the inner zone has an elevate ρ_s and had, therefore, a higher effective uranium concentration than the outer zone, only the inner zone was counted in zoned apatites (mag.: x625).

5.4.2 Age measurements

The measured AFT ages of the 19 analyzed samples range between 121 Ma and 232 Ma, covering ages from Upper Triassic and Lower Cretaceous and are displayed in table 5.2. As expected, younger ages were found at lower elevations and older ages tend to be at higher elevations. The oldest age VAH-12 (232 ± 15 Ma) however, can be found in the middle part of the Skåla profile (see Sec.5.4.4). For each sample at least 20 grains could be found. The only exception is VAH-16, because of lacking grain quality, as discussed above. To gain 20 grains, even grains with only a small countable surface area (25%) had to be counted (e.g. VAH-13). In other samples, 20 grains were easily found and even more were documented (e.g. VAH-11) (see also Appendix A). The track density ρ_s is rather low for all samples, with an average of 8.35 with a similar result for the induced track density (8.17). Almost every sample passes the chi-square (χ^2 >5%), except sample VAH-13. VAH-13 also shows by far the highest dispersion in single grain ages and the highest standard deviation for central age (see Table 5.2). A failed chi-square test can be indicative for two or more age populations within the sample. In non-sedimentary rocks is a failed chi-square test rather unusual, but can be explained by varying chemical composition, poor alignment of mount and mica, inconsistent counting or simply contamination. No evidence for false measurements were found, so the sample needs to be taken by face value, though viewed critically. Dpar measurements range from 1.34 (VAH-14) and 1.66 (VAH-12). That indicates that the solubility (i.e. chemistry) of the samples is comparable, as well as their inferred ages. This outcome was expected since most samples were taken within a small area and are of the same lithology.

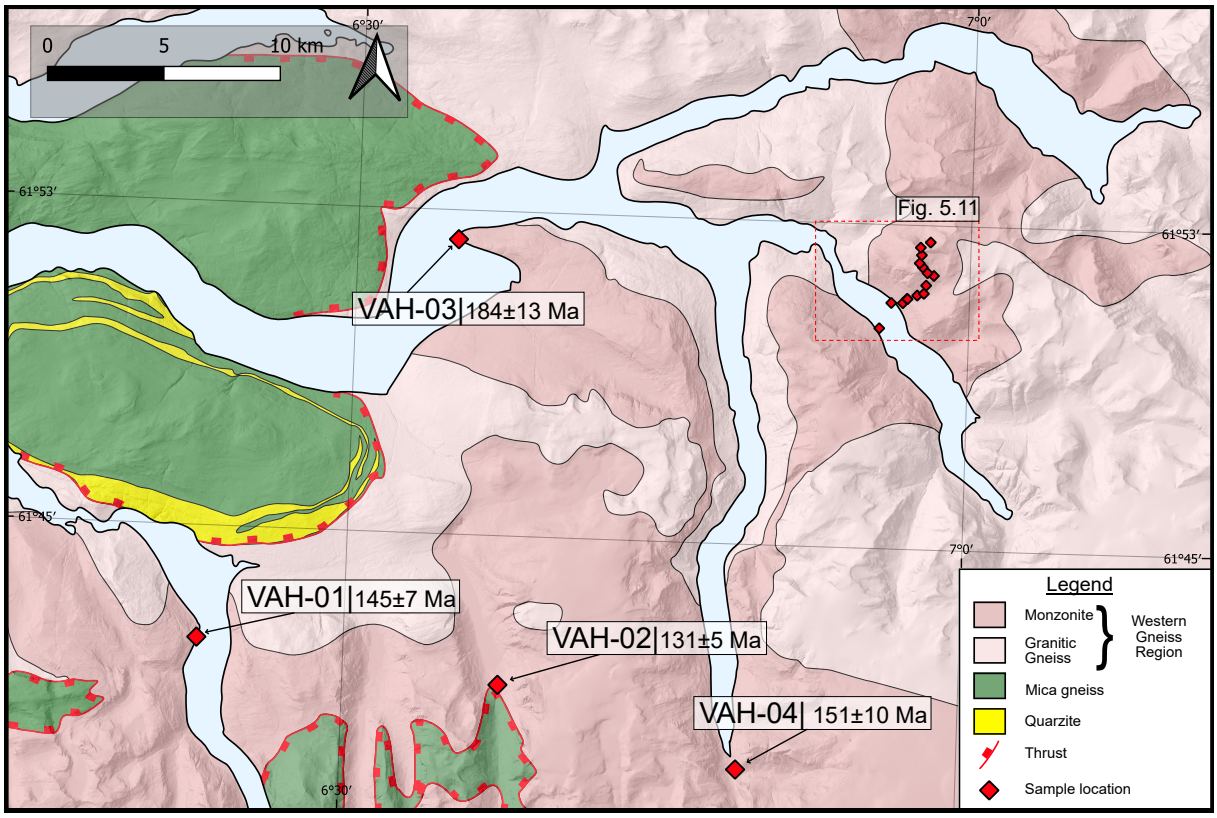

Fig. 5.8: Simplified lithological map of the study area with sample locations and their respective ages. A detailed view of the Skåla profile can be seen in figure 5.11. Elevation and lithological data by NGU

Sample	Location	UTM 32N		Elevation	Lithology	Sample	n	Spontaneous		Induced								Central Age		Measured		C-Axis Proj.		
		Easting	Northing	[m]		quality	(G)	ρ_s	N_s	ρ_i	N_i	ρ_d	N_d	P(χ^2) [%]	Disp.	U [ppm]	Dpar [µm]	±1σ [µm]	**Age [Ma]**	**±1σ [Ma]**	MTL [µm]	±1σ [µm]	MTL [µm]	±1σ [µm]	n (T)
VAH_01	Breimsvatnet	361526.17	6844294.64	95	Monzonite	F;f,(i),(d),(z)	(20)	9.84	1402	12.36	1762	17.128	25912	14	0.08	9	1.42	0.06	**145**	**7**	11.2	2.3	12.6	1.6	102
VAH_02	Myklebustdalen	374453.74	6842224.12	413	Monzonite	G;f,(i),(wz),(d)	(24)	16.96	3000	13.55	4166	17.048	25912	18	0.06	17	1.44	0.09	**131**	**5**	9.9	2.7	12.0	1.5	101
VAH_03	Hildaneset	372802.13	6861358.65	30	Monzonite	G;f,(i),(d),(z)	(20)	3.28	483	3.18	469	16.969	25912	26	0.09	3	1.51	0.09	**184**	**13**	9.7	1.6	11.5	1.4	2
VAH_04	Brenndalen	384658.00	6838590.05	160	Monzonite	F;f,i,(wz)	(21)	3.73	577	4.46	691	16.889	25912	17	0.10	4	1.42	0.12	**151**	**10**	8.4	2.7	10.8	1.6	5
VAH_05	Skåla	390851.25	6857535.49	60	Monzonite	G;f,(i),(z)	(24)	7.23	1275	9.91	1749	16.809	25912	14	0.09	10	1.38	0.13	**130**	**6**	11.1	2.4	12.4	1.7	61
VAH_06	Skåla	391367.80	6858623.05	63	Monzonite	G;f,(i),(d)	(27)	5.09	901	6.34	1121	16.730	25912	17	0.10	5	1.38	0.13	**143**	**8**	9.5	2.9	11.5	2.0	22
VAH_07	Skåla	391864.20	6858613.89	234	Monzonite	G;f,(i),(d),(wz)	(21)	6.28	910	9.25	1341	16.650	25912	9	0.12	8	1.40	0.08	**121**	**7**	9.7	2.6	11.3	2.0	37
VAH_08	Skåla	392044.48	6858796.13	396	Monzonite	F;f,d,(i),(wz),(z)	(20)	9.52	1216	9.48	1212	16.570	25912	35	0.05	8	1.40	0.15	**176**	**8**	11.1	2.4	12.5	1.8	47
VAH_09	Skåla	392066.79	6858787.18	410	Monzonite	F;f,(d),(i),(wz)	(20)	9.28	1140	10.54	1295	16.491	25912	48	0.05	9	1.59	0.19	**154**	**7**	10.4	2.7	12.1	1.7	43
VAH_10	Skåla	392482.28	6858940.96	618	Monzonite	F;f,(i),(z),(d)	(20)	3.13	331	3.02	319	16.411	25912	47	0.15	3	1.58	0.11	**182**	**16**	9.2	3.8	12.4	2.3	3
VAH_11	Skåla	392767.39	6859016.61	717	Monzonite	F;d,f,(wz)	(26)	7.92	1926	8.61	2095	16.331	25912	25	0.03	7	1.58	0.09	**159**	**6**	10.8	2.3	12.4	1.4	62
VAH_12	Skåla	392865.51	6859366.11	926	Monzonite	F;f,d,(wz),(i)	(20)	8.02	887	5.94	657	16.172	25912	22	0.11	5	1.66	0.20	**232**	**15**	10.2	3.4	11.6	2.6	30
VAH_13	Skåla	393198.50	6859782.17	1079	Monzonite	F;f,d,wz,(i),(z)	(20)	8.16	702	7.16	616	16.092	25912	0	0.27	7	1.45	0.15	**202**	**18**	10.9	2.7	12.5	1.8	39
VAH_14	Skåla	392925.20	6859901.18	1240	Monzonite	F;f,(i),(d),(z)	(20)	4.12	456	3.94	436	16.012	25912	69	0.02	4	1.34	0.15	**177**	**12**	11.6	0.6	13.0	0.5	3
VAH_15	Skåla	392722.34	6860150.33	1396	Monzonite	G;z,(f),(d),(i),(wz)	(21)	9.05	1401	8.52	1319	15.933	25912	84	0.00	7	1.45	0.09	**179**	**8**	11.7	1.9	12.9	1.5	33
VAH_16	Skåla	392590.10	6860323.47	1495	Monzonite	P;f,d,(i)	(12)	11.41	673	9.27	547	15.614	25912	15	0.12	8	1.53	0.15	**193**	**14**	11.4	2.7	12.8	1.7	17
VAH_17	Skåla	392681.82	6860670.60	1553	Monzonite	F;z,f,(i),(d),(wz)	(21)	6.99	842	6.05	728	15.534	25912	69	0.01	5	1.40	0.11	**189**	**10**	11.9	2.5	13.2	1.7	22
VAH_18	Skåla	392636.81	6860997.28	1691	Monzonite	G;(z),(f),(d),(wz)	(21)	13.12	1386	11.36	1200	15.455	25912	59	0.01	10	1.51	0.14	**188**	**8**	11.4	2.2	12.9	1.3	51
VAH_19	Skåla	393064.72	6861219.28	1841	Monzonite	F;z,f,(wz),(d),(i)	(22)	15.62	1420	12.30	1118	15.375	25912	18	0.10	10	1.48	0.09	**210**	**11**	12.3	1.6	13.4	1.2	43

Tab. 5.2. Results of all samples: Sample Quality: P=poor, F=fair, G=Good, f=fractures, i=inclusions, d=dislocations, z=zonation, wz=weak-zonation, letters in brackets indicate rare occurrence; n (G) - number of dated grains; $\rho_{s,\,i,\,d}$, track densities in 1 × 105 tracks cm^{-2}; $N_{s,\,i,\,d}$, number of tracks counted; P(χ^2) - p-value of the chi-square age homogeneity test (Galbraith, 2005); MTL - mean track length; n (T) - number of measured track lengths. The black line separates non-profile samples and profile samples of the Skåla profile.
Analytical equipment: Olympus BX51 optical microscope equipped with a computer-driven stage and the FT-Stage software (Dumitru, 1993); magnification of ×1250 during counting and a magnification of ×2000 for measuring Dpar and track lengths. At least five Dpar measurements were carried out on each grain that was counted and three Dpar measurements for each measured track length. Only TINTs (track-in-track) were measured and their angle with the c-axis was recorded. Fission track ages were calculated with TrackKey (Dunkl, 2002) using a zeta calibration factor of ζ = 213.85 ± 4.19 (F. Mayer-Ullmann).

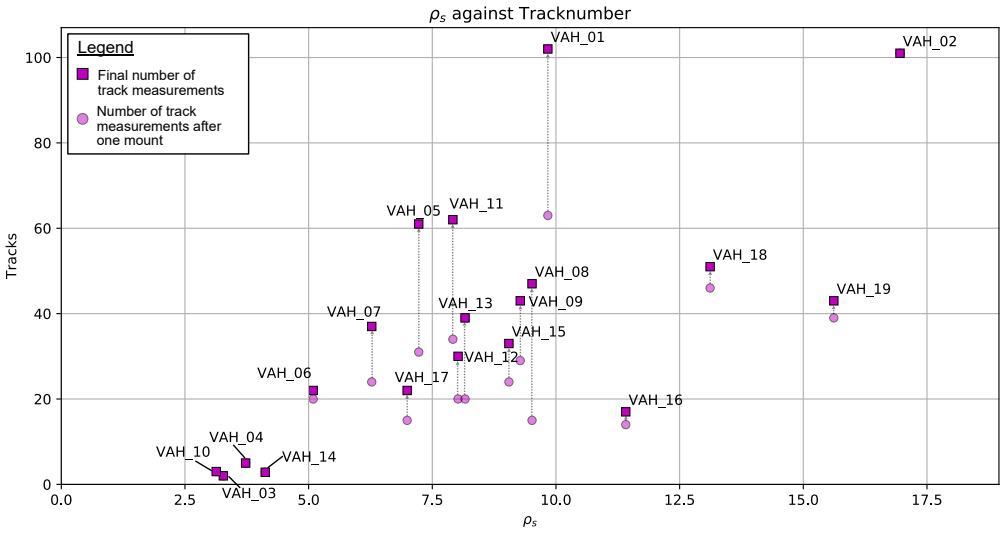

Fig. 5.9: ρ_s against track count. Results for one mount are shown shaded with a link to the final counting (incl. additional mount). The overall number of tracks found is mainly dependent on ρ_s, however is also affected by the number of grains and the surface area that allows for track measurements. The gain of counts is therefore dependent on the additional mount and grains on it.

5.4.3 Track length measurements

The occurrence of confined tracks is directly linked to the general track formation as these serve as pathways for the etchant. Mounts that show a higher track density ρ_s are more likely to yield more confined tracks. Another factor is the number of valid grains and surfaces available for track measurement, which can be increased by an additional mount. The relationship between ρ_s and the number of confined tracks is displayed in Fig 5.9. Due to a significant lack of confined tracks in the mounts, additional mounts needed to be prepared. These additional mounts were not irradiated and just etched according to protocol to reveal tracks. The alignment of these mounts was performed solely on the mount itself, without the use of a print. Other measurement criteria were kept consistent to guarantee comparability with tracks from the first mount. However, even with a second mount only in two samples more than 100 tracks were found (Table 5.2). VAH-02 yielded more than 100 tracks after measuring the first mount, so no additional mount was needed. VAH-03, VAH-04, VAH-10 and VAH-14 yielded less than 10 tracks in the first mount, so reaching a significant number of tracks in these mounts was not expected. These are also the samples with the lowest ρ_s.

The c-axis projected mean track lengths (MTL) range from 10.83 ± 1.53 µm (VAH-04) to 13.43 ± 1.24 µm (VAH-19) (Table 5.2). The MTL needs to be taken with care though, due to the low number of tracks in some of the samples that might not fully resemble the true population of the sample. However, plotted against elevation, a similar trend like the inferred age can

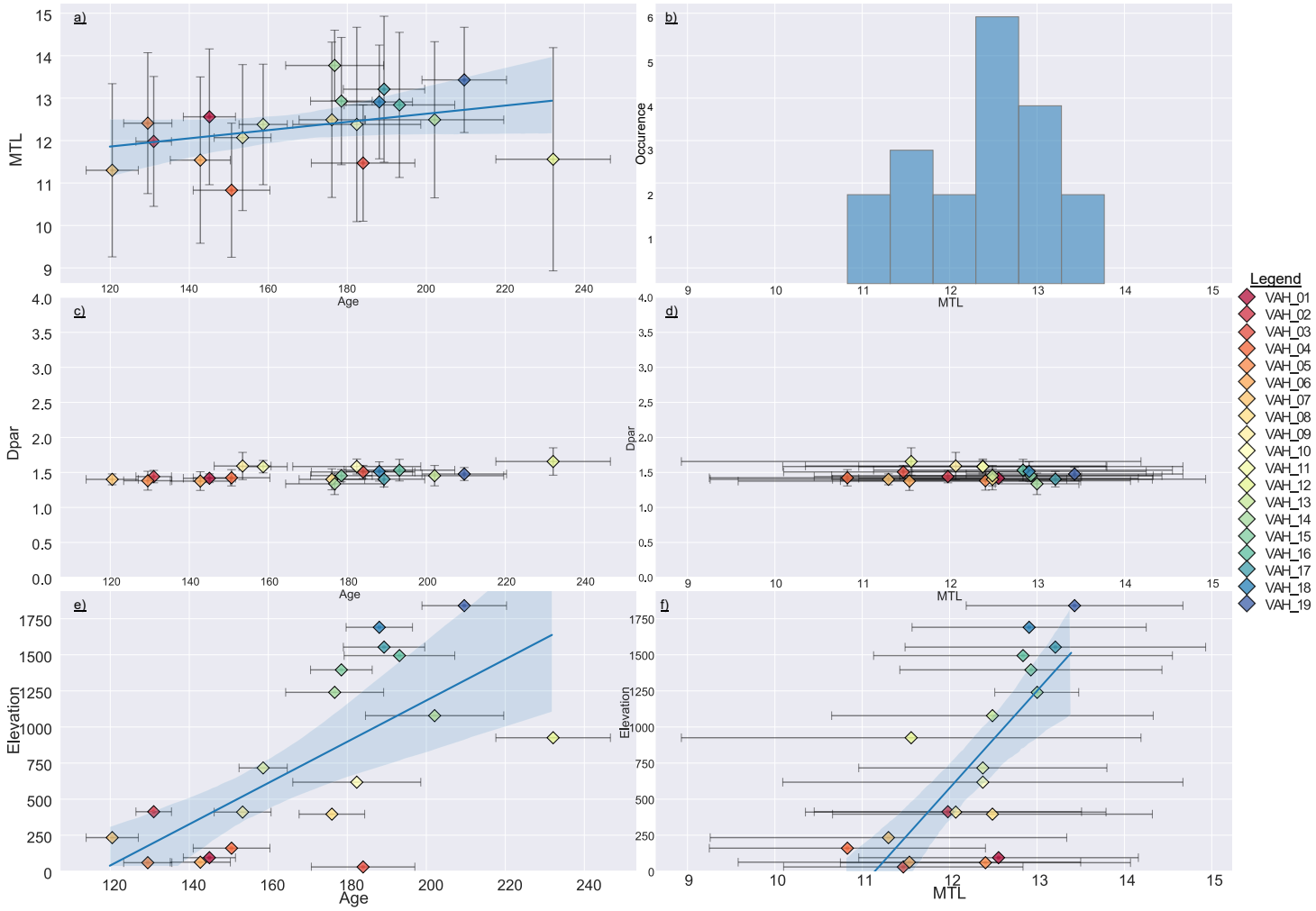

Fig. 5.10: Comparision of all samples (blue) with respective errorbars (1σ), regression (blue line) and 95% confidence interval (blue area). a) MTL show an increase with age, as it follows a similar trend with elevation. b) Histogram for mean track lengths. Most samples show a MTL between 12 and 13 µm which is in agreement with Redfield et al. (2005); Johannessen et al. (2013); Ksienzyk et al. (2014). c) Dpar over age d) Dpar over MTL. Dpar values remain generally unaffected. The y-axis was chosen to reflect the possible range of Dpar values (e.g. Donelick et al., 2005). e) Age against elevation f) MTL against elevation. As the age, MTL increases with elevation (for more detail see Sec. 5.4.4)

be seen (Fig. 6.2b). Both age and MTL show an increase in elevation. Dpar values remain mostly unaffected.

5.4.4 Skåla profile

The Skåla profile consists of the samples VAH-06 to VAH-19 located at the NW flank of the Skåla mountain. The lowest sample (VAH-06) is close to the fjord at 63 m a.s.l. whereas the highest sample (VAH-19) is located at 1841 m a.s.l. (Fig. 5.11, Tab. 5.2). VAH-05 was sampled close to the Skåla profile but on the opposite side of the fjord. An overview of the sample

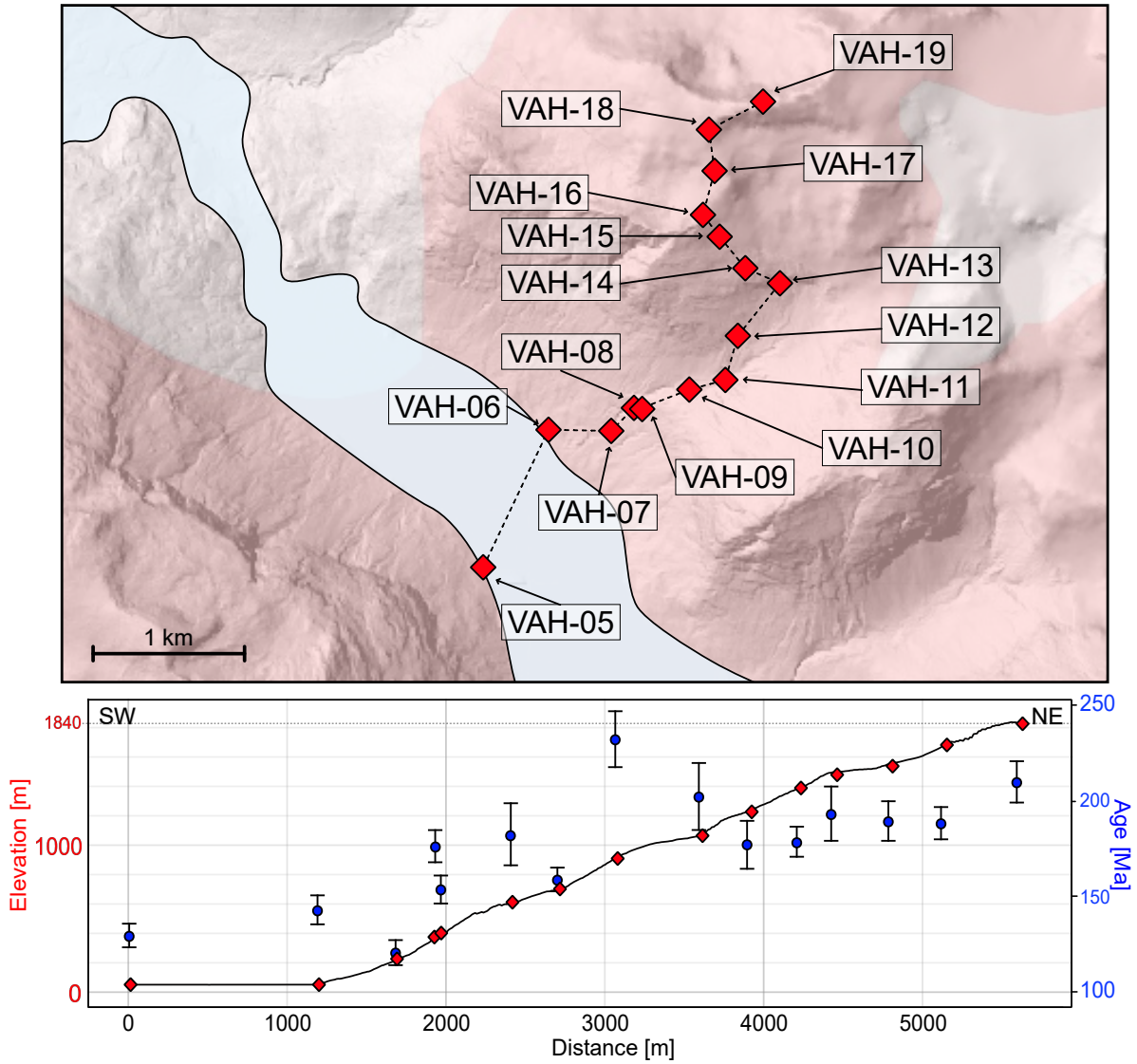

Fig. 5.11: Top: detailed Skåla profile with sample locations (red diamonds) with a hillshade map in the background to show topographic relief. The drawn profile is indicated by the dashed line. Bottom: Elevation profile with plotted locations and their respective ages (blue circles, 1σ error bars). Ages in more detail below. Lithology follows Fig. 5.8

location and vertical profile of the Skåla samples is given in Figure 5.11.

The ages increase with elevation by 3.3 ± 1.1 Myr/100 m (Fig. 5.12a). The lowest sample VAH-06 shows an age of 143 ± 8 Ma, the highest sample VAH-19 shows an age of 210 ± 11 Ma. Regression lines were drawn with y acting as an independent variable. The linear regression shows the increase in ages to elevation, however, samples VAH-12 and VAH-13 show an anomalous high age (Fig. 5.12a).

As well as the ages, the MTL increases with elevation (Fig. 5.12b). The MTL increases by ~0.1 µm/100m. Therefore MTL also correlates with increasing age. Older ages are linked to longer tracks. Samples VAH-12 and VAH-13 that show higher ages, however, don't show corresponding longer tracks.

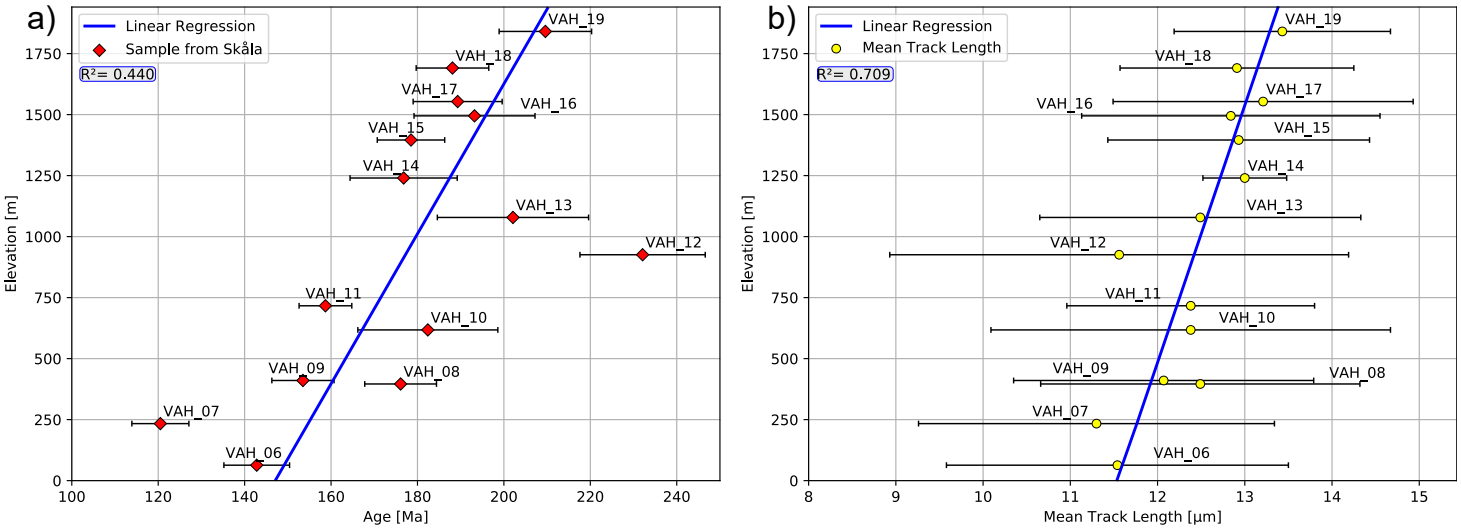

Fig. 5.12: a) Elevation over age for Skåla profile and 1σ errorbar. A clear increase in age with elevation is visible. Linear regression is provided in blue. The regression coefficient is given below the legend. b) Elevation over MTL for the Skåla with linear regression (blue line) and 1σ errorbar. MTL increases with elevation. Higher samples tend to have longer tracks i.e. faster exhumation through the PAZ. The regression coefficient is given below the legend.

5.5 Thermal history modelling

Almost all samples could be modelled successfully. In total 14 samples had enough confined track length measurements to produce a comprehensive thermal model. The fewer confined track measurements that contribute to the thermal model, the less constrained and inconclusive thermal history. Models for all samples are enclosed in the Appendix B. Cooling rates are based on generous estimations of weighted mean average paths, presented in all models.

5.5.1 Non-profile samples

Three out of five samples (excluding the Skåla profile) could be successfully modelled. VAH-01, VAH-05 and with moderate success VAH-04 (Fig. 5.13). VAH-01 shows an initial rapid cooling ~0.9 °C/Myr until the Triassic-Jurassic boundary at ~87 °C and cools into the PAZ at about 230 Ma. The sample remains in the PAZ and cooling plateaus to ~0.2 °C/Myr until the beginning of the Cenozoic. Shortly after, the sample leaves the PAZ and experiences rejuvenated cooling of ~0.9 °C/Myr until present (Fig. 5.13). VAH-05 describes a similar path with initial cooling of ~0.8 °C/Myr. The sample enters the PAZ roughly 210 Ma and cooling proceeds until Upper Jurassic. The cooling rate decreases in the PAZ to ~0.2 °C/Myr leaving the PAZ shortly after the Cretaceous. Subsequently, the cooling accelerates to ~1.0 °C/Myr until present (Fig. 5.13). Unlike VAH-01 and -05, VAH-04 yielded only 5 track measurements. Hence, the thermal model was less constrained. An overabundance of acceptable paths

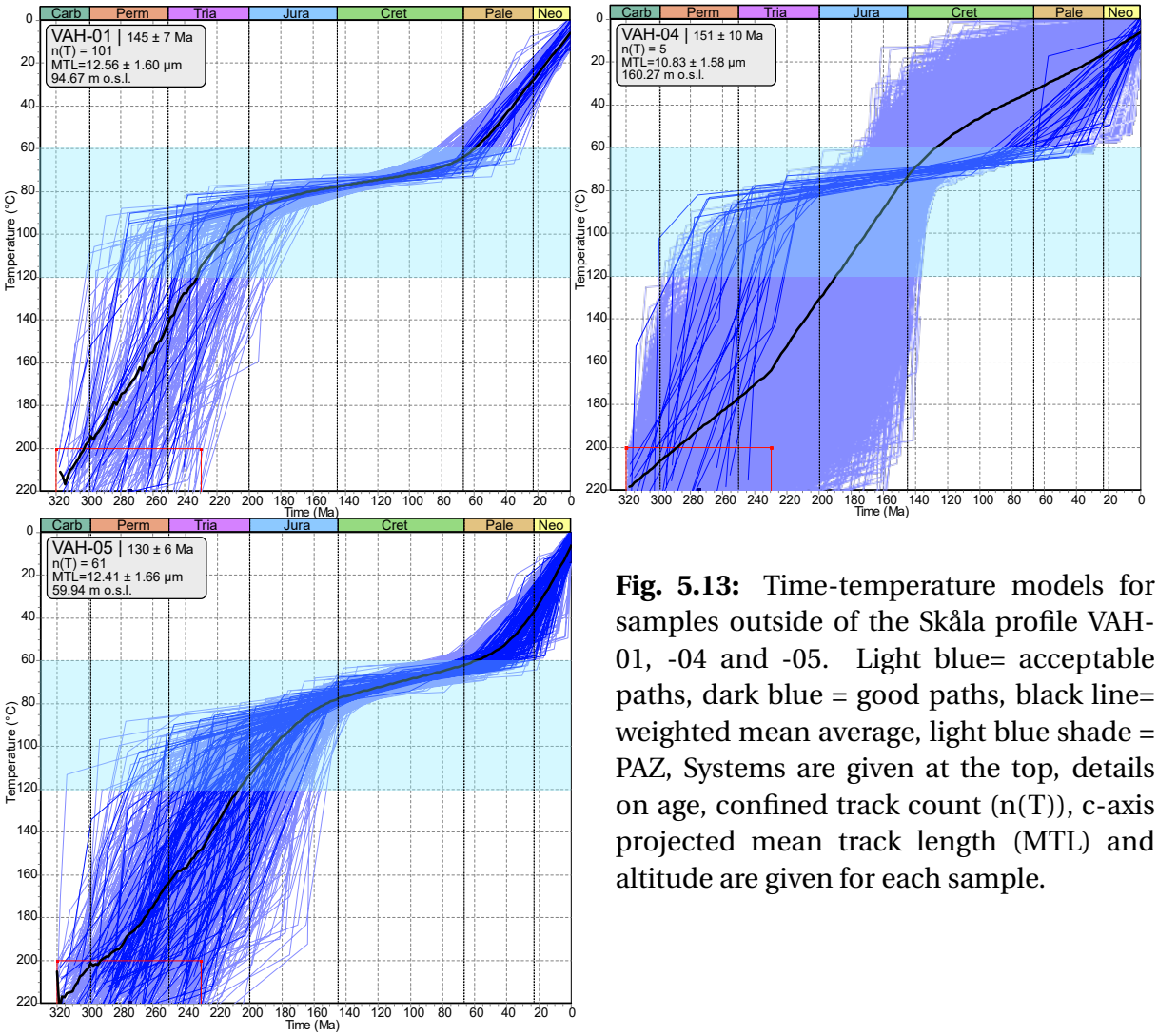

Fig. 5.13: Time-temperature models for samples outside of the Skåla profile VAH-01, -04 and -05. Light blue= acceptable paths, dark blue = good paths, black line= weighted mean average, light blue shade = PAZ, Systems are given at the top, details on age, confined track count (n(T)), c-axis projected mean track length (MTL) and altitude are given for each sample.

skews the weighted mean average, however, following just the 'good' paths, a similar trend as in VAH-01 and -05 can be seen. VAH-02 even though having over 100 tracks measured resulted only in 0 to 3 acceptable paths (when running the model several times). VAH-03 with only two tracks was poorly constrained and showed no clear result.

5.5.2 Skåla profile samples

From 14 samples from the Skåla profile all, except VAH-10 and VAH-14, showed clear modelling result. These samples showed similar time-temperature paths, a selection is presented here (Fig . 5.14). VAH-06 shows no significant difference to the time-temperature path of VAH-05, which might be due to their close proximation (Fig. 5.14). However, VAH-06 enters the PAZ slightly earlier, about 20 Myr, though leaves the PAZ somewhat synchronous.

VAH-11 follows the same principle of cooling (Fig. 5.14). During the Triassic, the sample enters the PAZ and cools rapidly ~1.0 °C/Myr. With the beginning of the Jurassic, the cool-

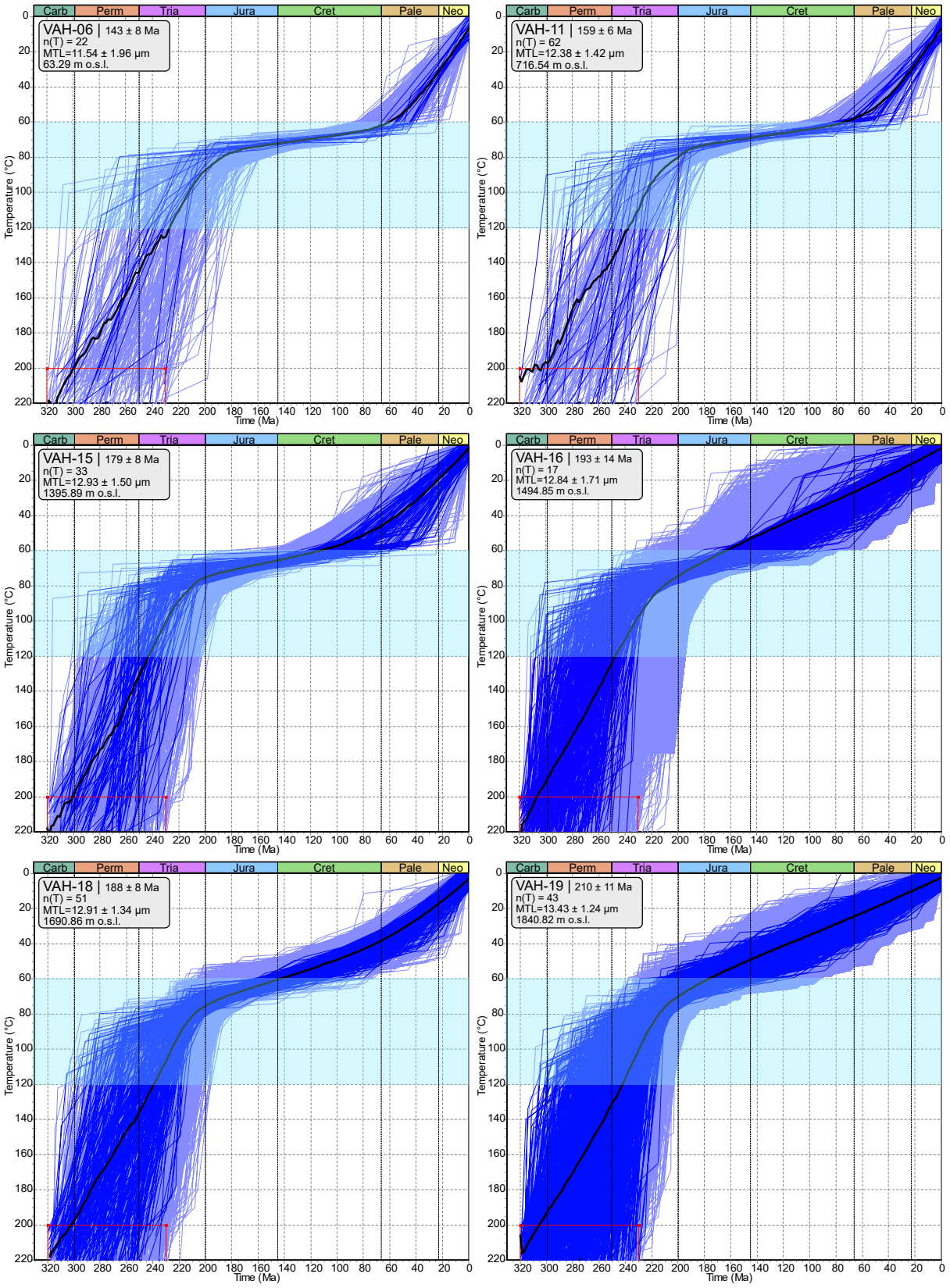

Fig. 5.14: Time-temperature models for samples of the Skåla profile VAH-06, -11, -15, -16, -18 and -19. Light blue= acceptable paths, dark blue = good paths, black line= weighted mean average, blue shade = PAZ, Systems are given at the top, details on age, confined track count (n(T)), c-axis projected mean track length (MTL) and altitude are given for each sample.

ing rate decreases to ~0.2 °C/Myr. Once the sample cools below the PAZ at the beginning of the Cenozoic, cooling increases again to ~0.8 °C/Myr. However, unlike the samples at lower altitude (e.g. VAH-06) the change from slow to faster cooling is less distinct and rather transitional (Fig. 5.15). A similar trend is followed by most samples in the lower section of the profile (Fig. 5.14 VAH-06 until VAH-14). First, rapid Triassic cooling into the PAZ, from the Jurassic onwards slow cooling and renewed cooling with the beginning of the Cenozoic. VAH-15 also starts with rapid cooling (~1.2 °C/Myr) until the Triassic-Jurassic boundary, following slow cooling (Fig. 5.14). However, VAH-15 does accelerated cooling at the end of the Mesozoic, but instead cooling rates steadily increase until present day. The sample enters the PAZ about 240 Ma and cools below the PAZ earlier than lower samples (Middle Cretaceous). VAH-16 shows rapid cooling (~1.3 °C/Myr) until ~220 Ma (Upper Triassic) (Fig. 5.14). The sample cools around ~250 Ma into the PAZ. In the Upper Triassic the cooling slows down, however, unlike VAH-15, VAH-16 keeps a steady cooling rate of ~0.4 °C/Ma until today. The disappearance of a sudden break in cooling with the end of the Mesozoic is also evident in the other samples of higher altitudes. Only VAH-18 show signs of a steady increase in cooling rate (Fig. 5.14), though less pronounced as in VAH-15. The highest sample VAH-19 also shows only two sets of cooling rates (Fig. 5.14). Rapid cooling until the Jurassic (~1.3 °C/Myr), and slower but constant cooling (~0.4 °C/Myr) onwards. VAH-19 enters the PAZ around 240 Ma and cools through it quickly in ~65 Myr (179 Ma).

5.5.3 Comparision of thermal models

The modelling results were compacted and simplified to allow for better comparison by using their weighted mean averages (WMA) (Fig. 5.15). Comparing the WMA allows us to get a general picture of the time-temperature-path of each sample, as the WMA represents all modelled paths while giving the 'good' path more weight. Almost all samples experience rapid cooling until the Upper Triassic (1.2 °C/Myr) (Fig. 5.15). The lowest sample VAH-05 however, cools slower initially and stops this phase in the Upper Jurassic. Every sample though shows a quite sudden change in cooling rates (Fig. 5.15 right). Interestingly, once the initial cooling phase is finalized, a slower cooling commences.The rate and style of this cooling varies dramatically between samples (Fig. 5.15 left). Generally, lower samples plateau during the Mesozoic and start sudden rapid cooling with the onset of the Cenozoic. With higher elevation, this sudden break seems to smooth out, until the highest sample retains a virtually linear cooling until present-day. This trend may not be linked entirely to elevation though, since the second highest sample VAH-18 shows a less linear cooling than VAH-16, ~200 m lower (Fig. 5.15 left). No sample shows signs of reheating with the applied constraints.

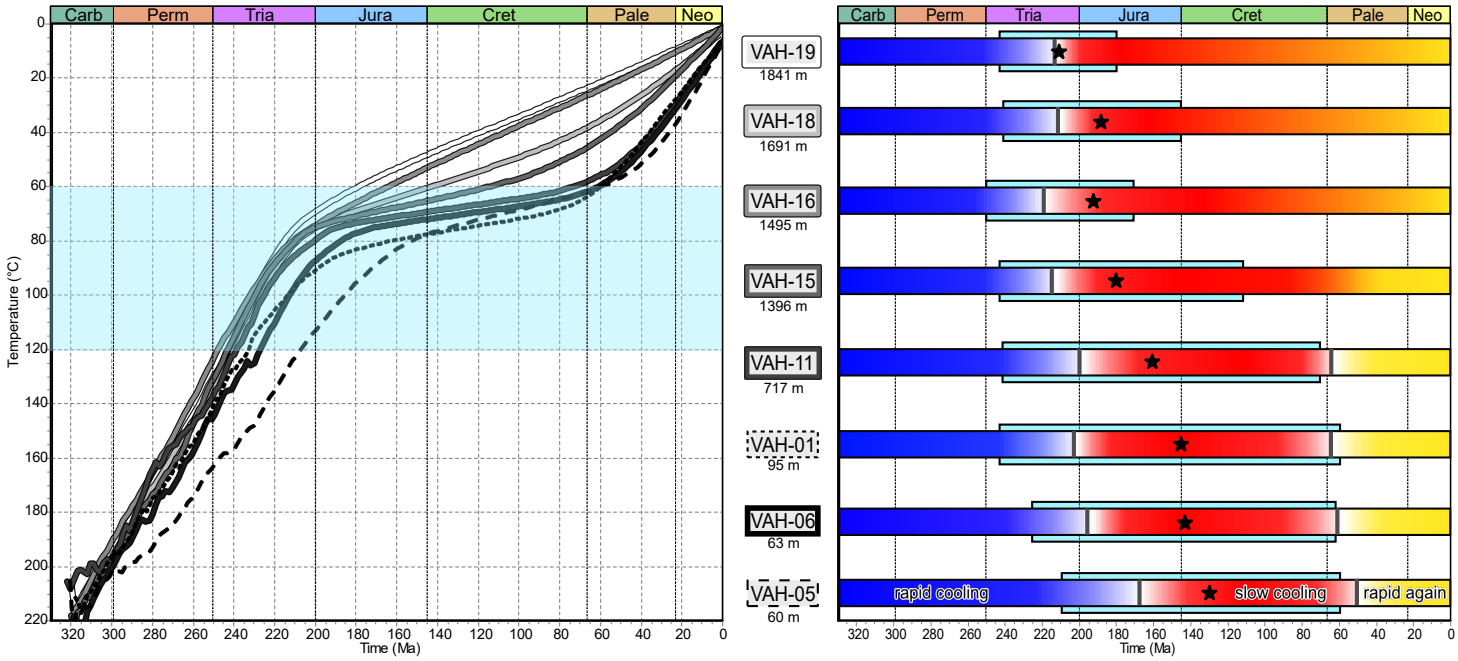

Fig. 5.15: Comparison of modelling results from samples VAH-05,-06 etc.... Symbology is indicated in the centre. The outline of each sample name indicates the respective symbology as used on the right-hand side. Elevation for each sample is given below sample name (in m a.s.l.). Left: Weighted mean averages (WMA) of different samples plotted in one time-temperature-plot. Periods indicated on top. Blue shaded area = PAZ. Dashed WMA indicate sample outside of Skåla profile. Right: Simplified cooling rates. Blue = initial rapid cooling, Red = slow cooling, Yellow = rejuvenated cooling. The dark border line indicates a sudden change in cooling rate while a smooth colour transition indicates slowly increasing cooling rates. The blue box in the back indicates the time frame in which the sample is within the PAZ. Black stars show AFT age.

Chapter 6

Discussion

Results presented in Chapter 5 comprise remote sensing of structural lineaments, 19 AFT samples as well as their respective thermal models. First, the data quality and interpretation will be discussed. Secondly, the results will be set in a regional setting and discussed in light of previous published work. Last, a sound interpretation of the thermal development of the study area will be inferred.

6.1 Assessment of data quality

6.1.1 Age data and grain quality

Important for evaluation the AFT data quality is the 1σ and the ρ_s. The 1 σ error of all ages remains below 10 %. Samples with low ρ_s tend to have larger errors, as counted tracks are limited. Notably, VAH-10 has the highest error (8.9 %) but also shows the smallest number of spontaneous tracks, as well as the lowest ρ_s and uranium concentrations. VAH-13 also shows a high error, even though ρ_s is not significantly lower. This sample is also the only sample failing the chi-square test ($\chi^2 > 5$ %), indicating more than one age population within the sample. In non-sedimentary rocks like monzonite, a failed chi-square test is rather unusual, but can be explained by varying chemical composition, poor alignment of the grain mount and the mica, inconsistent counting or simply contamination. As discussed in chapter 3, the Dpar value is a first approximation of chemical composition. However, the measured Dpar and its standard deviation for sample VAH-13 seems to be comparable to Dpars of other samples, suggesting similar annealing properties. Random recount of grains of this sample also confirmed previous measurements. If the alignment is poor, the track counting of the mount and mica does not match up and grains may be skewed to younger ages (if the objective aligns with an area of higher ρ_i than anticipated). However, the alignment of the

mount and mica of the samples did not show any significant deviations to justify a recount. Contaminations are also less likely to be the cause of this, as there is no particular outlier that may have caused the sample to fail the chi-square test. So, the sample needs to be taken at face value, though viewed critically. VAH-12 is the oldest sample, while not being at the highest elevation. However, VAH-12 also shows the highest Dpar values. While this sample has the highest Dpar, the MTL is quite low. No evidence would allow us to consider VAH-12 as an outliner. The likeliest source for false measurements is counting bias – biased, subconscious counting to fit the expected outcome. To avoid bias, samples were counted without previous interpretation or knowledge about their geographical location. Evaluations and age calculations were done after finishing counting all samples. With bias constantly in mind, I can report that measurements ought not to be affected by any kind of personal bias.

Each sample was evaluated and common features documented Table 5.2. The sample with the best quality was VAH-15. Undoubtedly, the sample with the poorest quality is VAH-16. Most grains appeared translucent to opaque. This implies a high amount of impurities blocking light from passing through the crystal. This made counting many apatite grains impossible. Only 12 countable grains were found. Beauty mistakes like fractures, dislocations, inclusions and zonation (Sec. 5.4.1) are not considered to be the cause for false measurements. Even though they can significantly complicate the counting process, I can exclude this as reason for poor data quality as I made particular efforts to avoid false counting for grains with such features.

6.1.2 Mean track length

Track length calibration showed that track length measurements tend to be slightly shorter (3%) than the average worker, which still allows for reasonable comparison with other fission track studies. In this study a mean MTL of 10.66 ± 1.01 µm was inferred, similar to other studies in southern Norway. MTLs were reported by Leighton (2007) (mean: 12.41 ± 0.65 µm), Johannessen et al. (2013) (mean: 11.08 ± 0.41 µm) and Ksienzyk et al. (2014) (mean: 12.21 ± 0.57 µm). Differences may occur due to regional variations, composition and c-axis projection (Sect. 3.1.1). Two samples contained more than 100 confined tracks. In samples with very few measured tracks this can lead to an under-sampling bias, where not the complete spectrum of the histogram is sampled, skewing the data to a certain length or misshaping the distribution. Samples with less than 10 tracks are virtually impossible to interpret, as no distribution will be visible. However, this is only in 4 samples the case. The low concentration of uranium results in fewer fission events, limiting the number of observable tracks. Hence, samples with low uranium concentrations also yield the fewest tracks. Longer tracks are usually more common to intersect with other tracks making them easier and more frequent

to spot than smaller tracks (Laslett et al., 1982). Even though the limited number of tracks overall, this issue seems not to produce a particular skew to longer tracks. VAH-12 shows rather short MTLs, while also having the largest Dpar. The Dpar, while mainly an indication for chemical composition (Sec. 4.2.4), can serve as an indication for annealing kinetics. A long Dpar generally means longer track lengths. VAH-12, however, shows both many long and short tracks producing the broadest distribution of all samples. This suggests that the sample must have spent more time in the PAZ and cooling slower than adjacent samples. But with only 30 measured tracks under-sampling cannot be excluded for VAH-12 and the distribution need to be interpreted with caution.

6.1.3 Thermal history models

Thermal history models are strongly influenced by the constraints we choose for our data. In this study, all constraints are therefore set based on the knowledge from previous studies (Sec. 4.3.1). An inverse model gives a first suggestion on the thermal history of a sample, but by no means the ultimate truth. For example without additional constraints, no reheating will be modelled by the software. When the model produces more good paths, is this an indication for an easy fit to the tested hypothesis. However, this may also require tighter and carefully chosen constraints to further resolve the thermal history. Besides the manually chosen constraint, the main input of a thermal model come from the age and the mean track lengths (see chapter 4.3 for more details). Sample with only a few measured tracks are poorly constrained and can display almost any path. Such models cannot be properly used for interpretation. Other samples may result in no or hardly any paths. VAH-02 and VAH-12, for example, produce none or only a few paths, despite having a solid number of tracks. When running the model until a good path is found it required more than 10 million tried paths, indicating that the given constraints are highly incompatible with any possible Tt-path (>180 mil. for VAH-12). VAH-03, -04, -10 and -14 on the other hand, produce a poorly constrained model and do not show clear cooling paths due to the limiting number of tracks.

Most models, however, show a distinct cooling path. Though due to varying track numbers a direct comparison between modelled samples is complicated. In these cases, the best estimate is the weighted mean average of a sample. Samples with successful modelling were used for further interpretation, even if the track number did not reach 100, as this is rather a recommendation than a hard rule (Chapter 3).

6.2 Partial annealing zone

The vertical profile taken at Skåla can contain information about apparent exhumation rate and possibly tectonic displacement (Fitzgerald and Malusà, 2018). When interpreting these data, we need to consider rather the isotherms than the topography. Isotherms are compressed below valleys and wider spaced below mountains. Isotherms are deflected by long wavelength topography and advection, so they may not exactly mirror topography (Gleadow et al., 2000; Fitzgerald and Malusà, 2018). In the study area, the wavelength of topography is (currently) short and exhumation rates are very low (see below). For the Skåla vertical profile, the horizontal distance is short (about 3.2 km). Therefore, the effects of advection and topography are negligible. In fact, for denudation rates lower than ~300 m/Myr advection is likely not to play a role (Brown and Summerfield, 1997) and the age-elevation profile of Skåla merely shows ~30 m/Myr. However, in cases where relief changes drastically with time, exhumation rates might be overestimated (Braun, 2002). As mentioned in chapter 2, sampling a vertical profile may or may not reveal an exhumed partial annealing zone (PAZ). However, the linear regression of the age-elevation profile along Skåla shows an ambiguous result with two possible premises: 1) a continuous age-elevation relationship, or 2) a change in exhumation rate at 1250 m altitude and displacement of ages. Both scenarios will be discussed in the following sections.

6.2.1 Continuous exhumation

Assuming the simple case of stable and continuous exhumation, this means that no PAZ was exhumed. This results in no change in exhumation rate at all and is shown in Fig. 6.1(left). Linear regression applied to the resulting age-elevation profile suggest a low exhumation rate of ~30.1 ± 6.3 m/Myr.

This scenario renders VAH-12 as an outlier. Inverse modelling of VAH-12 was not successful and did not result in any good path whatsoever, though this is not reason enough to disregard this sample altogether. The scenario of continuous exhumation suggests no major influence from rifting on exhumation rates, as cooling seems to be more or less stable. Lengthening of MTL without a change in exhumation rate seems contradicting (Fig. 6.1 right). Earlier work highlights the strong influence of offshore rift phases on onshore structures (e.g. Ksienzyk et al., 2014; Fossen et al., 2021). Therefore, considering earlier studies and evidence from the profile, a continuous exhumation during the entire Mesozoic seems unlikely. The exhumation rate in the age-elevation profile cannot be explained by one singular regression. So, this approach is with good confidence rejected.

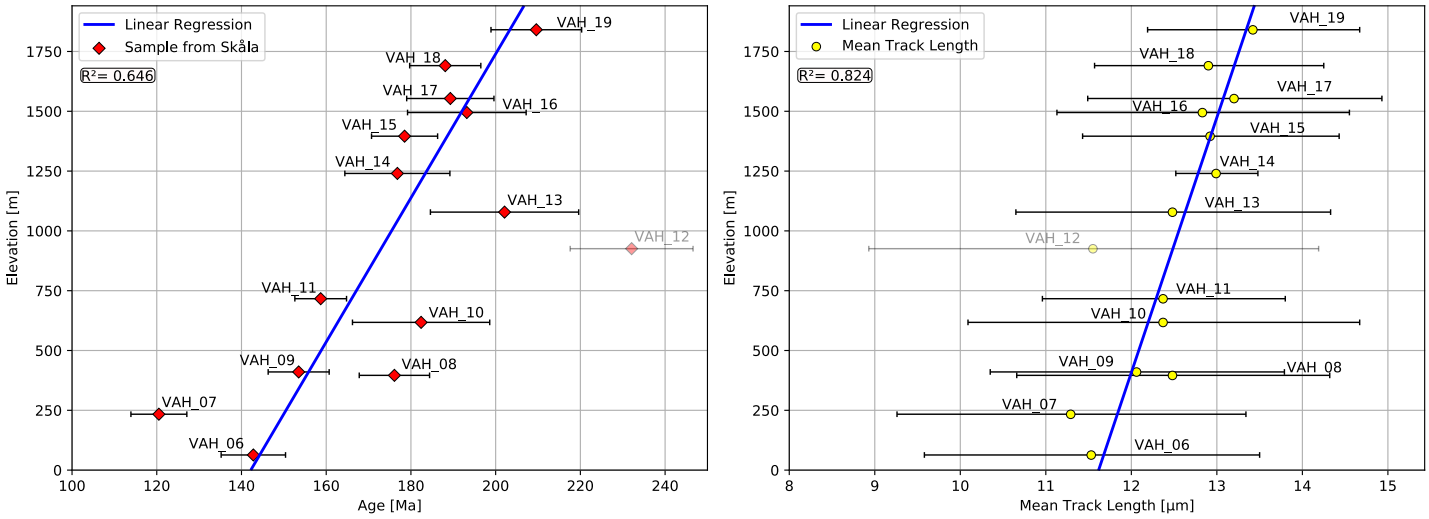

Fig. 6.1: Age-elevation profile (right) and respective MTL (left) for the Skåla profile if VAH-12 is considered an outlier. Errorbars indicate 1σ error. The blue line is given as linear regression

6.2.2 Break in slope and exhumed PAZ

By assuming a displacement between VAH-13 and VAH-14, two separate regression lines could be drawn to achieve a significantly better fit, however, that requires a fault separating both sample locations (Fig. 6.2). If a break is present in the age profile, a similar break should be visible in the MTL against elevation as well.

The resulting offset at around 1250 m altitude is about 50 Myr (Fig. 6.2). A similar break can also be observed in the MTL. A shift to longer MTLs (~0.40 µm) also fits well with the observation in the age profile, since you would expect longer confined tracks with more rapid exhumation, as is the case in the upper section of the profile.

6.2.2.1 Exhumed PAZ in the age-elevation profile

The age-elevation profile in figure 6.2 does not show the typical signature of an exhumed paleo-PAZ (Sec. 3.2.3). This may be due to either the lack of major difference in cooling rates between stages of tectonic stability and cooling, or no longer phases of tectonic activity causing displacement along the profile that might obstruct an ascended PAZ (Fitzgerald and Malusà, 2018). The two constructed slopes may represent the upper section of an exhumed PAZ (Fig. 3.8). The base of the PAZ is not sampled and hence not displayed in the age-elevation profile. MTL distributions also show an increase in length and smaller distribution towards higher samples, as expected from the upper section of a PAZ (Sec. 3.2.3, Fig. 3.8).

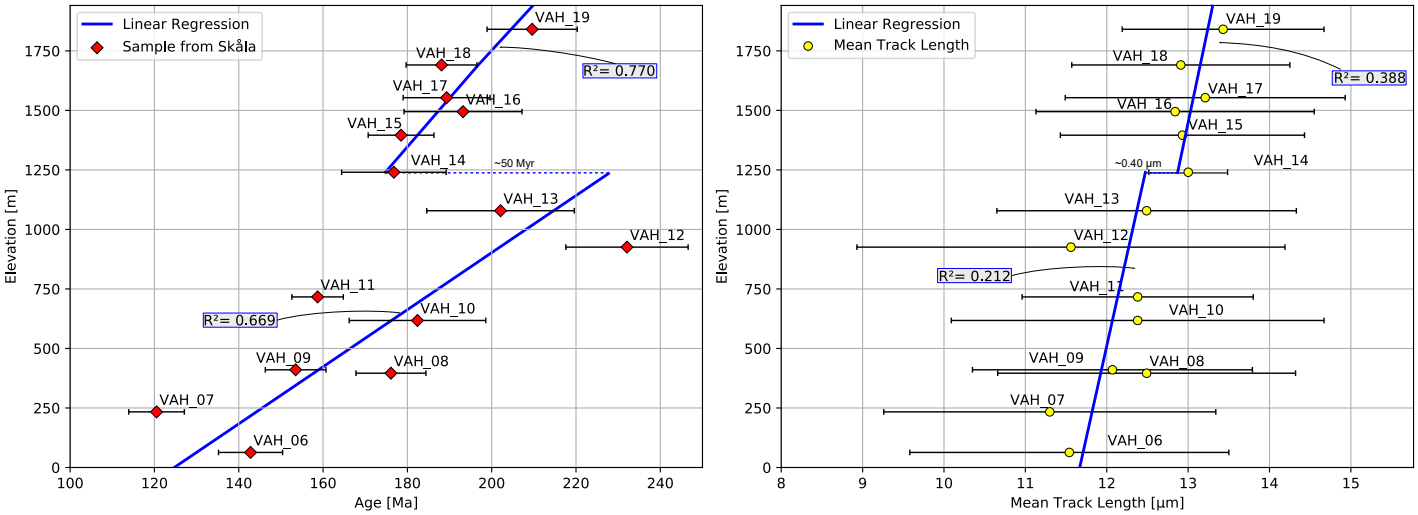

Fig. 6.2: Age and MTL profile with break between VAH-13 and -14 to achieve a better fit. Regression lines in blue with 1σ errorbar. Left: Linear regression for age against elevation. Lower regression from VAH-06 to (incl.) VAH-13. Upper regression from (incl.) VAH-14 to VAH-19, the dashed line indicates age offset (~50 Myr). Right: Linear regression for MTL against elevation. Lower regression from VAH-06 to (incl.) VAH-13. Upper regression from (incl.) VAH-14 to VAH-19, the dashed line indicates age offset (~0.40 µm).

An exhumed PAZ usually shows a strictly increasing age with elevation (e.g. Fitzgerald et al., 1995; Fitzgerald and Malusà, 2018). Exceptions can be where the vertical profile is cut by tectonic displacement and there is a shift to younger ages (e.g. Miller et al., 2010). In the Skåla profile we observe an abrupt shift in the central parts of the profile rather than a gradual change of ages (Fig. 6.3).

Assuming that the age-elevation profile represents the upper section of an exhumed PAZ, we can estimate the apparent exhumation rate of 20.5 ± 5.4 m/Myr for a former cooling event, considering previously mentioned caveats to exhumation rate estimation. Given the inferred ages, Early Jurassic North Sea rifting may have served as a trigger for more rapid cooling. Close-by illite fault gauge dating reveals similar reactivation ages and are as well linked to the second rift phase (Fossen et al., 2021). Slower cooling commences during the Late Jurassic, as fault activity decreases as well (Fossen et al., 2021). The slope of the two regressions is so similar, that they show overlapping 1σ confidence and one could argue that continuous cooling took place in addition to the displacement between VAH-13 and VAH-14.

6.2.2.2 Evidences for a hypothetical fault

The transition in the age-elevation profile (Fig. 6.3) is marked by an offset of ~50 Myr or a vertical offset of roughly 625 m (see dashed blue line in Fig. 6.3). This offset may have been

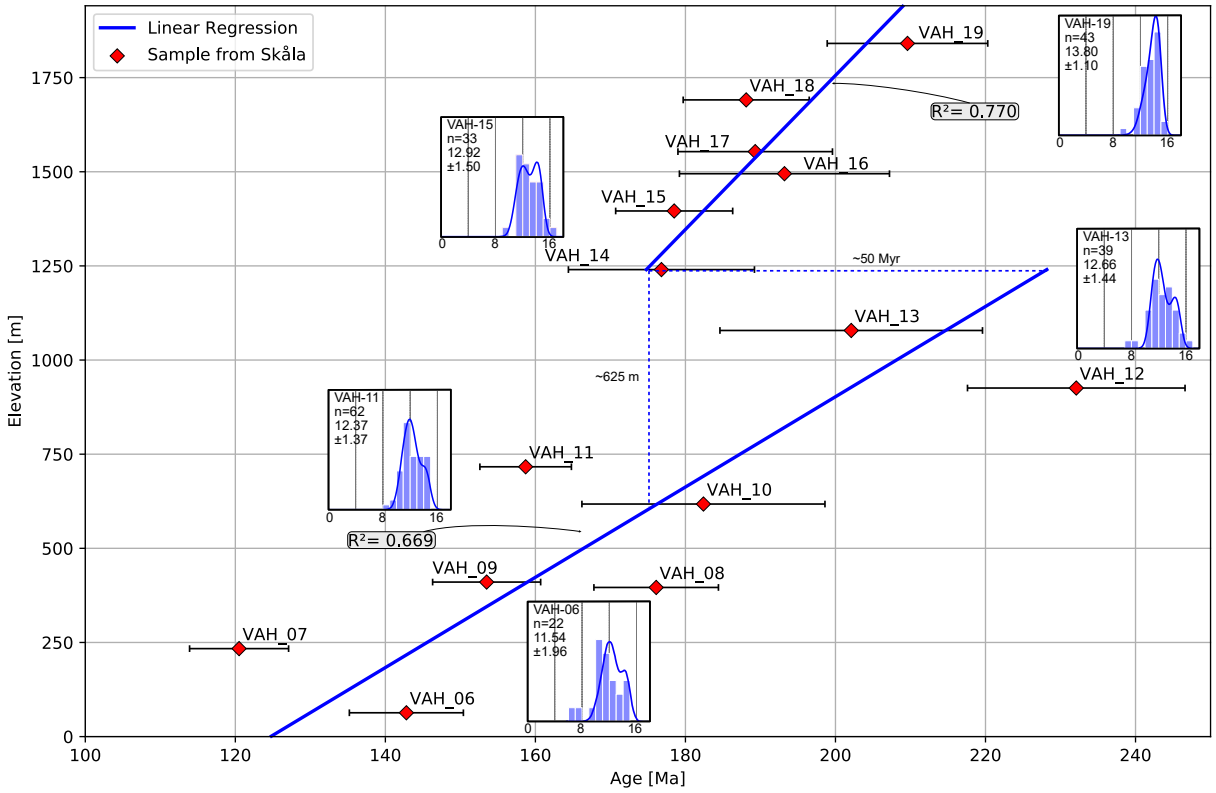

Fig. 6.3: Age-elevation profile with separated linear regression between sample VAH-13 and -14 showing a ~50 Myr gap or an offset of ~625 m to the lower regression line. The gap is shown as a dashed line. Track length distribution, MTL in µm, 1σ error and number of measured tracks is given for some samples.

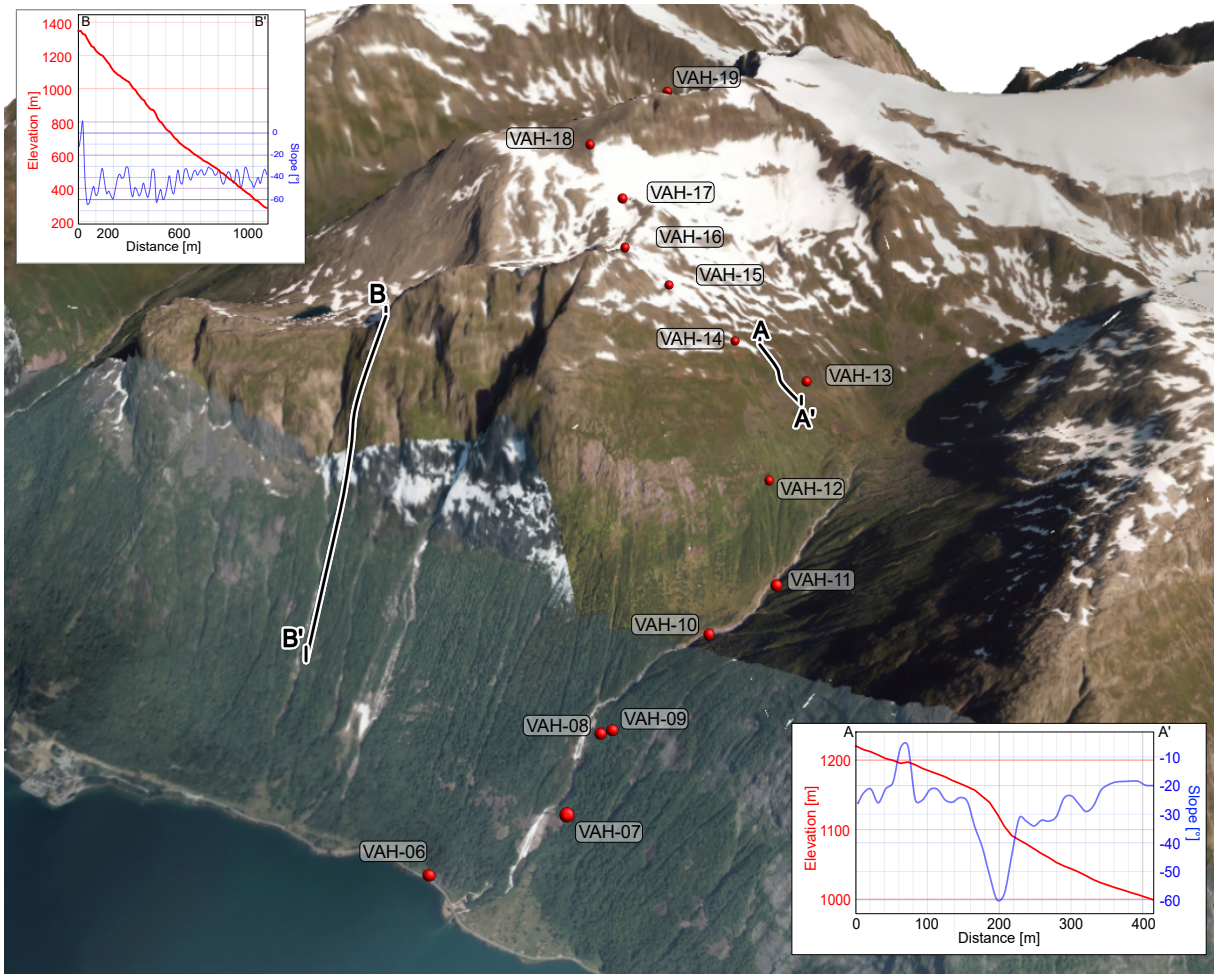

Fig. 6.4: 3D image of the Skåla profile. Red symbols show sample locations. Two profiles were drawn along the cliff-side, with their respective elevation and corresponding slope. Subplots in the corners show each profile with elevation (red) and slope in degree (blue). Orthophoto by Norgeskart.no; DEM by Kartverket.no

caused by a fault. An offset in MTL of ~0.4 µm, with longer tracks in the upper section of the profile, indicates more rapid cooling in the footwall. However, while sampling, no fault was observed. In fact, Skåla was chosen because of fewer apparent lineaments along the slopes (personal comment Åse Hestnes, Prof. Joachim Jacobs). Nonetheless, a fault cannot defiantly be ruled out as it may have been concealed by debris or vegetation.

Also 3D images do not clearly uncover faults (Fig. 6.4). But slope measurements between the two samples in question reveal a section with a conspicuous 60° slope, suggesting an actual fault may be present. This fault likely strikes parallel to the side valley (~E-W). However, to undoubtedly verify this, field observations are required. Remote sensing does not provide solid information about fault displacement, as significant sections of the fault zone are likely concealed. Additional slope measurements were conducted along valley facing slope, showing a similar angle, suggesting fault influence during valley formation.

Figure 6.5 visualizes the estimated offset, due to normal faulting between VAH-13 and -14

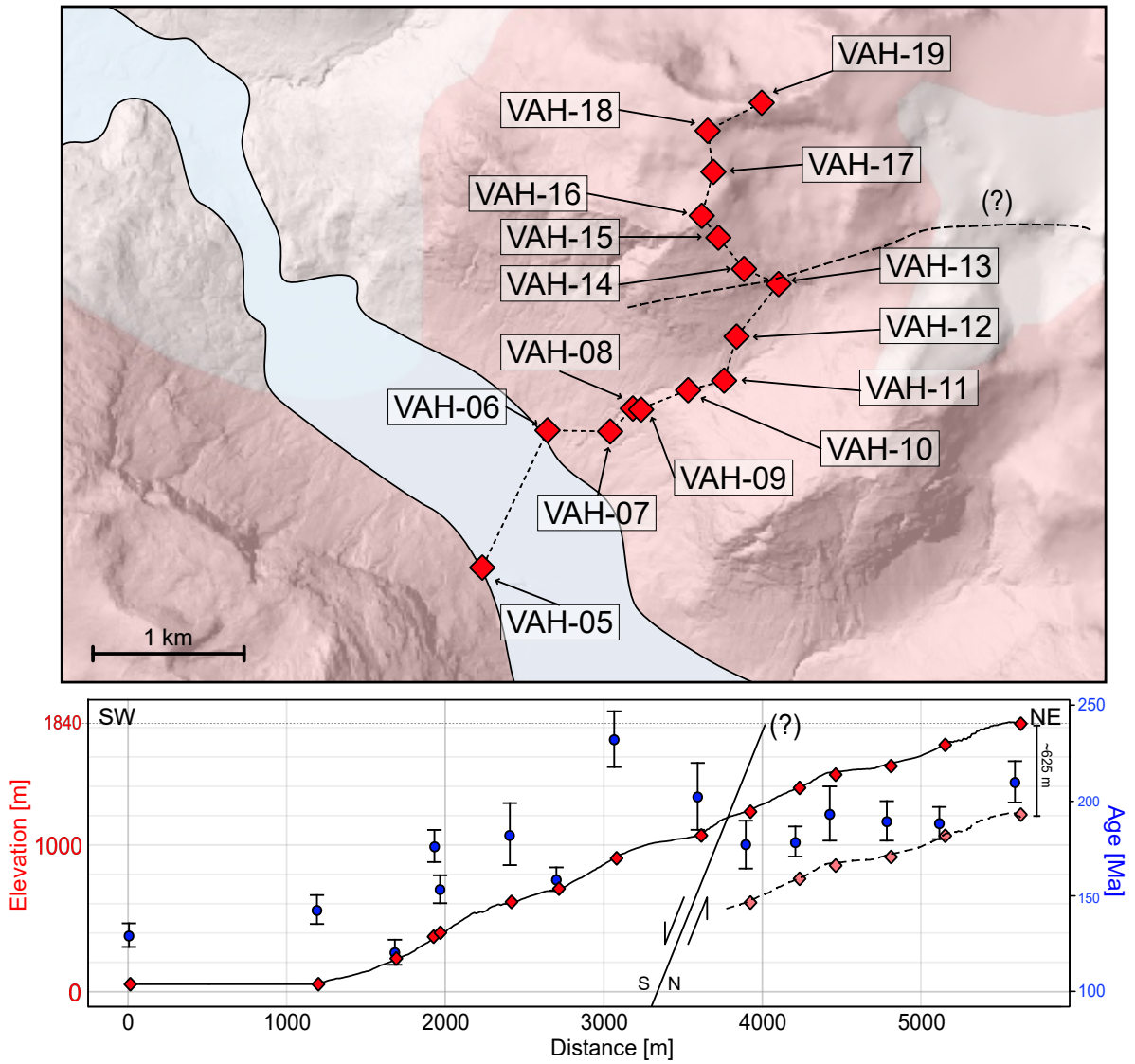

Fig. 6.5: Modified Fig. 5.11 with interpreted fault. The black dashed line shows a possible fault trace. Below: Profile with respective ages, showing sample location pre-faulting (faded red) with ~625 m displacement. Errorbars indicate 1σ error.

and also shows an ~625 m displacement. As the ages are displaced themselves, the ages must have been acquired before faulting took place. Given that the measured ages represent the pre-faulting position, the age of the fault must postdate the cooling past the T_c, i.e. Middle Jurassic. This coincides well with the 2nd rift phase (e.g. Færseth, 1996; Ksienzyk et al., 2016). Combined data shows that faulting was most active during both rift phases but did not completely cease until the Paleogene (Fossen et al., 2021). The exhumed PAZ does not show increased Cenozoic cooling as it is not exhumed far enough. Low-temperature thermochronological methods than apatite fission track, like apatite (U-Th)/He may reveal other parts of the PAZ and are a highly valuable tool for further interpretation. Inverse models also give further insights into the thermal evolution and will be discussed in the following section.

6.3 Interpretation of age and inverse models

The inverse models give a valuable view into a possible time-temperature path (Tt-path). It allows to track the temperature of each sample through time. The measured age for each sample matches (for successful models) always with ~72 °C. The path also gives a distinct signature (Fig. 5.15). It shows that the samples had a similar temperature during the Late Triassic. Subsequently, the temperature difference between each sample increases, until it reaches its maximum at the Upper Cretaceous to Cenozoic boundary. The Tt-path is highly dependent on the spatial distribution of isotherms. This can be influenced by:

- change in geothermal gradient (e.g. by advection)
- change of topography i.e. change Δz (e.g. by differential erosion, faulting)
- a combination of both

This differential change in temperature also spans over almost the whole Mesozoic, so a long-term process is likely the mechanism. Other thermal processes that could reset the measured age, like wildfires (Wolf et al., 1998) or fault friction (Tagami, 2012) are unlikely. The different possibilities are discussed in this section.

6.3.1 Thermal variation (Geothermal Gradient)

Heat flow studies and estimations of geothermal gradients in Western Norway are quite uniform and suggest a low (modern) geothermal gradient of about <20 °C/km for the study area (Pascal et al., 2010; Maystrenko et al., 2021; Leighton, 2007). Extensive drilling in the North

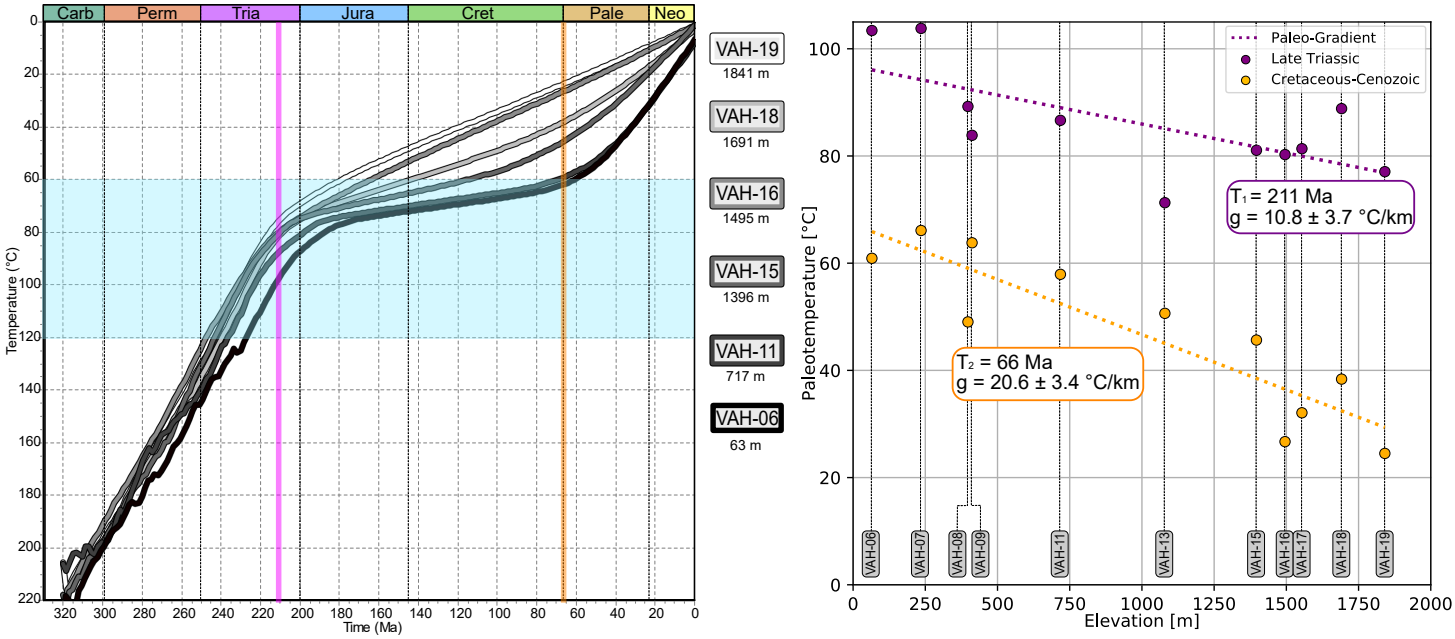

Fig. 6.6: Reconstruction of the Paleo-Geothermal Gradient. Right: Inverse models of the Skåla samples with time-markers at which the geothermal gradient was inferred. Blue area = PAZ. Left: Diagram showing paleotemperature (°C) over elevation (m). Regression is used to infer the paleo-geothermal gradient.

Sea allowed for higher resolution thermal data, showing a high gradient on the Norwegian Shelf that quickly drops below 20 °C/km when approaching mainland Norway (Harper, 1971; Evans and Coleman, 1974). Recent borehole studies in Norway show a stable 16 – 20 °C/km geothermal gradient in the upper 300 to 800 m (Maystrenko et al., 2021). Boreholes from Stavanger however, show also geothermal gradients of just ~13 °C/km (Maystrenko et al., 2015). Changes in the thermal structure of the upper crust may be related to exhumation (Braun, 2016). Examples in the European Alps show that rapid erosion can cause advection to influence cooling paths to match the resulting cooling signature of this study (Zanchetta et al., 2015). However, advection as a result of erosion acts in orders of a few million years, unlike the mechanism at play here that shows long-term effects.

By plotting the maximum paleotemperature at a given time over its modern elevation we can estimate the paleo-geothermal gradient by plotting a regression through the data points (Fig. 6.6 right, e.g. Ventura and Lisker, 2003). The paleotemperature was inferred by taking the mean temperature of all generated paths at a time T (python code from Sirevaag et al., in review). By doing this for the Late Triassic (T_1: 211 Ma) and the Cretaceous – Cenozoic boundary (T_2: 66 Ma), two paleo-geothermal gradients can be inferred with 1σ confidence. The timesteps were chosen as they not only show a change in cooling rate, but also represent times where the difference in temperature was small (T_1) and large (T_2). If we assume the variation in temperature spacing to be the result of a change in geothermal gradient only, requires this a reduced geothermal gradient of 10.8 ± 3.7 °C/km in the Late Triassic to accus-

tom the observations. Subsequently, the geothermal gradient needs to increase to (modern) 20.6 ± 3.4 °C/km until the late Cretaceous (Fig. 6.6). A change in geothermal gradient is not unreasonable. Different mechanisms can affect the heat flow in the upper crust. An insulating sedimentary cover with a low thermal conductivity could increase the geothermal gradient in the crystalline basement below (Łuszczak et al., 2017; Kim et al., 2020). However, the estimated modern geothermal gradient is higher than the low geothermal gradient estimated for the Late Triassic, without the presence of a sediment cover. An increased heat flow could be a response to ascension of the thermal lithosphere-asthenosphere boundary, e.g. by crustal thinning, mantle upwelling or increased magmatism and may even be related to rifting (Gholamrezaie et al., 2018; Malusà and Fitzgerald, 2019b; Kim et al., 2020; Li et al., 2019). Well established rift phases in the North Atlantic during the Mesozoic (e.g. Færseth, 1996; Doré et al., 1999; Fossen et al., 2021) may have caused enough crustal thinning to elevate the heat flow along the passive margin . Mantle upwelling, triggering dynamic topography (Pedersen et al., 2016), may increase the local heat flow as well, however, these effects only account for more recent thermal evolution and show only a limited effect in southwestern Norway (Schiffer and Nielsen, 2016). Considering the low Permo-Triassic geothermal gradient inferred by this approach, which is more typical for subduction zones than for passive continental margins (Dumitru, 1991), it is deemed unlikely that a change in thermal structure is the reason for the observed signature.

6.3.2 Topographic variation (Displacement and erosion)

If we assume a stable geothermal gradient, the vertical distance of the samples must have changed to explain the inverse model. Having most samples at a similar temperature requires them to be buried at a similar depth. Assuming a modern gradient of 20 °C/km, the samples would still have been buried ~3.6 – 5.1 km below the surface, resulting in a height of the Skåla profile of roughly ~300 m lower than at present-day (Fig. 6.7). Though showing low variation in elevation for samples VAH-08 to -19 and a significant jump in burial depth to the much deeper samples of VAH-06 and -07. With the end of the Mesozoic (T_2), the steep nature of the Skåla profile becomes obvious, even in its thermal signature (Fig. 6.7).

The transition from shallow slope in the late Triassic to a steep thermal profile at the end of the Mesozoic (Fig. 6.7) could theoretically be explained by (1) tectonically tilting (e.g. folding, doming, flexural uplift or otherwise), (2) by erosion of initially high relief topography to a low relief surface or (3) normal faulting, which increases the vertical distance. Tilting (1) would require the tectonic blocks eastern flank of Skåla to tilt upwards to move (now) upper samples higher. Folding and doming are difficult to constrain but have been documented from the area (e.g. Young et al., 2011; Hacker et al., 2010). Flexural uplift, considering an

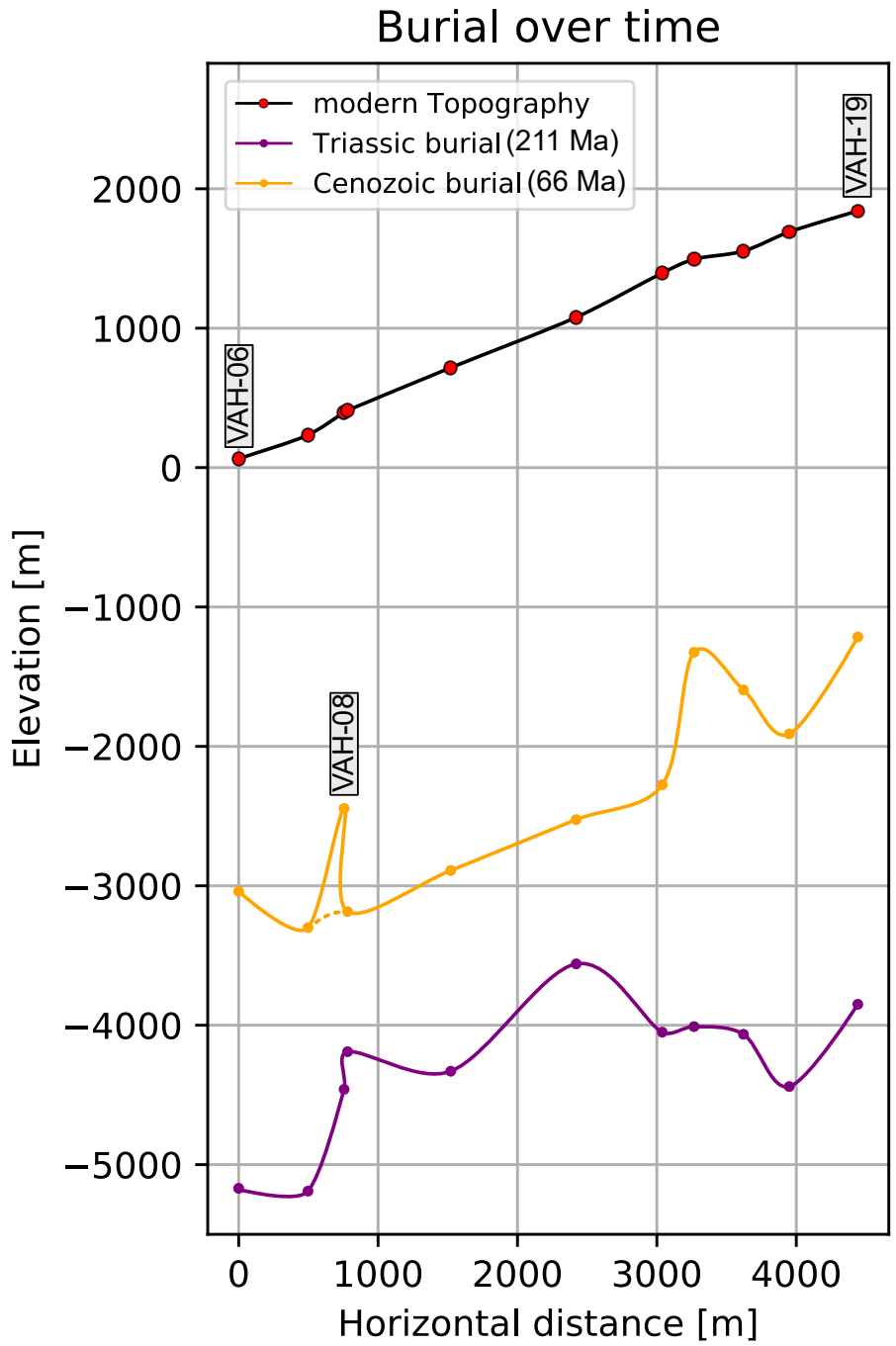

Fig. 6.7: Estimated burial for Late Triassic (211 Ma, purple) and Mesozoic-Cenozoic boundary (66 Ma, orange) based on temperatures from inverse models (Fig. 6.6) and average modern geothermal gradient of 20 °C/km. Modern topography is given as black line along the Skåla profile. Markers show position of samples. Dashed line shows burial if VAH-08 is not regarded.

eastwards extension during the rift phases, seems counterintuitive, since that would mean that the western flank would be uplifted. An extensional top-to-the-east Geiranger shear zone (GSZ, Fig. 2.1, Wiest et al., 2021) would have the right sense of direction. However, all these processes were active syn- or post-Caledonian, before the thermal tilting took place as shown in the inverse models. A change in topography (2) appears to be a more reasonable and simpler explanation. Assuming a high relief topography during the Late Triassic, that roughly follows the slope of the profile, all samples will acquire a similar temperature. By the end of the Cretaceous, the topography was then reduced to a low relief surface. Such interpretation is not unique, as similar conclusions were drawn by many researchers that support the paleic surfaces theory (e.g. Gabrielsen et al., 2010; Sømme et al., 2013; Rohrman et al., 1995). Even high relief topography during the Late Triassic is a commonly accepted interpretation (e.g. Leighton, 2007; Nielsen et al., 2009; Gabrielsen et al., 2010; Sømme et al., 2013; Ksienzyk et al., 2014; Pedersen et al., 2016). Though the influence the topography has on the perturbation on isotherms in 4-5 km depth needs to be considered. The main factor is the amplitude and wavelength of topography. With a wavelength of less than 12.5 km, the 100 °C isotherm remains unaffected (Braun, 2002; Reiners and Brandon, 2006). Therefore, the paleo-topography is required to have had significant relief and wavelength. Faulting (3) has most likely affected the area during the first and second rift phase and may have resulted in the vertical offset of samples. Faulting within the fjord may have caused displacement, enhancing cooling of lower samples like VAH-06 and -07. Additional E-W striking faults may have initiated exhumation of VAH-12 and -13 already in the first rift phase (Permo-Triassic), explaining old ages, but reactivation during the Jurassic rift phase may have cause vertical displacement, notably between VAH-13 and VAH-15. By the end of the Cretaceous, the vertical position of the samples is reached and only valley erosion and erosion at higher elevations take place from an already low relief surface.

6.3.3 Estimated exhumation through time

Once we conclude the more likely cause for the Tt-path we can estimate exhumation rates for each cooling phase (Fig. 5.15) and correlate these to independently described geological events. Thermochronology only constrains cooling, which is usually linked to exhumation or denudation - not surface uplift. It is therefore impossible to infer the altitude of the paleo topography without any independent data. Most likely the temperature variation is not due to a change in heat flow. A 10 °C/km geothermal gradient is quite low and usually expected within active subduction zones (e.g. Dumitru, 1991). Boreholes close to Stavanger with comparable low gradients were drilled in phyllite and showed a lack of heat-producing elements, compared to other boreholes (Maystrenko et al., 2015). Samples VAH-15 to -19 would show

a different geothermal gradient then samples VAH-06 to -13. With the latter one inferring a gradient more similar to a modern gradient of 20 °C/km. A more likely trigger for differential cooling is the vertical displacement of samples and likely also changes in topographic relief during exhumation. Miller et al. (2010) conclude that isochronic displacement along their vertical profile on Mount Munson is likely caused by a step-faulted architecture of the Transantarctic mountain range. They also observed similar Tt-paths for their profile, however, they suspect it simply to be a misleading signature of inverse modelling. Arguably, the resolution of thermal models for the AFT system below 60 °C is lacking, and modelling of AHe data could draw a clearer picture for this temperature range. This study suggests changes in topographic relief and warping of isotherms to have influenced Tt-paths (Fig. 6.8). During the Late Triassic, samples of the Skåla profile show roughly similar temperatures (~80 °C, therefore we suggest high topography (Fig. 6.8a) that subsequently experiences fault reactivation during the 2nd rift phase in the Jurassic (Fig. 6.8b). Displacement of ~625 m due to faulting results in the visible offset of ages in the age-elevation profile and faster exhumation of upper samples in the inverse models. Tilting of samples by tectonic instability can be considered, but initial high topography is seen to be more likely. By the Late Cretaceous, former topographic relief had been removed (Fig. 6.8c). Its absolute elevation cannot be inferred from thermal models, but its low relief nature seems evident, given that the present slope of the samples was already established. Certainly, there is room for interpretation, e.g. post-Mesozoic movement, the degree of flatness of Late Mesozoic surfaces or thermal evolution that may be concealed by different caveats of thermochronological interpretation. However, considering the obtained data of this study – the simple and more straight forwards solution would suggest peneplanation by the end of the Cretaceous.

The Cenozoic thermal response can be explained by differential erosion and valley carving. This may have been enhanced by rejuvenated continental margin uplift, causing fluvial or glacial fluvial erosion (Lidmar-Bergström et al., 2000) or differential periglacial erosion in combination with isostatic rebound (Egholm et al., 2017). In any case, valley incision likely commenced during the Cenozoic shaping isotherms to reflect the changing relief (e.g. Schildgen and van der Beek, 2019) eventually resulting in the present-day valley, as evident from the location of the samples (Fig. 6.8d). To test if the isothermal warping is spatially sound with the topography of this scale, I set up a simple model employing the heat equation (Stüwe, 2007) for the Late Triassic and Late Cretaceous case (Fig. 6.8 a and c). Thermal parameters were chosen from Maystrenko et al. (2015, 2021) and thermal boundaries to accommodate roughly a 20 °C/km geothermal gradient. The amplitudes of topography were set to 750 m in the Late Triassic (Gabrielsen et al., 2010; Sømme et al., 2013) and just 150 m in the Late Cretaceous. The wavelength in the Late Triassic was set at 6 km, though testing showed that there is a lot of leeway to still fit the interpretation. For larger wavelengths (>12

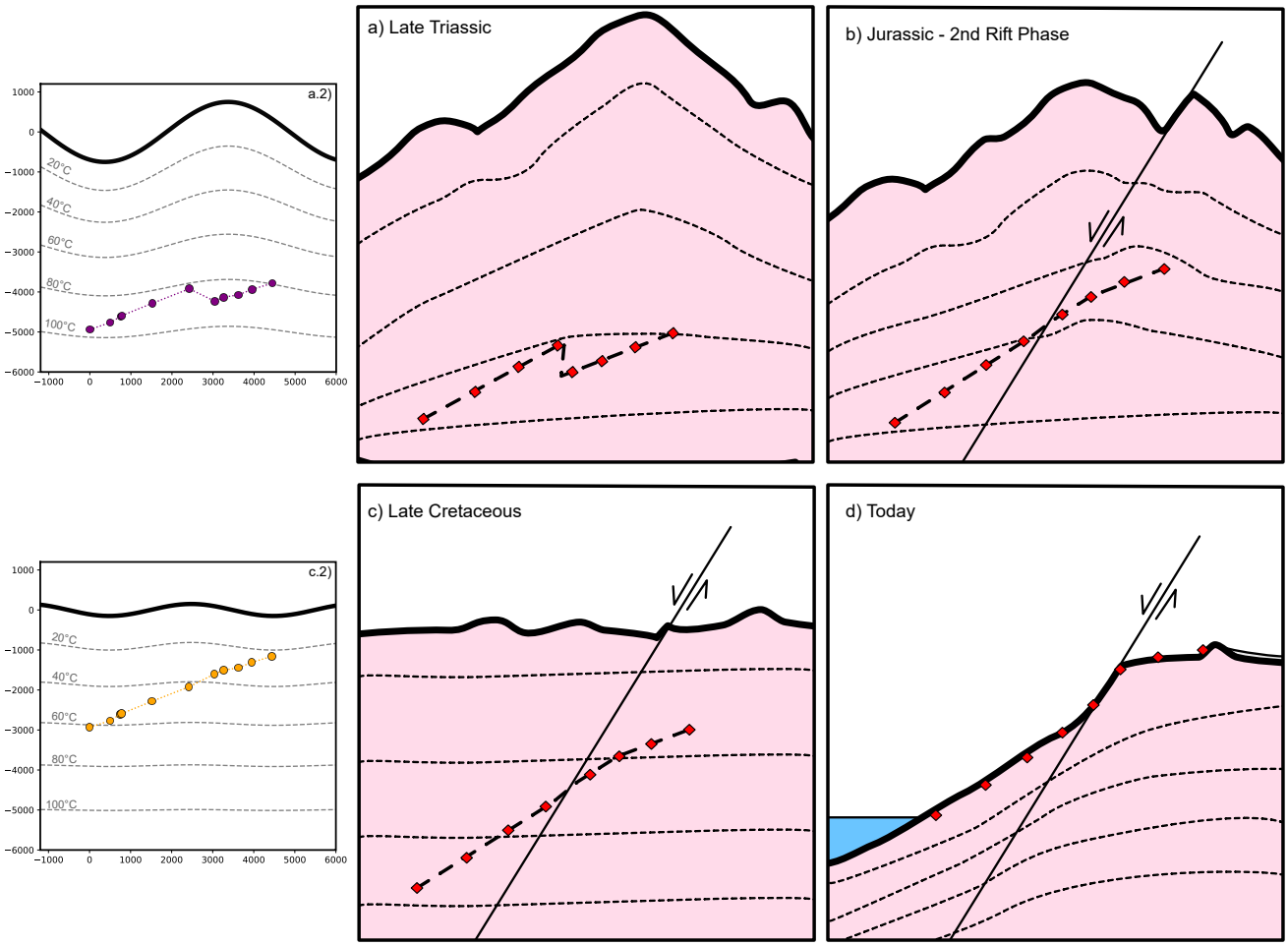

Fig. 6.8: Left: Numerical model of isotherms for the Late Triassic (a.2) and Late Cretaceous (c.2), solid black line = modelled topography and Temp=0°C, dashed line isotherms, dots show inferred sample burial based on estimated exhumation (more details in text). Right: Conceptual model of topographic evolution of Skåla profile (a- b). Dashed lines: estimated isotherms. Red diamonds: Samples and their relative location. The blue area shows modern fjord and sea level. The elevation is not to scale.

km), the location of the samples became relevant. The results (Fig. 6.8 a.2 and c.2) show that given a certain relief, scattering of temperature paths in time is a plausible result of landscape flattening and faulting. The python code is enclosed in Appendix C. The inverse models of samples outside of the profile are mostly inconclusive. VAH-01 and -05 show a delayed Triassic to Jurassic cooling phase, in comparison to samples from the Skåla profile. The inverse model of VAH-02 hardly resolves any path, however, when running the model for longer periods of time (>10 million paths) the model suggests an early entrance into the PAZ similar to VAH-09 (roughly the same elevation as well), but with a delayed cooling in the Cenozoic (55 Ma, Appendix B). Yet, a direct comparison of these models can lead to false interpretation, as they have different boundary conditions. Still, even under consideration of thermal models, both high topography and fault activity likely played a key role in the thermal evolution and the proposed topographic evolution stands. For the Skåla profile, we can estimate the amount of exhumation with a 20 °C/km geothermal gradient of about ~2 – 3 km Late Triassic to Late Cretaceous and about 1 km Cenozoic to today on higher elevations and up to 3 km within the valley. Assuming a combination of both a change in thermal state and tectonic displacement makes the actual exhumation virtually impossible to resolve but is not completely unreasonable.

6.4 Interpretation of structural observations

Recent K-Ar fault gouge data show that onshore faulting is highly influenced by the North Sea rifting (Fossen et al., 2021). A connection between onshore and offshore structures can likely be seen. In the following, the gathered information from remote sensing and lineament mapping will be compared with studies in the vicinity of Nordfjord, mainly offshore Måløy (Fig. 2.1, Reeve et al., 2015). The structural observations will also be compared with the inverse models and inferred AFT ages.

6.4.1 Major and minor lineaments

Gabrielsen et al. (2002, 2018) identify a dominantly NE-SW to NNE-SSW lineament in this structural belt (Mandal-Molde Zone), which is in contrast with the measured NW-SE lineaments of this study (Fig. 5.4). NE-SW lineaments are present in the study area but less common than NW-SE lineaments. NE-SW lineaments also show a large spread in directions, scattering form E-W to NNE-SSW lineaments in roughly equal quantity. Gabrielsen et al. (2018) inferred that the lineaments disappear beneath Caledonian Nappes, however in the inner Nordfjord, NW-SE lineaments are still affecting the Nappes. This might also contribute

to relatively more NW-SE to NNW-SSE mapped lineaments. The imminent influence of the Nordfjord Shear Zone (NSZ) and possibly the Møre-Trøndelag Fault Zone (MTFZ, Fig. 2.1) has likely influenced the general direction of lineaments in the region. The north-western part of the study area is influenced by the NSZ (Fig. 2.1) as major lineaments follow E-W shearing. These lineaments closely follow interpolated foliation traces by Wiest et al. (2021) and tend to follow structural boundaries of the Caledonian nappes (Fig.5.8). E-W trending lineaments show an equivalent orientation as the NSZ (Labrousse et al., 2004; Wiest et al., 2021), hence such major lineaments are likely of ductile origin or reactivations of basement foliation , inheriting previously established direction. In the southern part (Fig. 5.8), E-W foliation traces are cut by large N-S trending valleys. These are again cut off by a few E-W valleys/lineaments following the same strike as just further north. The intricate N-S orientation in contrast to the surrounding valleys as well as the similarities to offshore graben structures suggests a tectonic origin. Hillsides show a ~40 - 45° slopes, virtually identical on both sides of each valley. However, it remains to be discussed whether the observed slopes represent fault planes or rather erosional surfaces, which would explain the mechanically unfavored inclination. A similar dip is recoded for the N-S trending Gjøa fault system (Fig. 2.1) offshore of Måløy (Jackson et al., 2008; Reeve et al., 2015). These major N-S trending offshore faults show a throw of >1 km (Reeve et al., 2015). The valleys in the study area, if not objected by a fjord, show a throw of >900 m, some with superimposed glacial erosion surfaces. Minor N-S faults in the offshore sediments show a more typical 60° dip (Reeve et al., 2015). Such steep inclinations are highly uncommon in the study area. Using remote sensing, only one valley with steep valley slopes was found – the NWW-SEE valley in the very centre. Besides N-S trending normal faults, Reeve et al. (2015) also describe plenty of NE-SW striking faults in the offshore Måløy slope, while in the study area a majority of minor lineaments are trending NW-SE. Reeve et al. (2015) interpret the NE-SW faults as reactivated basement foliation of the same trend. In connection with a close-by dextral Sandane Shear Zone (SSZ, Fig. 2.1), these NE-SW faults can be seen as a product of non-coaxial deformation in an E-W trending shear zone. As inland the sense of shearing shifts to the sinistral NSZ, foliation changes direction and rather form NW-SE traces, due to the opposite shear direction. Common NW-SE lineaments can therefore be, similar to offshore observations, interpreted as brittle reactivation of basement foliation. In the eastern part of the study area (Fig. 5.8), the orientation of valleys shifts to NW-SE and a secondary NE-SW orientation. E-W trending lineation almost completely disappear. Most likely the change in orientation is due to a shift in the stress field, either more locally by the Geiranger Shear Zone (GSZ, Fig. 2.1) or due to a regional effect of slip partitioning along the MTFZ (Krabbendam and Dewey, 1998; Fossen, 2000). Walsh et al. (2013) suggest dextral movement somewhat parallel (NNW-SSE) to these N-S valleys. While the observable throw and AFT ages do not differ so much between the valleys, field obser-

vations show plenty of smaller N-S striking lineaments (personal comment Åse Hestnes), suggesting that strike-slip reactivation at a later stage may have played a role. Fossen et al. (2021) show, that fault activity in Nordfjord was still ongoing until the Paleocene. Estimating the throw of a fault with remote sensing can be complicated by a fjord or debris. Reeve et al. (2015) estimate the throw for the minor N-S faults <250 m and for their major N-S > 1 km . With the estimated AFT ages and the exhumation rate of 20.5 m/Myr, inferred from the slope of the upper section of the PAZ (Fig. 6.3), we can estimate the vertical offset between VAH-01 and VAH-02, without relying too much on remote sensing. Since VAH-02 is younger than VAH-01, VAH-02 is expected to be ~290 m lower than VAH-01. Interestingly, VAH-02 is ~600 m higher than expected for its AFT age. That roughly coincides with the estimated offset between VAH-13 and -14 within the Skåla profile. However, if we relate these to potential faults, the assumed fault between VAH-01 and VAH-02 would be perpendicular to the assumed fault at Skåla. Faulting, therefore, likely played a role, not only locally, but affecting a wide area along the passive margin. Several other studies emphasize the high influence of faulting on the present-day topography in SW-Norway (Ksienzyk et al., 2014; Johannessen et al., 2013; Osmundsen and Redfield, 2011). The vertical offset of 600 m could just as well be explained by high relief and warping of isotherms at greater depths, without any fault interaction necessary. Additionally, shorter track lengths of VAH-02 suggest, that this sample spent more time within the PAZ, effectively reducing the AFT age. The exact reason for a longer residence within the PAZ, however, causes the same explanatory dilemma.

6.4.2 Timing of faulting

The local SSZ/ NSZ (Fig. 2.1) was active at ~395 Ma/Lower Devonian (Young et al., 2011). Faults likely inherit intra-basement foliation due to previous shearing (Reeve et al., 2015; Osagiede et al., 2020). Recent K-Ar fault gouge ages by Fossen et al. (2021) close to Sandane (Fig.1.1) show Permian fault activity, as well as reactivation during the Late Paleocene and Mesozoic (Mid Permian, Late Triassic, Middle Jurassic) as well as in the Paleocene, indicating a wide temporal spread in fault reactivation and a tight link to the North Sea rift phases. Offshore lineaments might have been nucleated contemporary during the 2nd rift phase, but while activity in minor NE-SW faults stop in the Jurassic, major N-S valleys continue to be active into Early Cretaceous (Reeve et al., 2015). Likely the same evolution has affected onshore structures. AFT ages of VAH-01; -02; -04 and -05 show Middle Jurassic to Early Cretaceous ages suggesting that N-S trending lineaments may be related to rift phase 2 (ca. 170-140 Ma, Reeve et al., 2015; Fossen et al., 2021). However, as Fossen et al. (2021) points out, reactivation until the Paleocene cannot be ruled out. The topographic evolution is difficult to constrain with only a few samples scattered across a wide area. However, the same evo-

lution, as suggested for the Skåla profile, can easily be applied to the rest of the study area. First a high topography during the Late Triassic and likely fault displacement during the 2nd rift phase. Second, low relief during the Late Cretaceous and subsequent valley carving during the Cenozoic until today. VAH-02 may have been displaced at some point by faulting, placing it higher than the AFT age suggests, but simply variations in topography and high relief could have the same effect. A combination of both can also not be ruled out. VAH-03 is older, compared to other samples, which can be explained by faster erosion or flexural uplift along the fjord. Fault gouge dating could constrain local fault movements better and would be a valuable addition.

6.5 Comparison with previous studies and regional context

With the addition of AFT ages provided by this study a new map of thermal ages from western Norway can be drawn (Fig. 6.9). Figure 6.9 contains all published AFT data between 60 and 62.5 °N including ages from this study with interpolated ages (Andriessen and Bos, 1986; Rohrman et al., 1994, 1995; Leighton, 2007; Johannessen et al., 2013; Ksienzyk et al., 2014; Japsen et al., 2018). The displayed overall age pattern remains similar to results presented by Hendriks et al. (2007).

Apparent outliners within the map are due to differences in sampling altitude. AFT ages in SW-Norway are expected to increase with elevation (e.g. Andriessen and Bos, 1986; Hendriks et al., 2007) and local age variations in figure 6.9 are thus likely a result of higher altitude of sampling location. Still, it becomes obvious that the coast shows older ages than the interior. Based on their widespread ages Rohrman et al. (1995) interpreted the age pattern as a result of domal uplift. Redfield et al. (2004, 2005) highlight the influence of fault block and flexural uplift in the MTFZ (Fig. 2.1) on exhumation. Leighton (2007) adds more AFT ages along Sognefjord and introduces the idea that the Neogene uplift is not necessary to explain apparent ages, similar to the findings of Nielsen et al. (2009). Johannessen et al. (2013) and Ksienzyk et al. (2014) provide extensive AFT ages within Hardanger and the Bergen area and point out that the passive margin evolution may be highly influenced by fault block movement. The interpreted topographic evolution of this study seems to be in line with former thermochronological studies within SW-Norway. In line with other studies, samples of higher elevation cool slightly faster than lower ones that show a delayed cooling in the Cenozoic (Johannessen et al., 2013). While this effect could be considered an artefact of thermal modelling (Miller et al., 2010), the occurrence of this effect in two independent vertical profiles in SW-Norway, suggests that there might be other explanations. Generally, we assume topography to simply erode from top to bottom, exhuming every point at the same pace. However,

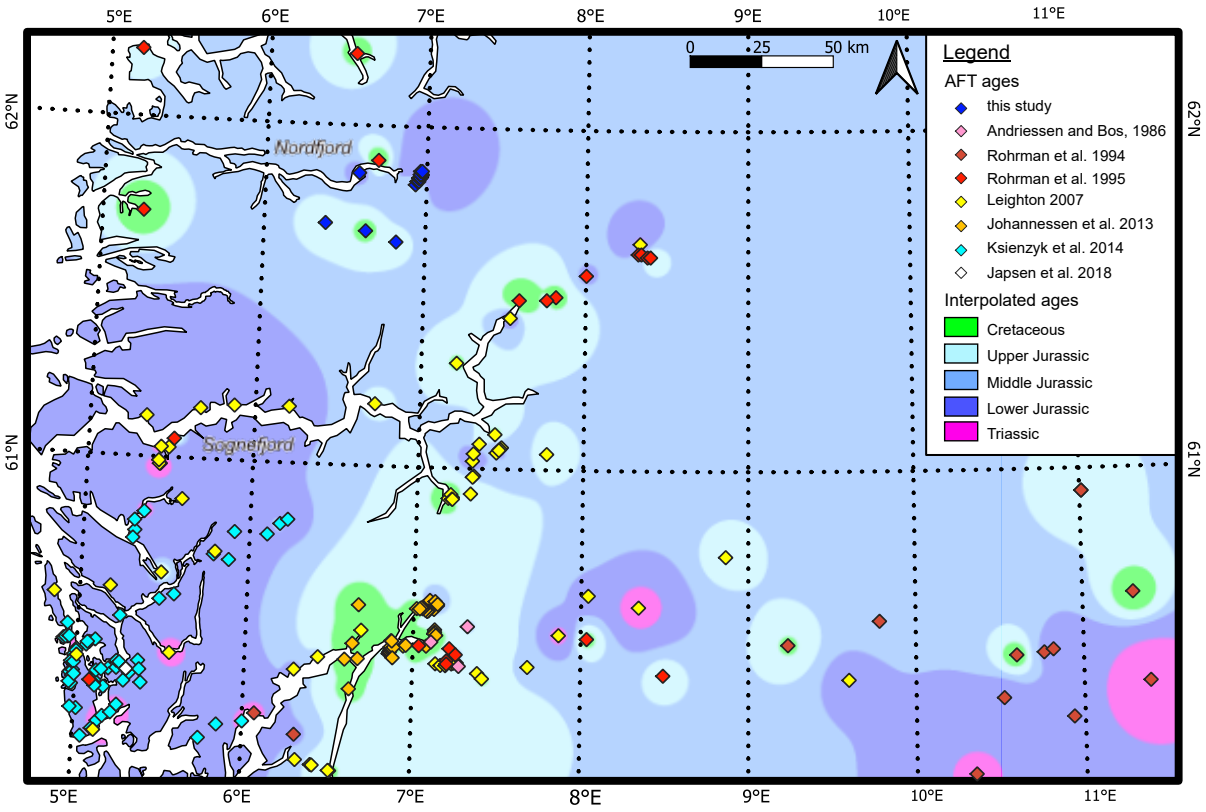

Fig. 6.9: Map of all the published AFT ages between 60 °N and 62.5 °N in Norway including the results of this study. Published ages for each publication are plotted as diamonds. Interpolated ages with discrete colouring according to system/epoch (using QGIS 3.16). Published ages from: Andriessen and Bos (1986); Rohrman et al. (1994, 1995); Leighton (2007); Johannessen et al. (2013); Ksienzyk et al. (2014); Japsen et al. (2018).

this is rarely the case. Instead, erosion is considered to remove material as a function of terrain curvature (Stüwe, 2007). Meaning that over time, hillslope diffusion takes place and a pointy relief slowly smooths out. This process is dependent on several factors e.g. climate, tectonic, lithology etc. However, it serves as a valid explanation for the observed thermal evolution.

6.5.1 Late Paleozoic to Cenozoic cooling

A rapid Permo-Triassic cooling is a common phenomenon in thermochronological studies in SW-Norway (e.g. Leighton, 2007; Johannessen et al., 2013; Ksienzyk et al., 2014). With a cooling rate of 1 – 2 °C/Myr, the cooling is slightly slower in the Nordfjord area than further south. However, the Permo-Triassic timing is consistent with the first rift phase (e.g. Fossen et al., 2021). Detritus transported from the Caledonides to central Europe also argues for rapid exhumation in the Late Triassic (Paul, 1993).

Low Early Jurassic to Cretaceous cooling rates of <1°C/Myr are also common in thermal mod-

els, implying that Late Jurassic North Sea rifting did not significantly affect inland areas (Johannessen et al., 2013; Ksienzyk et al., 2014). While data of this study show the same results, faulting likely occurred during the 2nd rift phase, before the influence of rifting on effective erosion became limited. Fault activity certainly played a significant role in the whole study area and not only within the profile where ages are visibly displaced. However, it is more difficult to constrain the actual influence on the entire study area based on wide-spaced single sample ages.

The Cretaceous is often described as a low relief topography (e.g. Gabrielsen et al., 2010; Sømme et al., 2013) and even with a possible sediment cover (Lidmar-Bergström et al., 2000). Thermal models of VAH-19 do not reject sediment cover (Fig. 6.10). However, Ksienzyk et al. (2014) suggest that only coastal areas had been buried with a thick sediment cover during the Mesozoic. This sediment cover buried samples 1 – 2 km, with its thickness decreasing inland (Fossen et al., 1997; Ksienzyk et al., 2014). Therefore, it is unlikely that samples in the inner Nordfjord area had been buried to a similar extend. Samples from high altitudes in SW-Norway did not reach the surface during the Mesozoic, but still require Cenozoic exhumation (Johannessen et al., 2013; Ksienzyk et al., 2014). This study draws the same conclusion, though additionally shows that the relief during the end of the Mesozoic was likely of low relief. Independent methods that determine the altitude of said low relief surface would truly be invaluable

The removal of 1 - 2 km of overburden during the Cenozoic (Ksienzyk et al., 2014) is consistent with this study, as it is with Johannessen et al. (2013). This suggests that Cenozoic exhumation must have been quite homogeneous in SW-Norway. A recent study by Pedersen et al. (2021) estimate that more than 60 % of the sediment volume in the shelf must be attributed to outside large valleys and fjords. This suggests significant glacial erosion at higher elevations, however, they estimated much less than 1 – 2 km. Further dating of high elevation surfaces may reveal surfaces that experienced less erosion during the Cenozoic. This study also clearly shows higher exhumation within the valleys, indicating differential erosion, likely by glacio-fluvial processes (e.g. Lidmar-Bergström et al., 2000; Pedersen and Egholm, 2013).

6.5.2 Peneplain vs. ICE hypotheses

The results of this study are neither entirely compatible with the ICE (Nielsen et al., 2009) nor the established peneplanation hypothesis (e.g. Gabrielsen et al., 2010). The critical point is if there was Neogene tectonic uplift or not. Low-temperature thermochronology does not discriminate between the causes of cooling. Hence, the data cannot give insights whether there was Neogene tectonic uplift or not.

6.5.2.1 Further constraints for thermal modelling

More constraint boxes were applied on the highest sample VAH-19, in order to test the peneplain hypothesis. If a peneplain were present at some point in the Mesozoic, the Tt-model should show this. Three different constraints were tested, each additional with forced reheating after peneplanation (Fig. 6.10); 1) the constraints allow for peneplanation at any point during the Mesozoic (Fig. 6.10 left), 2) the same constraints as Ksienzyk et al. (2014) were applied for an Upper Jurassic peneplain, based on observation of vitrinite reflectance by Fossen et al. (1997) (Fig. 6.10 centre), and 3) a peneplain in the Late Cretaceous is simulated based on the presented model in Gabrielsen et al. (2010) (Fig. 6.10 right). Peneplanation was modelled with a box that forces a cooling to a maximum of 40°C to allow for up to 2 km of overburden in addition to surface temperature. A similar approach was taken by Ksienzyk et al. (2014). Reheating is constrained as a box from 40 to 80°C starting at the end of the peneplain until present day. Fig. 6.10 shows that if not forced into reheating, the model

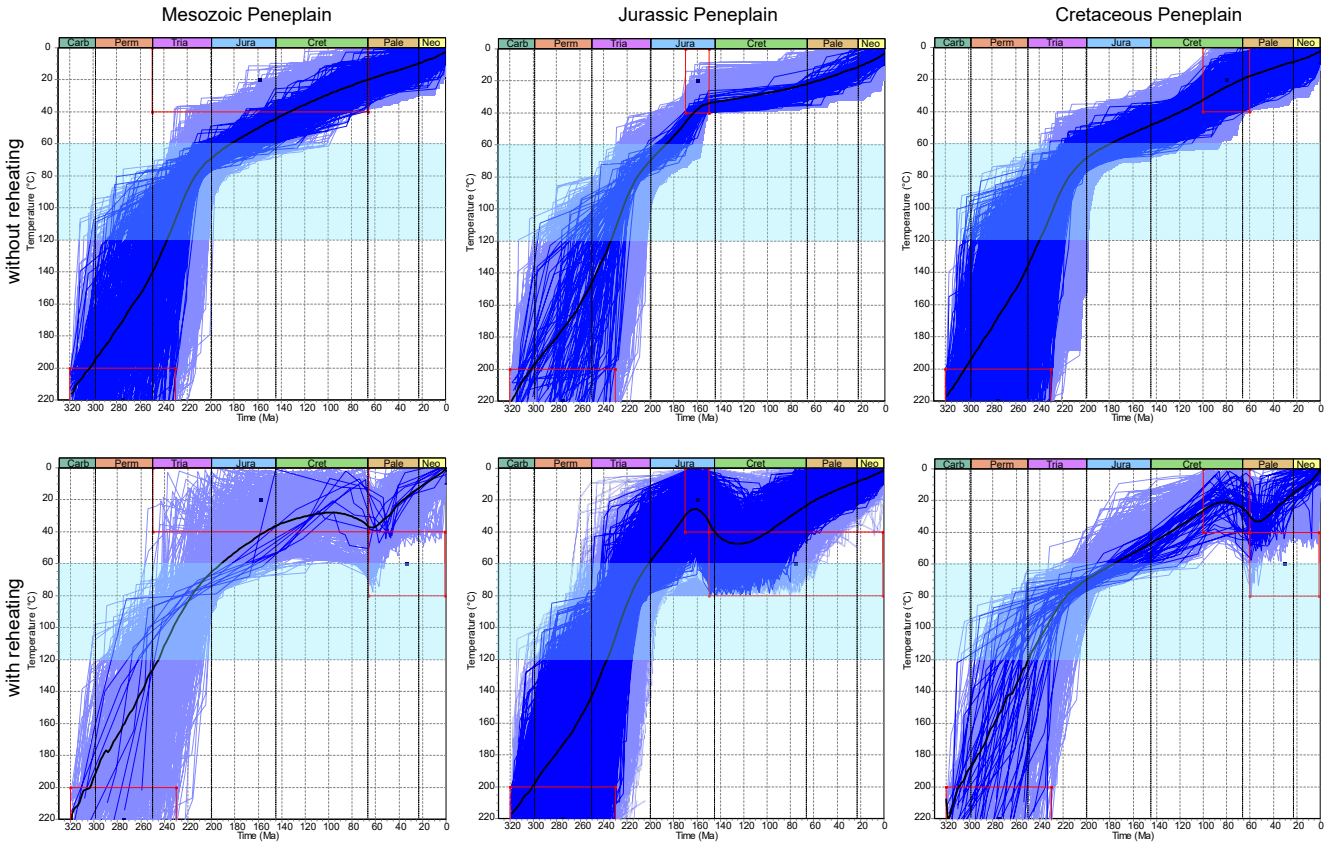

Fig. 6.10: Time-temperature paths with constraints for peneplain hypothesis, with and without reheating. Resurfacing = <40 °C, reheating = 40-80 °C. Dark blue = Good paths, light blue = acceptable paths, Red box = Tt constraints, black= weighted mean average, blue shade= PAZ. Left: Allows for resurfacing at any point during the Mesozoic (250-66 Ma). Centre: Jurassic peneplain (170-150 Ma) based on Ksienzyk et al. (2014). Right: Late Cretaceous peneplain (100-60 Ma) based on Gabrielsen et al. (2010).

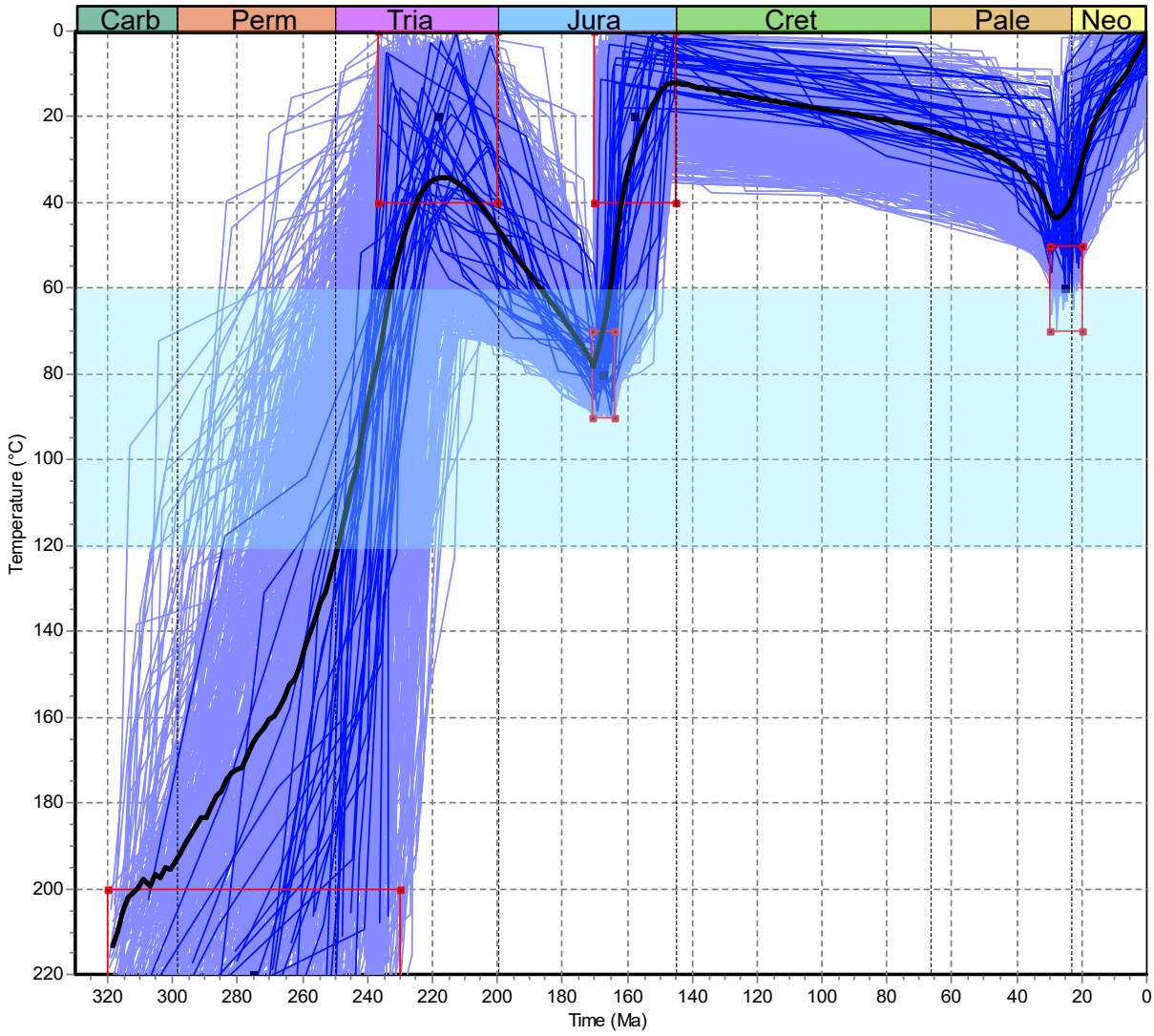

Fig. 6.11: Tt-model recreating heating and cooling history proposed by Japsen et al. (2018) with sample VAH-19. Dark blue = Good paths, light blue = acceptable paths, Red box = Tt constraints, black= weighted mean average, blue shade= PAZ.

remains as loyal to the Tt-path without further constraints (Fig. 5.14 VAH-19) as possible. A rather linear cooling trend is displayed without clear evidence for pre-Cenozoic resurfacing (Fig. 6.10 top). Models that include reheating show, that reburial after the Mesozoic is unlikely. However, reheating after Jurassic peneplanation as suggested by Ksienzyk et al. (2014), produces a loosely constrained model (Fig. 6.10 bottom). The weighted mean average in said model indicates cooling to ~30 °C in the Upper Jurassic and subsequent reheating to ~50 °C during the Lower Cretaceous. A recent study by Japsen et al. (2018) suggests a series of peneplains in Hardangerfjord. They also use thermochronological modelling with peneplanation in the Triassic and Upper Jurassic as well as reheating episodes between and at the end of the Paleogene (Fig. 6.11). Recreating this set of constraints for VAH-19 shows possible solutions,

however with less reheating during the Cenozoic (Fig. 6.11). Forward modelling, following the suggested Tt-path of Japsen et al. (2018) results only in a poor fit of GOF=0.17. Their forward model (Fig. 6.11) is thus considered incompatible with the data of this study and a series of peneplains can be rejected for the inner Nordfjord.

6.5.2.2 Final remarks

The present study suggests that it was very likely that the Late Cretaceous landscape was already of low relief, however, it is unclear at what altitude. In case that this surface was already elevated, Neogene uplift would not have been necessary. It remains unclear, which process could have formed the Late Mesozoic peneplain in such a case. The Cretaceous was a warm period without glaciation (Miller et al., 2005; Stein, 2019), excluding the effect of glacial flattening. Erosion at sea level can also be excluded because even the Cretaceous sea level would not be >1000 m higher than today. The necessary topography also does not need to be completely flat to produce the observed thermal signal. With the given margin of uncertainty, we could also imagine an undulating surface smoothed out by long-term erosion, not necessarily by a transgressing Cretaceous sea.

Since the Cenozoic ~1 km of erosion took place at high elevation, likely by glacial processes (Lidmar-Bergström et al., 2000; Egholm et al., 2017). There is therefore no reason to talk about “paleic” surfaces, considering that surfaces likely would not show a Mesozoic age, when dated. Still, major erosion took mainly place inside valleys and fjords forming deep incisions, similar to the glacial buzzsaw effect described before (e.g. Pedersen and Egholm, 2013; Steer et al., 2012).

6.5.3 Passive margin evolution

The transect of thermochronological data from the coast to the continental interior of Norway can give insights into its topographic evolution. This is useful to constrain the evolution of the margin itself (Sec. 2.4.3). The data fits well with other published AFT ages of Norway considering the increased ages with elevation (Fig. 6.12). Comparing the full data set we can also conclude that the passive margin evolution excludes ‘Scarp retreat model’ and ‘Pinned divide model’ (case B and C in Fig. 6.12, Wildman et al. (2019)), as this would require younger ages at the margin. With old coastal ages the downwarped basal unconformity (A in Fig. 6.12, Ollier and Pain, 1997) remain a possibility or, as Johannessen et al. (2013) proposed, a fault-controlled evolution with footwall uplift (D in Fig. 6.12). The downwarped basal unconformity describes fluvial incision to a base level and escarpment retreat in combination with surface uplift. It also involves the formation of a peneplain (Ollier and Pain,

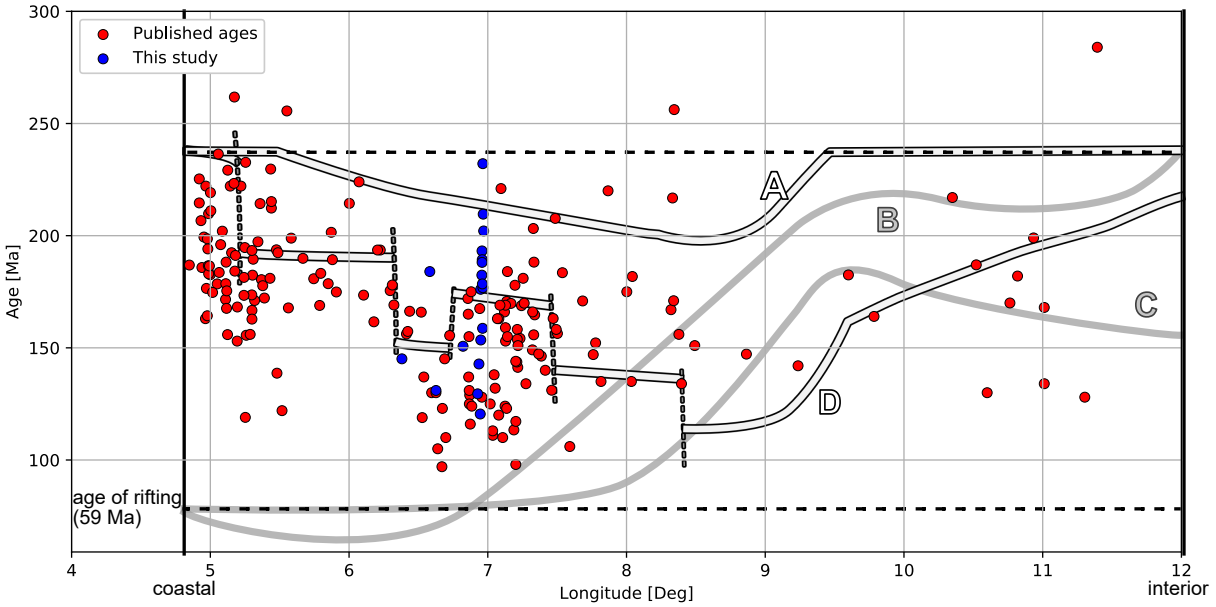

Fig. 6.12: Published AFT ages from coastline to interior between 60 – 62.5 °N in onshore Norway (compare with Fig. 6.9). The ages of this study are in blue. Conceptual models after Ollier and Pain (1997) (A) and Johannessen et al. (2013) (D) with dashed segments indicating fault-related offset. Grey lines: B) 'Scarp retreat model' and C) 'Pinned divide model' can be excluded because these models require young ages at the coastline. Age of rifting corresponds to the last North Atlantic rifting phase after Srivastava and Tapscott (1986). Published ages from: Andriessen and Bos (1986); Rohrman et al. (1994, 1995); Leighton (2007); Johannessen et al. (2013); Ksienzyk et al. (2014); Japsen et al. (2018).

1997). However, the strong local influence of brittle deformation and displacement of thermal ages within the study area leads to the same conclusion as Johannessen et al. (2013): The Norwegian passive margin likely results from a combination of fault-related uplift and regional varying denudation of different tectonic blocks (Redfield et al., 2005; Johannessen et al., 2013; Ksienzyk et al., 2014).

Chapter 7

Conclusions and outlook

From this study these main conclusions can be drawn:

- As expected, AFT ages in the study area increase with elevation. Lower samples show Early Cretaceous ages, while samples collected in higher elevation show Late Triassic ages. The samples experienced generally slow cooling, as evident by the slope of the age-elevation profile, with an estimated exhumation of about 12 – 21 m/Myr.
- Even though the samples were collected along a very steep and less fractured mountain flank, the Skåla profile was likely dissected by a fault nonetheless. The fault has a throw of ~625 m, somewhere between 1070 and 1240 m a.s.l. and can also be identified by slope analysis and remote sensing. AFT ages can also constrain the timing of faulting to post-Middle Jurassic since the closure temperature was already reached before faulting took place. AFT ages outside of the Skåla profile show a similar throw, showing that fault activity along the Norwegian PCM can be significant even within a few km.
- Lineaments in the study area were connected to offshore studies. Mostly NW-SE to NNW-SSE mapped lineament show a tight connection to previously formed basement structure and can therefore be seen as inheritance of basement foliation of the Nordfjord-Shear Zone. N-S trending valleys may be related to N-S striking faults offshore. The timing of faulting is therefore thought to be linked to North Sea rifting, in agreement with other studies constraining fault timing (e.g. Fossen et al., 2021). The faults likely experienced nucleation or reactivation in the Late Jurassic, during the 2nd rift phase and reactivation likely continued until the Paleocene. Fault gauge dating would be required to constrain the timing of faulting even further.
- Thermal history modelling resulted in a distinct thermal signature for all modelled samples – rapid cooling until the Triassic, slow cooling until the onset of the Cenozoic and rapid cooling until they eventually completely exhume in the present day.

However, Late Triassic to Cenozoic cooling showed different velocities, being generally faster in higher elevation, leading to scattering of modelled temperature. During the Late Triassic samples yielded similar temperatures, while by the end of the Cretaceous samples showed a larger temperature difference. By plotting the temperatures at the Cretaceous-Cenozoic boundary over the elevation a modern geothermal gradient of 20.6 ± 3.4 °C/km was inferred, in line with most published geothermal gradients in S-W Norway (Harper, 1971; Evans and Coleman, 1974; Maystrenko et al., 2015). The thermal spacing in the Late Triassic is too low to reflect a reasonable geothermal gradient, suggesting that rather other mechanisms than a change in geothermal gradient resulted in variations of time-temperature paths. The scattering of temperatures during the Mesozoic is interpreted as a change from high to low relief topography and brittle deformation during the 2nd rift phase. Hence, thermal signatures reflect the warping of isotherms in combination with fault related displacement of samples.

- This study concludes that the topography had a high relief during the Triassic to Early Jurassic and was subsequently subdued (in agreement with Gabrielsen et al., 2010; Sømme et al., 2013). The topography was likely of low relief at the end of the Mesozoic, but low-temperature thermochronology data cannot resolve at which elevation. This low relief surface was surely further worn down, by perhaps 1 km, during the Cenozoic (Pedersen and Egholm, 2013; Pedersen et al., 2021). During Cenozoic valley carving commenced by shaping the deep valleys and exhuming samples at lower elevations.

- In light of the ongoing debate between Neogene uplift or ICE, this study remains rather inconclusive. While the data suggest a low relief surface at the end of the Mesozoic, modern surfaces are younger and have not been preserved during the Cenozoic. This study cannot provide insights into whether there was Neogene uplift or not, since the low relief surface might as well have been at a high altitude already. However, due to the significant influence of fault displacement within the study area, this study can conclude, that the PCM evolution must have been strongly influenced by faulting, agreeing with previous AFT studies in SW-Norway (Johannessen et al., 2013; Ksienzyk et al., 2014).

- For further insights into the thermal history of the inner Nordfjord, AHe data would be truly valuable, as this would allow for a higher resolution at the lower temperature range, ultimately confirming the modelled thermal spacing during the Late Cretaceous. The golden goose would be a better estimate for surface removal of low relief surfaces and a better way to figure out the paleo-altitude of SW-Norway.

References

Ali, A. and S. Durrani (1977). Etched-track kinetics in isotropic detectors. *Nuclear Track Detection 1*(2), 107–121.

Allen, P. A. (2008). Time scales of tectonic landscapes and their sediment routing systems. *Geological Society, London, Special Publications 296*(1), 7–28.

Andriessen, P. A. and A. Bos (1986). Post-caledonian thermal evolution and crustal uplift in the eidfjord area, western norway. *Norsk geologisk tidsskrift 66*(3), 243–250.

Aune, B. (1992). Temperaturnormaler, normalperiode 1961-90 (temperature normals, normal period 1961-90). *Rapport 2*, 93.

Baard, J. H., W. L. Zijp, and H. J. Nolthenius (1989). *Nuclear data guide for reactor neutron metrology*, Volume 12354. Springer Science
and Business Media.

Barbarand, J., T. Hurford, and A. Carter (2003). Variation in apatite fission-track length measurement: implications for thermal history modelling. *Chemical Geology 198*(1-2), 77–106.

Baumhauer, H. A. (1894). *Die resultate der aetzmethode: in der krystallographischen forschung, an einer reihe von krystallisirten körpern dargestellt*, Volume 1. W. Engelmann.

Bhandari, N., S. Bhat, D. Lal, G. Rajagopalan, A. Tamhane, and V. Venkatavaradan (1971). Fission fragment tracks in apatite: recordable track lengths. *Earth and Planetary Science Letters 13*(1), 191–199.

Bigazzi, G. (1967). Length of fission tracks and age of muscovite samples. *Earth and Planetary Science Letters 3*, 434–438.

Bingen, B., Ø. Skår, M. Marker, E. M. Sigmond, Ø. Nordgulen, J. Ragnhildstveit, J. Mansfeld, R. D. Tucker, and J.-P. Liégeois (2005). Timing of continental building in the sveconorwegian orogen, sw scandinavia. *Norwegian Journal of Geology/Norsk Geologisk Forening 85*.

Bogdanova, S. V., B. Bingen, R. Gorbatschev, T. N. Kheraskova, V. I. Kozlov, V. N. Puchkov, and Y. A. Volozh (2008). The east european craton (baltica) before and during the assembly of rodinia. *Precambrian Research 160*(1-2), 23–45.

Bottrill, A. D., J. Van Hunen, S. J. Cuthbert, H. K. Brueckner, and M. B. Allen (2014). Plate rotation during continental collision and its relationship with the exhumation of uhp metamorphic terranes: Application to the norwegian caledonides. *Geochemistry, Geophysics, Geosystems 15*(5), 1766–1782.

Braun, J. (2002). Quantifying the effect of recent relief changes on age–elevation relationships. *Earth and Planetary Science Letters 200*(3-4), 331–343.

Braun, J. (2016). Strong imprint of past orogenic events on the thermochronological record. *Tectonophysics 683*, 325–332.

Bray, R., P. Green, and I. Duddy (1992). Thermal history reconstruction using apatite fission track analysis and vitrinite reflectance: a case study from the uk east midlands and southern north sea. *Geological Society, London, Special Publications 67*(1), 3–25.

Brown, R. W. and M. Summerfield (1997). Some uncertainties in the derivation of rates of denudation from thermochronologic data. *Earth Surface Processes and Landforms: The Journal of the British Geomorphological Group 22*(3), 239–248.

Burtner, R. L., A. Nigrini, and R. A. Donelick (1994). Thermochronology of lower cretaceous source rocks in the idaho-wyoming thrust belt. *AAPG bulletin 78*(10), 1613–1636.

Butler, J. P., C. Beaumont, and R. A. Jamieson (2015). Paradigm lost: Buoyancy thwarted by the strength of the western gneiss region (ultra)high-pressure terrane, norway. *Lithosphere 7*(4), 379–407.

Carlson, W. D., R. A. Donelick, and R. A. Ketcham (1999). Variability of apatite fission-track annealing kinetics: I. experimental results. *American mineralogist 84*(9), 1213–1223.

Chadderton, L. T. (1988). On the anatomy of a fission fragment track. *International Journal of Radiation Applications and Instrumentation. Part D. Nuclear Tracks and Radiation Measurements 15*(1-4), 11–29.

Chadderton, L. T. (2003). Nuclear tracks in solids: registration physics and the compound spike. *Radiation measurements 36*(1-6), 13–34.

Chalmers, J., P. Green, P. Japsen, and E. Rasmussen (2010). The scandinavian mountains have not persisted since the caledonian orogeny. a comment on nielsen et al.(2009a). *Journal of Geodynamics 50*(2), 94–101.

Corfu, F., T. B. Andersen, and D. Gasser (2014). The scandinavian caledonides: main features, conceptual advances and critical questions. *Geological Society, London, Special Publications 390*(1), 9–43.

Cowan, G. A. and H. H. Adler (1976). The variability of the natural abundance of 235u. *Geochimica et Cosmochimica Acta 40*(12), 1487–1490.

Crowley, K., M. Cameron, and R. Schaefer (1991). Experimental studies of annealing of etched fission tracks in fluorapatite. *Geochimica et Cosmochimica Acta 55*(5), 1449–1465.

Dahl, S. O. and A. Nesje (1992). Paleoclimatic implications based on equilibrium-line altitude depressions of reconstructed younger dryas and holocene cirque glaciers in inner nordfjord, western norway. *Palaeogeography, Palaeoclimatology, Palaeoecology 94*(1-4), 87–97.

Donelick, R. (1993). A method of fission track analysis utilizing bulk chemical etching of apatite, patent 5267274. *US Patent and Trademark Off., Washington, DC*.

Donelick, R. (1995). A method of fission track analysis utilizing bulk chemical etching of apatite, patent 658,800. *Australian Patent*.

Donelick, R. A., R. A. Ketcham, and W. D. Carlson (1999). Variability of apatite fission-track annealing kinetics: Ii. crystallographic orientation effects. *American Mineralogist 84*(9), 1224–1234.

Donelick, R. A., P. O'sullivan, and R. Ketcham (2005). *Apatite Fission-Track Analysis*, Volume 58, pp. 49–94.

Doré, A. (1992). The base tertiary surface of southern norway and the northern north sea. *Norsk Geologisk Tidsskrift 72*(3), 259–265.

Doré, A., E. Lundin, L. Jensen, Ø. Birkeland, P. Eliassen, and C. Fichler (1999). Principal tectonic events in the evolution of the northwest european atlantic margin. *5*, 41–61.

Dumitru, T. A. (1991). Effects of subduction parameters on geothermal gradients in forearcs, with an application to franciscan subduction in california. *Journal of Geophysical Research: Solid Earth 96*(B1), 621–641.

Dumitru, T. A. (1993). A new computer-automated microscope stage system for fission-track analysis. *Nuclear Tracks and Radiation Measurements 21*(4), 575–580.

Dunkl, I. (2002). Trackkey: a windows program for calculation and graphical presentation of fission track data. *Computers and Geosciences 28*(1), 3–12.

Duretz, T., T. V. Gerya, B. J. P. Kaus, and T. B. Andersen (2012). Thermomechanical modeling of slab eduction. *Journal of Geophysical Research: Solid Earth 117*(B8), n/a–n/a.

Egholm, D. L., J. D. Jansen, C. F. Brædstrup, V. K. Pedersen, J. L. Andersen, S. V. Ugelvig, N. K. Larsen, and M. F. Knudsen (2017). Formation of plateau landscapes on glaciated continental margins. *Nature Geoscience 10*(8), 592–597.

England, P. and P. Molnar (1990). Surface uplift, uplift of rocks, and exhumation of rocks. *Geology 18*(12), 1173–1177.

Evans, T. R. and N. Coleman (1974). North sea geothermal gradients. *Nature 247*(5435), 28–30.

Færseth, R. (1996). Interaction of permo-triassic and jurassic extensional fault-blocks during the development of the northern north sea. *Journal of the Geological Society 153*(6), 931–944.

Faleide, J. I., F. Tsikalas, A. J. Breivik, R. Mjelde, O. Ritzmann, O. Engen, J. Wilson, and O. Eldholm (2008). Structure and evolution of the continental margin off norway and the barents sea. *Episodes 31*(1), 82–91.

Fitzgerald, P. and M. Malusà (2018). Chapter 9. concept of the exhumed partial annealing (retention) zone and age-elevation profiles in thermochronology. *Fission-track thermochronology and its application to geology. Springer*.

Fitzgerald, P. G. and A. J. Gleadow (1990). New approaches in fission track geochronology as a tectonic tool: Examples from the transantarctic mountains. *International Journal of Radiation Applications and Instrumentation. Part D. Nuclear Tracks and Radiation Measurements 17*(3), 351–357.

Fitzgerald, P. G., R. B. Sorkhabi, T. F. Redfield, and E. Stump (1995). Uplift and denudation of the central alaska range: A case study in the use of apatite fission track thermochronology to determine absolute uplift parameters. *Journal of Geophysical Research: Solid Earth 100*(B10), 20175–20191.

Fitzgerald, P. G. and E. Stump (1997). Cretaceous and cenozoic episodic denudation of the transantarctic mountains, antarctica: New constraints from apatite fission track thermochronology in the scott glacier region. *Journal of Geophysical Research: Solid Earth 102*(B4), 7747–7765.

Fleischer, R., P. Price, and R. Walker (1965). Effects of temperature, pressure, and ionization of the formation and stability of fission tracks in minerals and glasses. *Journal of Geophysical Research 70*(6), 1497–1502.

Fleischer, R. L. and P. B. Price (1964). Techniques for geological dating of minerals by chemical etching of fission fragment tracks. *Geochimica et Cosmochimica Acta 28*(10-11), 1705–1714.

Fleischer, R. L., P. B. Price, R. M. Walker, and R. M. Walker (1975). *Nuclear tracks in solids: principles and applications*. Univ of California Press.

Fossen, H. (1992). The role of extensional tectonics in the caledonides of south norway. *Journal of structural geology 14*(8-9), 1033–1046.

Fossen, H. (2000). Extensional tectonics in the caledonides: Synorogenic or postorogenic? *Tectonics 19*(2), 213–224.

Fossen, H. (2010). Extensional tectonics in the north atlantic caledonides: a regional view. *Geological Society, London, Special Publications 335*(1), 767–793.

Fossen, H. and W. J. Dunlap (1998). Timing and kinematics of caledonian thrusting and extensional collapse, southern norway: evidence from 40ar/39ar thermochronology. *Journal of structural geology 20*(6), 765–781.

Fossen, H. and W. J. Dunlap (1999). On the age and tectonic significance of permo-triassic dikes in the bergen-sunnhordland region, southwestern norway. *Norsk Geologisk Tidsskrift 79*(3), 169–178.

Fossen, H. and T. B. Holst (1995). Northwest-verging folds and the northwestward movement of the caledonian jotun nappe, norway. *Journal of Structural Geology 17*(1), 3–15.

Fossen, H. and C. A. Hurich (2005). The hardangerfjord shear zone in sw norway and the north sea: a large-scale low-angle shear zone in the caledonian crust. *Journal of the Geological Society 162*(4), 675–687.

Fossen, H., H. F. Khani, J. I. Faleide, A. K. Ksienzyk, and W. J. Dunlap (2017). Post-caledonian extension in the west norway–northern north sea region: the role of structural inheritance. *Geological Society, London, Special Publications 439*(1), 465–486.

Fossen, H., A. K. Ksienzyk, A. Rotevatn, M. S. Bauck, and K. Wemmer (2021). From widespread faulting to localised rifting: Evidence from k-ar fault gouge dates from the norwegian north sea rift shoulder. *Basin Research 33*(3), 1934–1953.

Fossen, H., G. Mangerud, J. Hesthammer, T. Bugge, and R. H. Gabrielsen (1997). The bjorøy formation: a newly discovered occurrence of jurassic sediments in the bergen arc system. *Norsk Geologisk Tidsskrift 77*(4), 269–287.

Gabrielsen, R., A. Braathen, J. Dehls, and D. Roberts (2002). Tectonic lineaments of norway. *Norwegian Journal of Geology 82*, 153–174.

Gabrielsen, R. H., J. I. Faleide, C. Pascal, A. Braathen, J. P. Nystuen, B. Etzelmuller, and S. O'donnell (2010). Latest caledonian to present tectonomorphological development of southern norway. *Marine and Petroleum Geology 27*(3), 709–723.

Gabrielsen, R. H., J. P. Nystuen, and O. Olesen (2018). Fault distribution in the precambrian basement of south norway. *Journal of Structural Geology 108*, 269–289.

Galbraith, R. F. (1990). The radial plot: graphical assessment of spread in ages. *International Journal of Radiation Applications and Instrumentation. Part D. Nuclear Tracks and Radiation Measurements 17*(3), 207–214.

Galbraith, R. F. (2005). *Statistics for fission track analysis*. Chapman and Hall/CRC.

Galbraith, R. F. and G. M. Laslett (1993). Statistical models for mixed fission track ages. *Nuclear tracks and radiation measurements 21*(4), 459–470.

Gallagher, K. and R. Brown (1999). Denudation and uplift at passive margins: the record on the atlantic margin of southern africa. *Philosophical Transactions of the Royal Society of London. Series A: Mathematical, Physical and Engineering Sciences 357*(1753), 835–859.

Gallagher, K., R. Brown, and C. Johnson (1998). Fission track ananlysis and its application to geological problems. *Annual Review of Earth and Planetary Sciences 26*(1), 519–572.

Gee, D. G., H. Fossen, N. Henriksen, and A. K. Higgins (2008). From the early paleozoic platforms of baltica and laurentia to the caledonide orogen of scandinavia and greenland. *Episodes 31*(1), 44–51.

Gentner, W., B. Kleinmann, and G. Wagner (1967). New k-ar and fission track ages of impact glasses and tektites. *Earth and Planetary Science Letters 2*(2), 83–86.

Gholamrezaie, E., M. Scheck-Wenderoth, J. Sippel, and M. R. Strecker (2018). Variability of the geothermal gradient across two differently aged magma-rich continental rifted margins of the atlantic ocean: the southwest african and the norwegian margins. *Solid Earth 9*(1), 139–158.

Gilchrist, A. and M. Summerfield (1990). Differential denudation and flexural isostasy in formation of rifted-margin upwarps. *Nature 346*(6286), 739–742.

Gleadow, A., Duddy, Ir, and J. Lovering (1983). Fission track analysis: a new tool for the evaluation of thermal histories and hydrocarbon potential. *The APPEA Journal 23*(1), 93–102.

Gleadow, A. and I. Duddy (1981). A natural long-term track annealing experiment for apatite. *Nuclear Tracks 5*(1-2), 169–174.

Gleadow, A., I. Duddy, P. F. Green, and J. Lovering (1986). Confined fission track lengths in apatite: a diagnostic tool for thermal history analysis. *Contributions to Mineralogy and Petrology 94*(4), 405–415.

Gleadow, A. and P. Fitzgerald (1987). Uplift history and structure of the transantarctic mountains: new evidence from fission track dating of basement apatites in the dry valleys area, southern victoria land. *Earth and planetary science letters 82*(1-2), 1–14.

Gleadow, A., B. Kohn, and C. Seiler (2019). *The future of fission-track thermochronology*, pp. 77–92. Springer.

Gleadow, A. J., R. W. Brown, et al. (2000). Fission-track thermochronology and the long-term denudational response to tectonics. *Geomorphology and global tectonics*, 57–75.

Green, P., I. Duddy, A. Gleadow, P. Tingate, and G. Laslett (1986). Thermal annealing of fission tracks in apatite: 1. a qualitative description. *Chemical Geology: Isotope Geoscience Section 59*, 237–253.

Green, P. and S. Durrani (1977). Annealing studies of tracks in crystals. *Nuclear Track Detection 1*(1), 33–39.

Hacker, B. R., T. B. Andersen, S. Johnston, A. R. C. Kylander-Clark, E. M. Peterman, E. O. Walsh, and D. Young (2010). High-temperature deformation during continental-margin subduction and exhumation: The ultrahigh-pressure western gneiss region of norway. *Tectonophysics 480*(1-4), 149–171.

Hall, A. M., K. Ebert, J. Kleman, A. Nesje, and D. Ottesen (2013). Selective glacial erosion on the norwegian passive margin. *Geology 41*(12), 1203–1206.

Harper, M. (1971). Approximate geothermal gradients in the north sea basin. *Nature 230*(5291), 235–236.

Hendriks, B., P. Andriessen, Y. Huigen, C. Leighton, T. Redfield, G. Murrell, K. Gallagher, and S. B. Nielsen (2007). A fission track data compilation for fennoscandia. *Norwegian Journal of Geology/Norsk Geologisk Forening 87*.

Holden, N. E. (1989). Total and spontaneous fission half-lives for uranium, plutonium, americium and curium nuclides. *Pure and Applied Chemistry 61*(8), 1483–1504.

Hurford, A. J. (1990). Standardization of fission track dating calibration: Recommendation by the fission track working group of the iugs subcommission on geochronology. *Chemical Geology: Isotope Geoscience Section 80*(2), 171–178.

Hurford, A. J. (2019). An historical perspective on fission-track thermochronology. *Fission-Track Thermochronology and its application to geology*, 3–23.

Hurford, A. J. and A. Carter (1991). The role of fission track dating in discrimination of provenance. *Geological Society, London, Special Publications 57*(1), 67–78.

Hurford, A. J. and P. F. Green (1983). The zeta age calibration of fission-track dating. *Chemical Geology 41*, 285–317.

Hurford, A. J. and K. Hammerschmidt (1985). 40ar39ar and k/ar dating of the bishop and fish canyon tuffs: Calibration ages for fission-track dating standards. *Chemical Geology: Isotope Geoscience section 58*(1-2), 23–32.

Jackson, C. A.-L., G. P. Barber, and O. J. Martinsen (2008). Submarine slope morphology as a control on the development of sand-rich turbidite depositional systems: 3d seismic analysis of the kyrre fm (upper cretaceous), måløy slope, offshore norway. *Marine and Petroleum Geology 25*(8), 663–680.

Jaffey, A., K. Flynn, L. Glendenin, W. T. Bentley, and A. Essling (1971). Precision measurement of half-lives and specific activities of u 235 and u 238. *Physical review C 4*(5), 1889.

Jakob, J., T. B. Andersen, and H. J. Kjøll (2019). A review and reinterpretation of the architecture of the south and south-central scandinavian caledonides—a magma-poor to magma-rich transition and the significance of the reactivation of rift inherited structures. *Earth-Science Reviews 192*, 513–528.

Japsen, P. and J. A. Chalmers (2000). Neogene uplift and tectonics around the north atlantic: overview. *Global and Planetary Change 24*(3-4), 165–173.

Japsen, P., P. F. Green, J. A. Chalmers, and J. M. Bonow (2018). Mountains of southernmost norway: uplifted miocene peneplains and re-exposed mesozoic surfaces. *Journal of the Geological Society 175*(5), 721–741.

Johannessen, K. C., F. Kohlmann, A. K. Ksienzyk, I. Dunkl, and J. Jacobs (2013). Tectonic evolution of the sw norwegian passive margin based on low-temperature thermochronology from the innermost hardangerfjord area. *Norwegian Journal of Geology/Norsk Geologisk Forening 93*.

Jonckheere, R. (2003). On the densities of etchable fission tracks in a mineral and co-irradiated external detector with reference to fission-track dating of minerals. *Chemical Geology 200*(1-2), 41–58.

Jonckheere, R. C. and G. A. Wagner (2000). On the occurrence of anomalous fission tracks in apatite and titanite. *American Mineralogist 85*(11-12), 1744–1753.

Kartverket.no. Digital elevation model. https://hoydedata.no/LaserInnsyn/.

Ketcham, R. (2017). Hefty version 1.9. 3. program.

Ketcham, R. A. (2003). Observations on the relationship between crystallographic orientation and biasing in apatite fission-track measurements. *American Mineralogist 88*(5-6), 817–829.

Ketcham, R. A. (2018). Fission-track annealing: From geologic observations to thermal history modeling. *Fission-Track Thermochronology and its Application to Geology*, 49.

Ketcham, R. A., A. Carter, R. A. Donelick, J. Barbarand, and A. J. Hurford (2007). Improved modeling of fission-track annealing in apatite. *American Mineralogist 92*(5-6), 799–810.

Ketcham, R. A., A. Carter, and A. J. Hurford (2015). Inter-laboratory comparison of fission track confined length and etch figure measurements in apatite. *American Mineralogist 100*(7), 1452–1468.

Kim, Y., M. Huh, and E. Y. Lee (2020). Numerical modelling to evaluate sedimentation effects on heat flow and subsidence during continental rifting. *Geosciences 10*(11), 451.

Kohn, B., L. Chung, and A. Gleadow (2019). *Fission-track analysis: field collection, sample preparation and data acquisition*, pp. 25–48. Springer.

Kooi, H. and C. Beaumont (1994). Escarpment evolution on high-elevation rifted margins: Insights derived from a surface processes model that combines diffusion, advection, and reaction. *Journal of Geophysical Research: Solid Earth 99*(B6), 12191–12209.

Krabbendam, M. and J. F. Dewey (1998). Exhumation of uhp rocks by transtension in the western gneiss region, scandinavian caledonides. *Geological Society, London, Special Publications 135*(1), 159–181.

Ksienzyk, A. K., I. Dunkl, J. Jacobs, H. Fossen, and F. Kohlmann (2014). From orogen to passive margin: constraints from fission track and (u–th)/he analyses on mesozoic uplift and fault reactivation in sw norway. *Geological Society, London, Special Publications 390*(1), 679–702.

Ksienzyk, A. K., K. Wemmer, J. Jacobs, H. Fossen, A. C. Schomberg, A. Süssenberger, N. K. Lünsdorf, and E. Bastesen (2016). Post-caledonian brittle deformation in the bergen area, west norway: results from k–ar illite fault gouge dating. *Norwegian Journal of Geology*.

Labrousse, L., L. Jolivet, T. Andersen, P. Agard, R. Hébert, H. Maluski, and U. Scharer (2004). Pressure-temperature-time deformation history of the exhumation of ultra-high pressure rocks in the western gneiss region, norway. *SPECIAL PAPERS-GEOLOGICAL SOCIETY OF AMERICA*, 155–184.

Lal, D., R. Rajan, and A. Tamhane (1969). Chemical composition of nuclei of z> 22 in cosmic rays using meteoritic minerals as detectors. *Nature 221*(5175), 33–37.

Laslett, G., A. Gleadow, and I. Duddy (1984). The relationship between fission track length and track density in apatite. *Nuclear Tracks and Radiation Measurements (1982) 9*(1), 29–38.

Laslett, G., W. Kendall, A. Gleadow, and I. Duddy (1982). Bias in measurement of fission-track length distributions. *Nuclear Tracks and Radiation Measurements (1982) 6*(2-3), 79–85.

Leighton, C. A. (2007). *The thermotectonic development of southern Norway: constraints from low-temperature thermochronology*. Thesis.

Li, W., M. Lang, A. J. Gleadow, M. V. Zdorovets, and R. C. Ewing (2012). Thermal annealing of unetched fission tracks in apatite. *Earth and Planetary Science Letters 321*, 121–127.

Li, Y., Z. Jiang, S. Jiang, H. Liu, and B. Wang (2019). Heat flow and thermal evolution of a passive continental margin from shelf to slope–a case study on the pearl river mouth basin, northern south china sea. *Journal of Asian Earth Sciences 171*, 88–102.

Lidmar-Bergström, K., C. Ollier, and J. Sulebak (2000). Landforms and uplift history of southern norway. *Global and Planetary Change 24*(3-4), 211–231.

Lidmar-Bergström, K. and J. M. Bonow (2009). Hypotheses and observations on the origin of the landscape of southern norway—a comment regarding the isostasy-climate-erosion hypothesis by nielsen et al. 2008. *Journal of Geodynamics 48*, 95–100.

Lisker, F., B. Ventura, and U. Glasmacher (2009). Apatite thermochronology in modern geology. *Geological Society, London, Special Publications 324*(1), 1–23.

Łuszczak, K., C. Persano, J. Braun, and F. M. Stuart (2017). How local crustal thermal properties influence the amount of denudation derived from low-temperature thermochronometry. *Geology 45*(9), 779–782.

Malusà, M. G. and P. G. Fitzgerald (2019a). *Fission-track thermochronology and its application to geology*. Springer.

Malusà, M. G. and P. G. Fitzgerald (2019b). *From cooling to exhumation: setting the reference frame for the interpretation of thermochronologic data*, pp. 147–164. Springer.

Maystrenko, Y. P., H. K. Elvebakk, M. Osinska, and O. Olesen (2021). New heat flow data from the veiholmen and raudsand boreholes, middle norway. *Geothermics 89*, 101964.

Maystrenko, Y. P., T. Slagstad, H. K. Elvebakk, O. Olesen, G. V. Ganerød, and J. S. Rønning (2015). New heat flow data from three boreholes near bergen, stavanger and moss, southern norway. *Geothermics 56*, 79–92.

Mcdowell, F. and R. Keizer (1977). Timing of mid-tertiary volcanism in the sierra madre occidental between durango city and mazatlán, mexico. *Geological Society of America Bulletin 88*(10), 1479–1487.

Mcdowell, F. W., W. C. Mcintosh, and K. A. Farley (2005). A precise 40ar–39ar reference age for the durango apatite (u–th)/he and fission-track dating standard. *Chemical Geology 214*(3-4), 249–263.

Metha, P. P. and Rama (1969). Annealing effects in muscovite and their influence on dating by fission track method. *Earth and Planetary Science Letters 7*(1), 82–86.

Miller, K. G., M. A. Kominz, J. V. Browning, J. D. Wright, G. S. Mountain, M. E. Katz, P. J. Sugarman, B. S. Cramer, N. Christie-Blick, and S. F. Pekar (2005). The phanerozoic record of global sea-level change. *science 310*(5752), 1293–1298.

Miller, S. R., P. G. Fitzgerald, and S. L. Baldwin (2010). Cenozoic range-front faulting and development of the transantarctic mountains near cape surprise, antarctica: Thermochronologic and geomorphologic constraints. *Tectonics 29*(1).

Mosar, J. (2003). Scandinavia's north atlantic passive margin. *Journal of Geophysical Research: Solid Earth 108*(B8).

Naeser, C. (1967). The use of apatite and sphene for fission track age determinations. *Geological Society of America Bulletin 78*(12), 1523–1526.

NGU. Norges geologiske undersøkelse: Bedrock map. https://geo.ngu.no/kart/berggrunn_mobil/. Last checked: 16.08.2021.

Nielsen, S. B., K. Gallagher, C. Leighton, N. Balling, L. Svenningsen, B. H. Jacobsen, E. Thomsen, O. B. Nielsen, C. Heilmann-Clausen, D. L. Egholm, M. A. Summerfield, O. R. Clausen,

J. A. Piotrowski, M. R. Thorsen, M. Huuse, N. Abrahamsen, C. King, and H. Lykke-Andersen (2009). The evolution of western scandinavian topography: A review of neogene uplift versus the ice (isostasy–climate–erosion) hypothesis. *Journal of Geodynamics 47*(2-3), 72–95.

Norgeskart.no. Orthophoto. https://kartkatalog.geonorge.no/metadata/norge-i-bilder-wms-ortofoto/dcee8bf4-fdf3-4433-a91b-209c7d9b0b0f.

Norton, M. G. (1987). The nordfjord-sogn detachment, w. norway. *Norsk Geologisk Tidsskrift 67*(2), 93–106.

Ollier, C. D. and C. F. Pain (1997). Equating the basal unconformity with the palaeoplain: a model for passive margins. *Geomorphology 19*(1), 1–15.

Osagiede, E. E., A. Rotevatn, R. Gawthorpe, T. B. Kristensen, C. A. Jackson, and N. Marsh (2020). Pre-existing intra-basement shear zones influence growth and geometry of non-colinear normal faults, western utsira high–heimdal terrace, north sea. *Journal of Structural Geology 130*, 103908.

Osmundsen, P. T. and T. Redfield (2011). Crustal taper and topography at passive continental margins. *Terra Nova 23*(6), 349–361.

Pascal, C., H. Elvebakk, and O. Olesen (2010). An assessment of deep geothermal resources in norway. In *Abstracts and Proceedings, World Geothermal Congress, 25–29 April, Bali, Indonesia*.

Paul, T. (1993). Transmission electron microscopy investigation of unetched fission tracks in fluorapatite—physical process of annealing. *Nuclear Tracks and Radiation Measurements 21*(4), 507–511.

Paulick, J. and H. Newesely (1968). Zur kenntis der apatite der cerro de mercado, durango, mexiko. neu jb mineral. *Mh 1*(2), 224–235.

Pedersen, V. K. and D. L. Egholm (2013). Glaciations in response to climate variations preconditioned by evolving topography. *Nature 493*(7431), 206–210.

Pedersen, V. K., R. S. Huismans, and R. Moucha (2016). Isostatic and dynamic support of high topography on a north atlantic passive margin. *Earth and Planetary Science Letters 446*, 1–9.

Pedersen, V. K., Å. R. Knutsen, G. Pallisgaard-Olesen, J. L. Andersen, R. Moucha, and R. S. Huismans (2021). Widespread glacial erosion on the scandinavian passive margin. *Geology*.

Price, P. and R. Walker (1963). Fossil tracks of charged particles in mica and the age of minerals. *Journal of Geophysical Research 68*(16), 4847–4862.

Ravenhurst, C. E., M. K. Roden-Tice, and D. S. Miller (2003). Thermal annealing of fission tracks in fluorapatite, chlorapatite, manganoanapatite, and durango apatite: experimental results. *Canadian Journal of Earth Sciences 40*(7), 995–1007.

Redfield, T., A. Braathen, R. Gabrielsen, P. Osmundsen, T. Torsvik, and P. Andriessen (2005). Late mesozoic to early cenozoic components of vertical separation across the møre–trøndelag fault complex, norway. *Tectonophysics 395*(3-4), 233–249.

Redfield, T., T. Torsvik, P. Andriessen, and R. Gabrielsen (2004). Mesozoic and cenozoic tectonics of the møre trøndelag fault complex, central norway: constraints from new apatite fission track data. *Physics and Chemistry of the Earth, Parts A/B/C 29*(10), 673–682.

Reeve, M. T., R. E. Bell, O. B. Duffy, C. a.-L. Jackson, and E. Sansom (2015). The growth of non-colinear normal fault systems; what can we learn from 3d seismic reflection data? *Journal of Structural Geology 70*, 141–155.

Reiners, P. W. and M. T. Brandon (2006). Using thermochronology to understand orogenic erosion. *Annu. Rev. Earth Planet. Sci. 34*, 419–466.

Reusch, H. (1901). Nogle bidrag til forstaaelsen af, hvorledes norges dale og fjelde er blevne til.

Roberts, D. (2003). The scandinavian caledonides: event chronology, palaeogeographic settings and likely modern analogues. *Tectonophysics 365*(1-4), 283–299.

Roberts, N. M. W. and T. Slagstad (2014). Continental growth and reworking on the edge of the columbia and rodinia supercontinents; 1.86–0.9 ga accretionary orogeny in southwest fennoscandia. *International Geology Review 57*(11-12), 1582–1606.

Roebben, G., M. Derbyshire, C. Ingelbrecht, and A. Lamberty (2006). Certification of uranium mass fraction in irmm-540r and irmm-541 uranium-doped oxide glasses.

Røhr, T. S., B. Bingen, P. Robinson, and S. M. Reddy (2013). Geochronology of paleoproterozoic augen gneisses in the western gneiss region, norway: evidence for sveconorwegian zircon neocrystallization and caledonian zircon deformation. *The Journal of Geology 121*(2), 105–128.

Rohrman, M., P. van der Beek, and P. Andriessen (1994). Syn-rift thermal structure and post-rift evolution of the oslo rift (southeast norway): New constraints from fission track thermochronology. *Earth and Planetary Science Letters 127*(1-4), 39–54.

Rohrman, M., P. Van Der Beek, P. Andriessen, and S. Cloetingh (1995). Meso-cenozoic morphotectonic evolution of southern norway: Neogene domal uplift inferred from apatite fission track thermochronology. *Tectonics 14*(3), 704–718.

Schiffer, C. and S. B. Nielsen (2016). Implications for anomalous mantle pressure and dynamic topography from lithospheric stress patterns in the north atlantic realm. *Journal of Geodynamics 98*, 53–69.

Schildgen, T. F. and P. A. van der Beek (2019). The application of low-temperature thermochronology to the geomorphology of orogenic systems. In *Fission-Track Thermochronology and its Application to Geology*, pp. 335–350. Springer.

Silk, E. and R. Barnes (1959). Examination of fission fragment tracks with an electron microscope. *Philosophical Magazine 4*(44), 970–972.

Sirevaag, H., J. Jacobs, and A. K. Ksienzyk (in review). Glacial erosion estimates for the dronning maud land mts. (east antarctica) from low-t thermochronology.

Skår, Ø. and R. B. Pedersen (2003). Relations between granitoid magmatism and migmatization: U–pb geochronological evidence from the western gneiss complex, norway. *Journal of the Geological Society 160*(6), 935–946.

Sobel, E. R. and D. Seward (2010). Influence of etching conditions on apatite fission-track etch pit diameter. *Chemical Geology 271*(1-2), 59–69.

Solheim, A., F. Riis, A. Elverhoi, J. Faleide, L. Jensen, and S. Cloetingh (1996). Impact of glaciations on basin evolution and models for the norwegian margin and adjacent areas. *Global and Planetary Change 12*, 1–450.

Sømme, T. O., O. J. Martinsen, and I. Lunt (2013). Linking offshore stratigraphy to onshore paleotopography: The late jurassic–paleocene evolution of the south norwegian margin. *Bulletin 125*(7-8), 1164–1186.

Soper, N., R. Strachan, R. Holdsworth, R. Gayer, and R. Greiling (1992). Sinistral transpression and the silurian closure of iapetus. *Journal of the Geological Society 149*(6), 871–880.

Spiegel, C., B. Kohn, A. Raza, T. Rainer, and A. Gleadow (2007). The effect of long-term low-temperature exposure on apatite fission track stability: A natural annealing experiment in the deep ocean. *Geochimica et Cosmochimica Acta 71*(18), 4512–4537.

Srivastava, S. and C. Tapscott (1986). Plate kinematics of the north atlantic. *The Geology of North America 1000*, 379–404.

SSB.no. Statistisk sentralbyrå: Population and land area in urban settlements. https://www.ssb.no/en/befolkning/folketall/statistikk/tettsteders-befolkning-og-areal. Last checked: 29.07.2021.

Steer, P., R. S. Huismans, P. G. Valla, S. Gac, and F. Herman (2012). Bimodal plio–quaternary glacial erosion of fjords and low-relief surfaces in scandinavia. *Nature Geoscience 5*(9), 635–639.

Steiger, R. H. and E. Jäger (1977). Subcommission on geochronology: convention on the use of decay constants in geo-and cosmochronology. *Earth and planetary science letters 36*(3), 359–362.

Stein, R. (2019). The late mesozoic-cenozoic arctic ocean climate and sea ice history: A challenge for past and future scientific ocean drilling. *Paleoceanography and Paleoclimatology 34*(12), 1851–1894.

Steven, T. A., H. H. Mehnert, and J. D. Obradovich (1967). Juan mountains, colorado. *US Geological Survey Professional Paper*, 47.

Stüwe, K. (2007). Energetics: Heat and temperature. *Geodynamics of the Lithosphere: An Introduction*, 51–137.

Summerfield, M. A. and R. W. Brown (1998). *Geomorphic factors in the interpretation of fission-track data*, pp. 269–284. Springer.

Tagami, T. (2012). Thermochronological investigation of fault zones. *Tectonophysics 538*, 67–85.

Tamer, M. and R. Ketcham (2020). Is low-temperature fission-track annealing in apatite a thermally controlled process? *Geochemistry, Geophysics, Geosystems 21*(3), e2019GC008877.

Torsvik, T., B. Sturt, E. Swensson, T. Andersen, and J. Dewey (1992). Palaeomagnetic dating of fault rocks: evidence for permian and mesozoic movements and brittle deformation along the extensional dalsfjord fault, western norway. *Geophysical Journal International 109*(3), 565–580.

Torsvik, T. H. (2003). The rodinia jigsaw puzzle. *Science 300*(5624), 1379–1381.

Torsvik, T. H. and L. R. M. Cocks (2005). Norway in space and time: a centennial cavalcade. *Norwegian Journal of Geology/Norsk Geologisk Forening 85*.

Ventura, B. and F. Lisker (2003). Long-term landscape evolution of the northeastern margin of the bohemian massif: apatite fission-track data from the erzgebirge (germany). *International Journal of Earth Sciences 92*(5), 691–700.

Vermeesch, P. (2019). *Statistics for fission-track thermochronology*, pp. 109–122. Springer.

Vineyard, G. (1976). Thermal spikes and activated processes. *Radiation effects 29*(4), 245–248.

Wagner, Ga; Storzer, D. (1975). Spaltspuren und ihre bedeutung für die thermische geschichte des odenwaldes. *Aufschluss 27*, 79–85.

Wagner, G. (1968). Fission track dating of apatites. *Earth and Planetary Science Letters 4*(5), 411–415.

Wagner, G. (1972). Geological interpretation of fission track ages.

Wagner, G. and G. Reimer (1972). Fission track tectonics: the tectonic interpretation of fission track apatite ages. *Earth and Planetary Science Letters 14*(2), 263–268.

Wagner, G. and P. Van Den Haute (1992). *Fission-track dating*, Volume 6. Springer Science and Business Media.

Walsh, E. O., B. R. Hacker, P. B. Gans, M. S. Wong, and T. B. Andersen (2013). Crustal exhumation of the western gneiss region uhp terrane, norway: 40ar/39ar thermochronology and fault-slip analysis. *Tectonophysics 608*, 1159–1179.

Wendt, A. S., O. Vidal, and L. T. Chadderton (2002). Experimental evidence for the pressure dependence of fission track annealing in apatite. *Earth and Planetary Science Letters 201*(3-4), 593–607.

Wiest, J. D., H. Fossen, and J. Jacobs (2020). Shear zone evolution during core complex exhumation – implications for continental detachments. *Journal of Structural Geology 140*.

Wiest, J. D., J. Jacobs, H. Fossen, M. Ganerød, and P. T. Osmundsen (2021). Segmentation of the caledonian orogenic infrastructure and exhumation of the western gneiss region during transtensional collapse. *Journal of the Geological Society 178*(3).

Wildman, M., N. Cogné, and R. Beucher (2019). Fission-track thermochronology applied to the evolution of passive continental margins. In *Fission-track thermochronology and its application to geology*, pp. 351–371. Springer.

Wolf, R., K. Farley, and D. Kass (1998). Modeling of the temperature sensitivity of the apatite (u–th)/he thermochronometer. *Chemical Geology 148*(1-2), 105–114.

Young, D. J., B. R. Hacker, T. B. Andersen, and P. B. Gans (2011). Structure and40ar/39ar thermochronology of an ultrahigh-pressure transition in western norway. *Journal of the Geological Society 168*(4), 887–898.

Young, E., A. Myers, E. L. Munson, and N. M. Conklin (1969). *Geological survey research 1969*, pp. 84.

Zanchetta, S., M. G. Malusà, and A. Zanchi (2015). Precollisional development and cenozoic evolution of the southalpine retrobelt (european alps). *Lithosphere 7*(6), 662–681.

Zhang, S., Z.-X. Li, D. A. D. Evans, H. Wu, H. Li, and J. Dong (2012). Pre-rodinia supercontinent nuna shaping up: A global synthesis with new paleomagnetic results from north china. *Earth and Planetary Science Letters 353-354*, 145–155.

Appendix A

Counting Results

Every counting result and additional comments are enclosed in the following pages:

Values in column "Eq. 3.5" show the results of the in-sum term in equation 3.5 that give the value for χ^2 and its (n-1) distribution (p-value).

Position	NoB-029	HeFTy RhoD (N/cm^2)	TrackKey RhoD ($10^5 N/cm^2$)
1	IRMM 1-1	1.72E+06	17.2077
2	VAH_01	1.71E+06	17.1280
3	VAH_02	1.70E+06	17.0484
4	VAH_03	1.70E+06	16.9687
5	VAH_04	1.69E+06	16.8890
6	VAH_05	1.68E+06	16.8093
7	VAH_06	1.67E+06	16.7296
8	VAH_07	1.66E+06	16.6499
9	VAH_08	1.66E+06	16.5702
10	VAH_09	1.65E+06	16.4905
11	VAH_10	1.64E+06	16.4108
12	VAH_11	1.63E+06	16.3311
13	IRMM 1-2	1.63E+06	16.2514
14	VAH_12	1.62E+06	16.1717
15	VAH_13	1.61E+06	16.0920
16	VAH_14	1.60E+06	16.0123
17	VAH_15	1.59E+06	15.9327
18	DUR	1.59E+06	15.8530
19	FCT	1.58E+06	15.7733
20	FCT 2	1.57E+06	15.6936
21	VAH_16	1.56E+06	15.6139
22	VAH_17	1.55E+06	15.5342
23	VAH_18	1.55E+06	15.4545
24	VAH_19	1.54E+06	15.3748
25	IRMM 1-3	1.53E+06	15.2951
26	DUR A1	1.52E+06	15.2154
27	DUR A2	1.51E+06	15.1357
28	DUR A3	1.51E+06	15.0560
29	194	1.50E+06	14.9763
30	195	1.49E+06	14.8966
31	196	1.48E+06	14.8169
32	197	1.47E+06	14.7373
33	198	1.47E+06	14.6576
34	199	1.46E+06	14.5779
35	211	1.45E+06	14.4982
36	215	1.44E+06	14.4185
37	IRMM 1-4	1.43E+06	14.3388

Sample#: **NoB-29**

Irradiation:	Durango	MINERAL	Apatite
Mag.	1,25		
RhoD			
Date	03.11.2020		
Analyst	FMU		

#		Ns	Ni	L	B	Area
1		14	121	10	10	100
2		15	117	10	10	100
3		15	106	10	10	100
4		15	96	10	10	100
5		13	97	10	10	100
6		19	123	10	10	100
7		17	86	10	10	100
8		15	105	10	10	100
9		16	77	10	10	100
10		15	121	10	10	100
11		18	79	10	10	100
12		17	72	10	10	100
13		14	100	10	10	100
14		12	109	10	10	100
15		14	98	10	10	100
16		18	83	10	10	100
17		16	114	10	10	100
18		10	77	10	10	100
19		16	91	10	10	100
20		16	83	10	10	100
21		10	92	10	10	100
22		15	88	10	10	100
23		12	113	10	10	100
24						
25						
26						
27						
28						
29						
30						

			Ns/Ni	Zeta	1x st. Dev.	2x st. Dev.
Sum	342	2248	0.1521	261.08	15.8	15.24
Averag	14.9	97.7				
σ	2.34	15.8				
σ %	15.7	16.1				
Max	19	123				
Min	10	72				

Sample#: **NoB-29**

Irradiation: FCT1 MINERAL Apatite
Mag. 1,25
RhoD
Date 03.11.2020
Analyst FMU

#		Ns	Ni	L	B	Area
1		6	45	10	5	50
2		9	47	5	10	50
3		9	28	5	10	50
4		5	40	10	5	50
5		5	26	5	5	25
6		2	13	5	5	25
7		3	15	5	5	25
8		4	25	5	5	25
9		2	28	5	5	25
10		1	14	5	5	25
11		4	27	5	5	25
12		3	28	5	5	25
13		2	17	5	5	25
14		4	31	5	10	50
15		4	18	5	5	25
16		4	24	5	5	25
17		2	14	5	5	25
18		5	26	5	5	25
19		3	21	5	5	25
20		3	20	5	5	25
21						0
22						0
23						0
24						
25						
26						
27						
28						
29						
30						

			Ns/Ni	Zeta	1x st. Dev.	2x st. Dev.
Sum	80	507	0.1578	224.67	27.36	27.06
Averag	4	25.4				
σ	2.13	9.78				
σ %	53.2	38.6				
Max	9	47				
Min	1	13				

Sample#: **NoB-29**

Irradiation: FCT2 MINERAL Apatite
Mag. 1,25
RhoD
Date 04.11.2020
Analyst FMU

#		Ns	Ni	L	B	Area
1		6	29	5	5	25
2		4	39	5	10	50
3		3	20	5	5	25
4		7	41	5	5	25
5		12	41	10	5	50
6		5	24	5	5	25
7		12	43	10	5	50
8		6	42	5	10	50
9		9	38	5	5	25
10		3	21	5	5	25
11		6	29	5	10	50
12		7	42	10	5	50
13		5	54	5	10	50
14		6	44	10	5	50
15		8	52	10	10	100
16		10	96	10	10	100
17		2	17	5	5	25
18		5	43	5	10	50
19		1	22	5	5	25
20		4	17	5	5	25
21						0
22						0
23						0
24						
25						
26						
27						
28						
29						
30						

			Ns/Ni	Zeta	1x st. Dev.	2x st. Dev.
Sum	121	754	0.1605	225.81	22.53	22.16
Averag	6.05	37.7				
σ	3.02	17.9				
σ %	49.9	47.4				
Max	12	96				
Min	1	17				

Sample#: **VAH-01**

											Sum	1402	1762
Irradiation:	NoB-29				MINERAL	Apatite						
Mag.	1,25										**Average**	70.1	88.1
RhoD											**σ**	30.9921892	45.6472747
Date	24.11.2020										**σ %**	44.2113968	51.8130246
Analyst	FMU												
		Ns/Ni	**FT-age**	**1x st. Dev.**	**2x st. Dev.**	**n(G)**							
		0.7957				20					**Max**	152	201
											Min	24	32

#	cT	Ns	Ni	L	B	Area	Grain qualit	comments		Eq. 5.3
1		24	32	5	10	50	p	f		118496
2		92	133	10	10	100	g			2637809.08
3		70	70	10	5	50	f	f		4536000
4		51	60	5	10	50	g	z		297032.108
5		77	104	10	10	100	f	f		567392.022
6		52	74	5	10	50	f	f		1166598.22
7		41	62	10	10	100	g	f d	adjacent to Zrc	2092826.45
8		63	61	5	10	50	f	f		5237373.03
9		38	50	10	5	50	f	i		112326.545
10		31	51	5	10	50	g	f		3474809.76
11		58	52	10	5	50	f	f d		7800193.31
12	*	104	131	10	10	100	g	f d		729.344681
13		70	74	5	10	50	f	f i		2665600.44
14		89	132	10	10	100	g	f i d		3610119.98
15		60	58	5	10	50	f	z f		5047078.1
16		86	86	10	10	100	gr	wz		5572800
17		50	42	10	5	50	g	f	adjacent to zrc	9277985.39
18		76	120	10	10	100	g	f i	adjacent to zrc	6012304
19	*	152	201	10	10	100	p	f		553497.122
20		118	169	10	10	100	p	f i		2934761.27
21						0				
22						0				
23						0			χ^2=	25.7924597
24						0				
25						0			p-value	0.1361
26						0				
27						0				
28						0				
29						0				
30						0				
31						0				
32						0				
33						0				
34										
35										
36										
37										
38										
39										
40										

fractures	16
dislocations	4
inclusions	5
wzonation	1
zonations	2

Sample#: **VAH-02**

											Sum	3000	4166
Irradiation:	NoB-29				MINERAL	Apatite						
Mag.	1,25										**Average**	119.285714	162.857143
RhoD											**σ**	57.7140735	90.5981709
Date	24.11.2020										**σ %**	48.3830557	55.6304558
Analyst	FMU												
							Ns/Ni	**FT-age**	**1x st. Dev.**	**2x st. Dev.**	**n(G)**		
							0.7201				24		
												Max	251	403
												Min	40	49

#	cT	Ns	Ni	L	B	Area	Grain qualit	comments		Eq. 5.3
1		69	80	5	10	50	g	f i z		15113302.8
2	*	129	158	10	5	50	p		obstacle on mica	14011621.6
3	*	217	323	10	10	100	f	f		7818778.67
4		40	56	5	5	25	f	wz f i		19266.6667
5		103	126	5	10	50	f	f		11401771.2
6		96	111	5	10	50	f			21644580.2
7		71	84	10	10	100	g	d		12369121.3
8		148	183	10	10	100	g	i		13792853.8
9		103	174	5	10	50	g	f i		31158056.3
10		43	49	5	5	25	p	f		11226641.8
11		82	102	10	5	50	f	i f		6892470.35
12		93	149	10	10	100	g	f		14659635.7
13		71	98	10	10	100	g	wz		18874.5325
14		181	233	10	10	100	gr			7318990.62
15		72	104	5	10	50	f	f		824740.364
16		158	236	10	10	100	g	f		6287441.58
17		129	182	10	10	100	g			237039.859
18	*	251	403	10	10	100	g	f		40792042.1
19		148	180	10	10	100	f			17873959.2
20		96	110	10	5	50	g	d		23742932.5
21		205	279	10	10	100	g	f		599216.736
22		160	192	10	10	100	g	f d		23298618.2
23		106	180	10	10	100	g	f		33857857.4
24		229	374	10	5	50	g			46798169.5
25										
26										
27										
28										
29										χ^2= 28.9452699
30										
31									p-value	0.1821
32										
33										
34										
35										
36										
37										
38										
39										
40										

fractures	14
dislocations	3
inclusions	5
wzonation	2
zonations	1

Sample#: **VAH-03**

Irradiation: NoB-29 MINERAL Apatite
Mag. 1,25
RhoD
Date 04.11.2020
Analyst FMU

Ns/Ni	FT-age	1x st. Dev.	2x st. Dev.	n(G)
1.0299				20

	Ns	Ni
Sum	483	469
Average	24.625	23.3125
σ	11.0204356	9.14125265
σ %	44.7530378	39.2118076
Max	49	43
Min	11	8

#	cT	Ns	Ni	L	B	Area	Grain qualit	comments		Eq. 5.3
1		13	20	5	5	25	f	fz		384696.03
2		11	8	5	5	25	p	fwz		88264.4737
3		24	26	5	10	50	f	f		33904.08
4		14	18	5	10	50	p	f		141512
5		26	13	10	10	100	f	fd		897108.333
6		27	17	10	10	100	g			450461.455
7		28	19	10	10	100	g	f		332809.043
8		28	29	10	10	100	g			13432.0175
9		17	18	10	10	100	g	f	next to a zrc	14852.6
10		32	26	10	10	100	g	f		103491.379
11		12	14	10	10	100	f	id		49459.8462
12		29	26	10	10	100	f	f		19779.0727
13		21	32	10	10	100	g	f		593178.283
14		45	43	5	10	50	g			1282.90909
15		18	28	10	10	100	g	fi		561450.522
16		49	36	10	10	100	g			368019.4
17		39	42	10	10	100	g	f		49136.1111
18		17	9	10	5	50	f	f		505687.538
19		22	30	5	5	25	g	fz		334722.769
20		11	15	5	5	25	f	fz		167361.385
21										
22										
23										
24										
25									χ^2=	22.5607069
26										
27									p-value	0.2572
28										
29										
30										
31										
32										
33										
34										
35										
36										
37										
38										
39										
40										

fractures	15
dislocations	2
inclusions	2
wzonation	1
zonations	3

Sample#: **VAH-04**

											Sum	577	691
Irradiation:	NoB-29				MINERAL	Apatite							
Mag.	1,25										**Average**	26.7647059	31.4117647
RhoD											**σ**	13.1791948	20.6096422
Date	05.11.2020										**σ %**	49.2409477	65.6112206
Analyst	FMU												
											Max	56	85
											Min	8	6

Ns/Ni	**FT-age**	**1x st. Dev.**	**2x st. Dev.**	**n(G)**
0.835				21

#	cT	Ns	Ni	L	B	Area	Grain qualit	comments	Eq. 5.3
1		40	36	10	10	100	f	fi	620650.316
2		16	16	10	10	100	f		103968
3		35	37	10	10	100	f	fi	111706.889
4		23	28	10	10	100	g	fi	1356.2549
5		15	12	10	10	100	g	fi	438536.333
6		8	6	5	5	25	f	fi	304882.571
7		41	53	10	10	100	f	fi	53856.383
8		33	52	10	10	100	f	i	610051.776
9		47	53	10	10	100	f	fi	35948.16
10		56	85	10	10	100	g	i	759587.241
11		20	6	5	5	25	g	fiwz	4126467.85
12		27	32	5	5	25	f		631.338983
13		23	36	5	10	50	p	fi wz	403468.492
14		16	12	10	10	100	f		609765.143
15		22	23	10	10	100	g	fi	82861.3556
16		16	22	10	5	50	g	if	70606.4211
17		17	25	5	10	50	g	f	170754.381
18		41	71	10	10	100	f	f	1425611.57
19		23	21	10	10	100	g	f	324049.455
20		32	36	10	5	50	f	fz	26405.8824
21		26	29	5	5	25	f	zf	27641.6182
22									
23									
24									
25									
26									
27									χ^2= 25.8555968
28									
29									p-value 0.1706
30									
31									
32									
33									
34									
35									
36									
37									
38									
39									
40									

fractures	16
dislocations	0
inclusions	13
wzonation	2
zonations	2

Sample#: **VAH-05**

											Sum	1275	1749
Irradiation:	NoB-29				MINERAL	Apatite							
Mag.	1,25										**Average**	54.1428571	74.2857143
RhoD											**σ**	26.0197727	33.2718242
Date	06.11.2020										**σ %**	48.0576277	44.7889941
Analyst	FMU												
					Ns/Ni	**FT-age**	**1x st. Dev.**	**2x st. Dev.**	**n(G)**		**Max**	129	147
					0.729				24		**Min**	22	17

#	cT	Ns	Ni	L	B	Area	Grain qualit	comments		Eq. 5.3
1		22	17	5	5	25	g	zf		7239507.92
2		37	52	10	5	50	g	fz		28298.5281
3		64	85	10	10	100	g	f		85105.5101
4		54	78	5	10	50	p	fid		189697.091
5		75	95	5	10	50	f			594132.353
6		41	58	10	10	100	g			50728.0909
7		42	66	10	10	100	g	f		1058508
8		57	61	10	10	100	f	f		4071175.63
9		84	115	10	10	100	g			425.532663
10		58	80	10	10	100	g			2256.26087
11		27	28	5	10	50	f	f		2414173.25
12		37	60	10	10	100	g			1432302.77
13		99	147	10	10	100	g			828240.146
14		33	61	10	10	100	g	fi		4280035.79
15		49	53	10	10	100	g	f		3221096.82
16		69	120	5	10	50	f	wz fd		5526549
17		52	70	10	10	100	g	f		23632.8197
18	*	129	129	10	10	100	f	ifd		14491602
19		37	73	10	5	50	g			7312754.95
20		28	28	10	10	100	g			3145464
21		43	84	10	10	100	g	f		8009161.02
22		58	67	5	10	50	f			2052354.31
23		34	56	5	5	25	f			1582448.4
24		46	66	5	5	25	f	fz		121968
25						0				
26						0				
27						0			χ^2=	30.3867165
28						0				
29						0			p-value	0.1386
30						0				
31						0				
32						0				
33						0				
34						0				
35						0				
36						0				
37						0				
38						0				
39						0				
40						0				

fractures	14
dislocations	3
inclusions	3
wzonation	1
zonations	3

Sample#: **VAH-06**

											Sum	901	1121
Irradiation:	NoB-29				MINERAL	Apatite							
Mag.	1,25										**Average**	27.5882353	36.5882353
RhoD											**σ**	10.845845	19.2810102
Date	07.11.2020										**σ %**	39.3132973	52.6972947
Analyst	FMU												
		Ns/Ni	**FT-age**	**1x st. Dev.**	**2x st. Dev.**	**n(G)**					**Max**	44	75
		0.8037				27					**Min**	10	11

#	cT	Ns	Ni	L	B	Area	Grain qualit	comments		Eq. 5.3
1		20	22	5	5	25	g	df		160704.857
2		40	52	10	10	100	g			44001.5652
3		21	24	10	5	50	g	f		81664.2
4		31	22	5	5	25	f	f		4205189.45
5		40	62	5	10	50	g			1191024.35
6		42	47	10	10	100	g	i		251912.64
7		23	32	10	10	100	g	f		169025.473
8		23	20	5	10	50	g	f		1401492.3
9		44	75	10	10	100	g			2799151.27
10		41	72	10	10	100	f	if		3164831.16
11		31	25	10	5	50	g	f		2669197.79
12		25	32	5	10	50	g	if		11425.4211
13		30	47	5	10	50	f	f		986832.325
14		13	22	5	5	25	f	d wz		787200.029
15		20	35	5	10	50	g			1510604.09
16		10	22	5	5	25	g	fz		2317704.5
17		15	11	5	5	25	g	f wz		1833277.54
18		21	22	5	10	50	g	f	'weirdly zoned'	321650.256
19		14	28	10	10	100	g	fd		2164218
20		51	56	10	10	100	gr	i		421413.318
21		37	50	5	10	50	g			146739.414
22		56	60	10	10	100	g	f		654902.207
23		33	32	10	10	100	g	f		1024644.94
24		25	20	5	5	25	g	f		2224445
25		24	31	10	10	100	g	f		19176.8909
26		57	52	10	10	100	g	f		2665431.42
27		114	148	10	10	100	gr	f		117736.321
28						0				
29						0				
30						0				
31						0				
32						0			χ^2=	33.0147559
33						0				
34						0			p-value	0.1617
35						0				
36						0				
37						0				
38						0				
39						0				
40						0				
41						0				
42						0				
43						0				
44						0				

fractures	17
dislocations	3
inclusions	4
wzonation	2
zonations	1

Sample#: **VAH-07**

										Sum	910	1341
Irradiation:	NoB-29			MINERAL	Apatite						
Mag.	1,25									**Average**	43.3684211	63.3157895
RhoD										**σ**	17.4617376	27.9564197
Date	10.11.2020									**σ %**	40.2637154	44.1539464
Analyst	FMU											
										Max	81	125
										Min	23	24

Ns/Ni	**FT-age**	**1x st. Dev.**	**2x st. Dev.**	**n(G)**
0.6786				21

#	cT	Ns	Ni	L	B	Area	Grain qualit	comments		Eq. 5.3
1		81	125	10	10	100	g			127702.141
2		74	72	10	10	100	g			7785162.99
3		29	39	5	10	50	g	fd		169900.015
4		43	48	10	10	100	f	fi		2148618.56
5		29	54	10	5	50	g	f		1266060.25
6		55	90	5	10	50	g	f wz		457524.31
7		63	111	10	10	100	g		close to an inclusion	1569780.05
8		23	24	5	10	50	g			1724553.38
9		32	64	10	5	50	g			2447370.67
10		31	51	10	10	100	g	f		285560.012
11		31	38	10	5	50	g	f		708320.014
12		57	93	10	10	100	f	f		447501.66
13		36	75	10	5	50	g	wz		3594240.32
14		66	82	10	10	100	g	id		1302844.57
15		37	33	5	10	50	g	idf		5480722.41
16		23	26	5	5	25	g	fi wz		1052969.16
17		34	61	10	5	50	g	f		1035021.64
18		36	48	10	5	50	g	f wz		251466.857
19		44	69	10	10	100	f	f		126847.752
20		36	44	10	5	50	g			847896.2
21		50	94	10	10	100	g	fi		2374167.36
22						0				
23						0				
24						0				
25						0				
26						0			χ^2=	28.8485961
27						0				
28						0			p-value	0.09
29						0				
30						0				
31						0				
32						0				
33						0				
34										
35										
36										
37										
38										
39										
40										

fractures	13
dislocations	3
inclusions	5
wzonation	4
zonations	0

Sample#: **VAH-08**

Irradiation:	NoB-29		MINERAL	Apatite	
Mag.	1,25				
RhoD					
Date	11.11.2020				
Analyst	FMU				

Ns/Ni	FT-age	1x st. Dev.	2x st. Dev.	n(G)
1.0033				20

Sum	1216	1212
Average	60.8	60.6
σ	28.6954975	35.2978306
σ %	47.196542	58.2472451
Max	114	124
Min	14	11

#	cT	Ns	Ni	L	B	Area	Grain qualit	comments	Eq. 5.3
1		24	15	5	5	25	g	fdz	3017412.92
2		58	46	10	10	100	g	f wz	1982784.62
3	*	76	99	10	10	100	p	fdi	4567462.77
4		112	117	10	10	100	f	i	186090.76
5		54	42	10	10	100	g	fdi	2152806
6		114	124	10	10	100	f	zf	668754.017
7		50	45	10	5	50	p		363941.053
8		90	104	10	10	100	g	d	1557749.77
9		84	109	10	10	100	g	id wz	4894827.44
10		54	51	10	5	50	gr	zd	112177.371
11		50	35	5	5	25	g	f	3828724.71
12		38	42	5	10	50	f	df	314503.2
13		14	11	5	5	25	p	ifd	516098.56
14		26	29	5	5	25	f	fdi	255954.618
15		80	82	10	10	100	f	fd	46750.0247
16		45	31	5	5	25	g	fz	3733162.32
17		44	48	10	5	50	g	z	276104.348
18		74	69	10	5	50	g	zfi	233948.643
19		95	86	10	10	100	g	id	616564.066
20		34	27	5	5	25	f	z	1150120.92
21						0			
22						0			
23						0			
24						0			
25						0			χ^2= 20.6785884
26						0			
27						0			p-value 0.3548
28						0			
29						0			
30						0			
31						0			
32						0			
33						0			
34									
35									
36									
37									
38									
39									
40									

fractures	12
dislocations	11
inclusions	8
wzonation	2
zonations	7

Sample#: **VAH-09**

										Sum	1140	1295
Irradiation:	NoB-29				MINERAL	Apatite						
Mag.	1,25									**Average**	60.5294118	67.5882353
RhoD										**σ**	29.7197696	36.2457908
Date	11.11.2020									**σ %**	49.0997166	53.6273668
Analyst	FMU											
					Ns/Ni	**FT-age**	**1x st. Dev.**	**2x st. Dev.**	**n(G)**	**Max**	135	141
					0.8803				20	**Min**	21	23

#	cT	Ns	Ni	L	B	Area	Grain qualit	comments	Eq. 5.3
1		37	41	5	5	25	p	fi wz	17700.3205
2		78	86	10	10	100	f	fd	53785.9756
3		56	70	10	5	50	g	f	420622.222
4		108	140	5	10	50	g	f wz	1571240.32
5		21	23	5	5	25	g	fi wz	21605.1136
6		63	55	10	5	50	p	wz	3022400.21
7		72	99	10	5	50	f	wz	2251136.84
8		35	34	5	5	25	g	f wz	624626.449
9		87	72	10	10	100	g	fi	5883284.43
10		30	28	10	5	50	f		828015.517
11		74	102	10	10	100	g		2376150.57
12		56	47	10	5	50	g	f	3482753.4
13		43	52	5	10	50	g	fd	136042.368
14	*	51	71	10	10	100	g	fd	1818532.99
15		135	141	10	10	100	f	f	718794.293
16		33	28	10	10	100	g	fi	1917446.31
17		50	60	10	5	50	f	z	121113.636
18		23	29	5	5	25	f	wz	206262.019
19		53	73	10	10	100	g		1688271.63
20		35	44	5	10	50	f	fi	295914.241
21									
22									
23									
24									χ^2= 18.597642
25									
26									p-value 0.4829
27									
28									
29									
30									
31									
32									
33									
34									
35									
36									
37									
38									
39									
40									

fractures	13
dislocations	3
inclusions	5
wzonation	7
zonations	1

Sample#: **VAH-10**

Irradiation:	NoB-29		MINERAL	Apatite	
Mag.	1,25				
RhoD					
Date	12.11.2020				
Analyst	FMU				

Ns/Ni	FT-age	1x st. Dev.	2x st. Dev.	n(G)
1.0376				20

Sum	331	319
Average	16.55	15.95
σ	6.53311403	10.0024997
σ %	39.4750093	62.7115968
Max	32	49
Min	9	4

#	cT	Ns	Ni	L	B	Area	Grain qualit	comments	Eq. 5.3
1		11	7	5	5	25	p	fiz	78936.8889
2		15	21	10	10	100	p	fi	130321
3		9	9	10	5	50	g	fz	648
4		19	17	10	5	50	g	f	5232.11111
5		30	16	10	10	100	p	fdi	397110.348
6		18	15	10	5	50	f	zi	18294.8182
7		15	14	10	10	100	g		786.241379
8		12	10	5	10	50	g	dfz	12196.5455
9		12	8	5	5	25	f	i	69620
10		15	22	10	10	100	g	di	168513.757
11		19	18	5	10	50	f	f	286.72973
12		10	8	5	5	25	f	zf	16320.2222
13	*	13	15	10	5	50	f	wz fd	23897.2857
14		27	49	5	10	50	p	fid	761200.474
15		9	4	5	5	25	f	wz	184093
16		13	11	5	5	25	f	z	10668.1667
17		19	14	10	5	50	p	zfi	61706.9394
18		16	12	10	5	50	p	fiwz	45765.1429
19		17	17	5	10	50	f	wz f i	1224
20		32	32	5	10	50	p	f z i d	2304
21						0			
22						0			
23						0			
24						0			χ^2= 18.8383797
25						0			
26						0			p-value 0.4672
27						0			
28						0			
29						0			
30						0			
31						0			
32						0			
33						0			
34									
35									
36									
37									
38									
39									
40									

fractures	14
dislocations	6
inclusions	11
wzonation	4
zonations	8

Sample#: **VAH-11**

Irradiation: NoB-29 MINERAL Apatite
Mag. 1,25
RhoD
Date 04.11.2020
Analyst FMU

Ns/Ni	FT-age	1x st. Dev.	2x st. Dev.	n(G)
0.9193				26

Sum	1926	2095
Average	75.2631579	84.0526316
σ	25.7139005	33.4970541
σ %	34.1653223	39.8524751
Max	139	170
Min	35	19

#	cT	Ns	Ni	L	B	Area	Grain qualit	comments	Eq. 5.3
1		73	89	10	10	100	g		2107860.75
2	*	41	37	10	5	50	g	f wz	2745188.32
3	*	57	87	10	10	100	g	d	16098150.1
4	*	74	85	10	10	100	f		473851.572
5		43	48	10	10	100	g	df wz	61360.0989
6		70	77	10	10	100	p	f	18565.3333
7		102	102	10	10	100	p	d	1456611
8		73	68	10	10	100	g	d	3422333.96
9		57	71	10	10	100	g	f	2346590.32
10		139	170	10	10	100	f	d	4244421.44
11		35	19	5	5	25	f	fz	24984562.2
12		82	104	10	10	100	f	fd	4371226.86
13		115	129	10	10	100	g	f	232319.02
14		75	88	10	10	100	g	d	937691.834
15	*	92	116	10	10	100	f	d wz	4524120.08
16		79	77	10	10	100	f	d	1897071.85
17		89	96	10	10	100	p	wz f	13137.7351
18	*	54	68	10	10	100	f	wz fd	2608149.54
19		80	66	10	10	100	f	df	11225714.1
20		81	61	10	10	100	p	d	19195631.6
21		79	93	10	10	100	f	d	1077405.63
22		66	60	10	10	100	p	di	4093207.14
23		60	66	10	10	100	f	d wz	15913.1429
24		81	90	10	10	100	g	f	77696.0526
25		66	54	10	10	100	f	f wz	9784656.3
26		63	74	10	10	100	g	d	810733.73
27						0			
28						0			
29						0			
30						0			
31						0			
32						0			
33						0			
34						0			
35						0			
36						0			
37						0			
38						0			
39						0			
40						0			

χ^2= 29.4485881

p-value 0.2456

fractures	12
dislocations	16
inclusions	1
wzonation	7
zonations	1

Sample#: **VAH-12**

											Sum	887	657
Irradiation:	NoB-29				MINERAL	Apatite							
Mag.	1,25										**Average**	44.35	32.85
RhoD											**σ**	24.9489479	23.113621
Date	16.11.2020										**σ %**	56.2546739	70.3610988
Analyst	FMU												
		Ns/Ni	**FT-age**	**1x st. Dev.**	**2x st. Dev.**	**n(G)**					**Max**	114	103
		1.3501				20					**Min**	14	15

#	cT	Ns	Ni	L	B	Area	Grain qualit	comments	Eq. 5.3
1	*	114	103	10	10	100	g	fz i	1248987.876
2	*	63	56	10	10	100	g	f i	576260.1765
3		14	15	5	5	25	p	fi	581636.1724
4		34	16	10	5	50	g	z f i	1327146.32
5	*	26	20	5	5	25	p	dfi	9412.26087
6		16	20	5	5	25	f	fiz	1451221.778
7		28	15	5	5	25	p	fid	602750.7209
8		45	25	5	10	50	f	wz f i d	780172.8571
9	*	42	31	10	10	100	g	f	128.890411
10	*	51	30	10	5	50	f	fid	587266.7778
11		34	25	10	5	50	g	fdi	450.3220339
12		90	83	10	5	50	f	fdi wz	1213809.717
13	*	31	29	10	10	100	g	fi	478112.2667
14	*	42	38	10	10	100	f	fi	466956.8
15		71	41	5	10	50	f	fid	943557.1429
16		59	29	5	10	50	f	dfi	1932290.909
17	*	23	20	5	5	25	g	wz fd	160735.8372
18		31	17	5	10	50	g	f	582561.3333
19		43	25	10	5	50	g		542908.4706
20	*	30	19	10	5	50	f	fd	166580.5918
21						0			
22						0			
23						0			
24						0			
25						0			χ^2= 23.42811903
26						0			
27						0			p-value 0.22
28						0			
29						0			
30						0			
31						0			
32						0			
33						0			
34									
35									
36									
37									
38									
39									
40									

fractures	19
dislocations	10
inclusions	15
wzonation	3
zonations	3

Sample#: **VAH-13**

Irradiation:	NoB-29		MINERAL	Apatite	
Mag.	1,25				
RhoD					
Date	16.11.2020				
Analyst	FMU				

Ns/Ni	FT-age	1x st. Dev.	2x st. Dev.	n(G)
1.1396				20

Sum	702	616
Average	34.5625	29.4375
σ	18.9313453	21.2664642
σ %	54.7742358	72.2427659
Max	72	79
Min	10	5

#	cT	Ns	Ni	L	B	Area	Grain qualit	comments	Eq. 5.3
1		23	15	5	5	25	f	dfz	348290.632
2		29	27	10	5	50	p	df	21216.0714
3		20	26	5	5	25	f	zfd	764970.087
4		46	53	5	5	25	g	wz	794716.162
5		17	12	5	5	25	p	fzd	144631.172
6		27	12	5	5	25	p	i wz f	1727468.31
7		23	40	5	5	25	f	wz f	3072122.92
8		35	17	5	10	50	f	fd	1781920.69
9		32	20	5	5	25	f	zd	618684.308
10		66	47	10	10	100	f		519524.283
11		61	63	10	10	100	g	wz	356633.065
12		10	5	10	10	100	g	d	468166.667
13		19	9	5	5	25	f	zi	1036035.57
14		51	28	5	10	50	g	di wz	1750602.53
15	*	72	79	10	10	100	f	d	816842.623
16		22	18	5	5	25	f	z	20976.4
17		37	37	5	5	25	f	fd	136826
18		34	16	5	5	25	f	fdiwz	1886458.88
19		51	58	5	5	25	f	ifdwz	793486.239
20	*	27	34	5	5	25	f	fd	858355.672
21									
22									
23									
24	*								χ^2= 41.4352506
25									
26									p-value 0.0021
27									
28									
29									
30	*								
31									
32									
33									
34									
35									
36									
37									
38									
39									
40									

fractures	11
dislocations	13
inclusions	5
wzonation	7
zonations	6

Sample#: **VAH-14**

											Sum	456	436
Irradiation:	NoB-29				MINERAL	Apatite							
Mag.	1,25										**Average**	22.8	21.8
RhoD											**σ**	11.3675438	15.6628961
Date	17.11.2020										**σ %**	49.8576484	71.8481475
Analyst	FMU												
		Ns/Ni	**FT-age**	**1x st. Dev.**	**2x st. Dev.**	**n(G)**					**Max**	49	65
		1.0459				20					**Min**	9	4

#	cT	Ns	Ni	L	B	Area	Grain qualit	comments		Eq. 5.3
1		10	5	5	5	25	f	di wz		288426.667
2		35	30	10	5	50	f	f		38406.1538
3		11	4	5	5	25	g			588852.267
4		27	25	10	5	50	p	f wz		2661.23077
5		21	17	10	5	50	f	di		51874.1053
6		23	24	10	10	100	p	di		17852.2553
7		30	35	5	10	50	f	f		127606.154
8		15	8	10	5	50	g	i		363637.565
9		15	13	5	5	25	p	zf		13376.5714
10		25	19	5	5	25	f	zf		113629.455
11		10	5	10	10	100	f			288426.667
12		49	50	10	10	100	f	fi		20829.2525
13		16	13	10	10	100	g			37872.5517
14		45	65	10	10	100	g			912730.909
15	*	17	18	5	5	25	f	z		18103.3143
16		9	6	5	5	25	g	z		94089.6
17		29	32	10	10	100	f	fdi		62208.2623
18		27	24	10	5	50	f	fdi wz		13442.8235
19		13	14	5	5	25	f	wz		18987.2593
20		29	29	5	10	50	g	fz		5800
21						0				
22						0				
23						0				
24						0				
25						0			χ^2=	15.4857409
26						0				
27						0			p-value	0.6913
28						0				
29						0				
30						0				
31						0				
32						0				
33						0				
34										
35										
36										
37										
38										
39										
40										

fractures	9
dislocations	5
inclusions	7
wzonation	4
zonations	5

Sample#: **VAH-15**

										Sum	1401	1319
Irradiation:	NoB-29			MINERAL	Apatite						
Mag.	1,25									**Average**	66.7142857	62.8095238
RhoD										**σ**	31.9298338	34.4885764
Date	18.11.2020									**σ %**	47.8605646	54.9097881
Analyst	FMU											
										Max	138	142
										Min	20	17

Ns/Ni	**FT-age**	**1x st. Dev.**	**2x st. Dev.**	**n(G)**
1.0622				21

#	cT	Ns	Ni	L	B	Area	Grain qualit	comments		Eq. 5.3
1		20	17	5	5	25	g	zd		177539.703
2		65	46	10	10	100	f	wzi		4083076.77
3		85	90	10	10	100	g	dfi		1116003.57
4		49	41	10	10	100	g	fd		574401.111
5		37	32	10	5	50	f	zfd		228533.928
6		106	106	10	10	100	g	z		356372
7		24	33	10	5	50	g	z		3727875.95
8		138	142	10	10	100	g	zfd		1022451.43
9		96	95	10	10	100	g	z		219234.77
10		119	119	10	10	100	f	z		400078
11		66	60	10	5	50	f	z	large obstacle on mica	71143.1429
12		87	91	10	10	100	g	zd		911554.18
13		89	84	10	10	100	g	z		496.236994
14		49	34	5	10	50	f	z		3480698.9
15		36	25	5	10	50	f	zf		2544699.69
16		69	65	5	10	50	g	z		21.761194
17		65	58	10	10	100	g	z		162955.52
18		48	51	10	5	50	g	z		669124.455
19		33	35	10	5	50	g	z		446148
20		39	24	10	5	50	g	z		5038817.29
21	*	81	71	10	10	100	gr	zf	picture taken	357154.105
22						0				
23						0				
24						0				
25						0				
26						0				χ^2= 13.8471332
27						0				
28						0				p-value 0.8382
29						0				
30						0				
31						0				
32						0				
33						0				
34										
35										
36										
37										
38										
39										
40										

fractures	6
dislocations	6
inclusions	2
wzonation	1
zonations	18

Sample#: **VAH-16**

											Sum	673	547
Irradiation:	NoB-29					MINERAL	Apatite					
Mag.	1,25										**Average**	56.0833333	45.5833333
RhoD											**σ**	41.4826543	29.181122
Date	18.11.2020										**σ %**	73.9660998	64.0170866
Analyst	FMU												
						Ns/Ni	**FT-age**	**1x st. Dev.**	**2x st. Dev.**	**n(G)**			
						1.2303				12			
											Max	168	107
											Min	14	6

Apatites look terrible, brownish, almost opace...makes them almost impossible to count

#	cT	Ns	Ni	L	B	Area	Grain qualit	comments		Eq. 5.3
1		14	6	10	5	50	f	f		655220
2		60	65	10	5	50	p	fdi		954845
3		43	36	10	5	50	f	fdi		6327.20253
4		33	30	10	5	50	p	df		72624.1429
5		98	91	10	10	100	p	df		308591.37
6		38	33	5	10	50	f	f		28520.1268
7		57	30	10	5	50	p	fdi		1388024.38
8		19	22	5	5	25	p	fd		474989.488
9		54	54	5	10	50	f	z		428652
10		168	107	10	10	100	p	fd		1437866.27
11		54	42	5	5	25	p	fdi		16854
12		35	31	5	5	25	p	difwz		44720.0606
13						0				
14						0				
15						0				
16						0				
17						0			χ^2=	15.802076
18						0				
19						0			p-value	0.1486
20						0				
21						0				
22						0				
23						0				
24						0				
25						0				
26						0				
27						0				
28						0				
29						0				
30						0				
31						0				
32						0				
33						0				
34										
35										
36										
37										
38										
39										
40										

fractures	11
dislocations	9
inclusions	5
wzonation	1
zonations	1

Sample#: **VAH-17**

Irradiation:	NoB-29		MINERAL	Apatite	
Mag.	1,25				
RhoD					
Date	19.11.2020				
Analyst	FMU				

Ns/Ni	FT-age	1x st. Dev.	2x st. Dev.	n(G)
1.1566				21

Sum	842	728
Average	40.0952381	34.6666667
σ	19.0863951	19.9181659
σ %	47.602648	57.4562478
Max	88	88
Min	18	8

#	cT	Ns	Ni	L	B	Area	Grain qualit	comments	Eq. 5.3
1		32	14	5	5	25	f	z.f	2879001.39
2		21	17	5	5	25	f	z	24965.1579
3		25	20	10	10	100	g		41102.2222
4		22	22	5	5	25	f	zfi	142956
5		47	43	10	10	100	f	zfi	44001.1111
6		52	38	10	10	100	g	f	381551.111
7		61	68	10	10	100	g	zi	1279620.96
8		38	37	10	5	50	g	z	162401.333
9		62	44	10	10	100	g	zf	617129.66
10		88	88	10	10	100	g	zdi	571824
11		48	47	10	5	50	g	z	225651.579
12		21	13	5	5	25	f	zf	554498.941
13		38	29	10	5	50	g	zf	157261.433
14		20	23	5	5	25	f	zif	537154.326
15		21	15	5	5	25	g	wzf	196249
16		18	8	5	5	25	f	wz	1559670.15
17		73	61	10	10	100	g	wz	23697.9403
18		35	27	10	5	50	f	zfi	121621.226
19		37	38	10	5	50	g		341381.333
20		35	35	5	10	50	f	fi	227430
21		48	41	10	5	50	f	df	2000.94382
22									
23									
24									
25									χ^2= 16.4625855
26									
27									p-value 0.6875
28									
29									
30									
31									
32									
33									
34									
35									
36									
37									
38									
39									
40									

fractures	12
dislocations	2
inclusions	7
wzonation	3
zonations	13

Sample#: **VAH-18**

											Sum	1386	1200
Irradiation:	NoB-29				MINERAL	Apatite							
Mag.	1,25										**Average**	66	57.1428571
RhoD											**σ**	34.9499642	30.0154722
Date	20.11.2020										**σ %**	52.9544913	52.5270764
Analyst	FMU												
		Ns/Ni	**FT-age**	**1x st. Dev.**	**2x st. Dev.**	**n(G)**							
		1.155				21					**Max**	170	138
											Min	21	18

#	cT	Ns	Ni	L	B	Area	Grain qualit	comments		Eq. 5.3
1		21	21	5	5	25	f	z		363258
2		42	42	10	5	50	g			726516
3		86	84	10	10	100	f			1028671.62
4		69	54	5	10	50	g	z		514617.366
5		40	35	10	5	50	f	z		3468
6		170	138	10	10	100	g	f		526311.117
7		55	49	10	5	50	f			35224.9615
8		68	61	10	5	50	f	wz		67278.4186
9		57	54	10	10	100	f	i		374100.324
10		105	85	10	5	50	g			353032.105
11		84	55	5	10	50	f	d		4343056.83
12		127	108	10	5	50	g	f		31297.634
13		55	54	10	5	50	g			717581.064
14		28	18	5	5	25	f	f		1627328.35
15		41	28	5	5	25	f	z		1565125.57
16		35	37	5	5	25	f	z		1196604.5
17		53	56	10	5	50	g	fzd		1802277.58
18		71	75	5	10	50	g	z		2407962.33
19		75	81	10	5	50	f	fzd		3178043.31
20		65	46	10	5	50	f	fzd		1827851.68
21		39	19	5	5	25	g	z		7221675.1
22						0				
23						0				
24						0				
25						0			χ^2=	17.9841762
26						0				
27						0			p-value	0.5885
28						0				
29						0				
30						0				
31						0				
32						0				
33						0				
34										
35										
36										
37										
38										
39										
40										

fractures	6
dislocations	4
inclusions	1
wzonation	1
zonations	10

Sample#: **VAH-19**

											Sum	1420	1118
Irradiation:	NoB-29				MINERAL	Apatite							
Mag.	1,25										**Average**	64.5454545	50.8181818
RhoD											**σ**	42.6432904	41.1740052
Date	23.11.2020										**σ %**	66.0670696	81.0221926
Analyst	FMU												
											Max	190	164
											Min	17	10

Ns/Ni	**FT-age**	**1x st. Dev.**	**2x st. Dev.**	**n(G)**
1.2701				22

#	cT	Ns	Ni	L	B	Area	Grain qualit	comments		Eq. 5.3
1		139	130	10	10	100	g	wz d		3169231.24
2		85	65	5	10	50	g	zfd		49686
3		41	33	5	5	25	g	z		14114.6486
4	*	190	164	10	10	100	g	z d		1182518.64
5		64	32	5	5	25	f	z d		7102464
6		75	83	5	10	50	f			7320760.13
7	*	48	42	5	5	25	f	z	picture taken	396806.4
8	*	52	31	5	10	50	g	f wz		2400740.43
9		42	17	10	5	50	f	d		8823217.9
10		48	28	5	5	25	f	z f		2543700.21
11		25	16	5	5	25	p	z f d		667143.902
12		17	10	5	5	25	f	i wz		855468
13		56	39	5	5	25	f	z		549936.674
14		48	47	10	5	50	f	f		1799808.17
15		58	45	5	10	50	f	i wz		8651.80583
16		36	25	10	5	50	g	z i f		369565.639
17		33	20	5	5	25	f	z		1361283.7
18		38	30	5	5	25	f	zf		197.882353
19		60	41	5	5	25	f	zfdi		777223.762
20		97	77	5	10	50	g	wz d		4593.31034
21		29	18	5	5	25	f	zf		1001852
22		139	125	10	5	50	f	zfd		1849703.05
23						0				
24						0				
25						0				χ^2= 26.612328
26						0				
27						0				p-value 0.1841
28						0				
29						0				
30						0				
31						0				
32						0				
33						0				
34										
35										
36										
37										
38										
39										
40										

fractures	10
dislocations	9
inclusions	4
wzonation	5
zonations	14

Appendix B

Apatite Fission Track Thermal History Models

All thermal history models were modelled using the Software HeFTy 1.9.3 (Ketcham et al., 2007). Left panel shows the final thermal history models (unprocessed). Right panel shows the track length distribution.

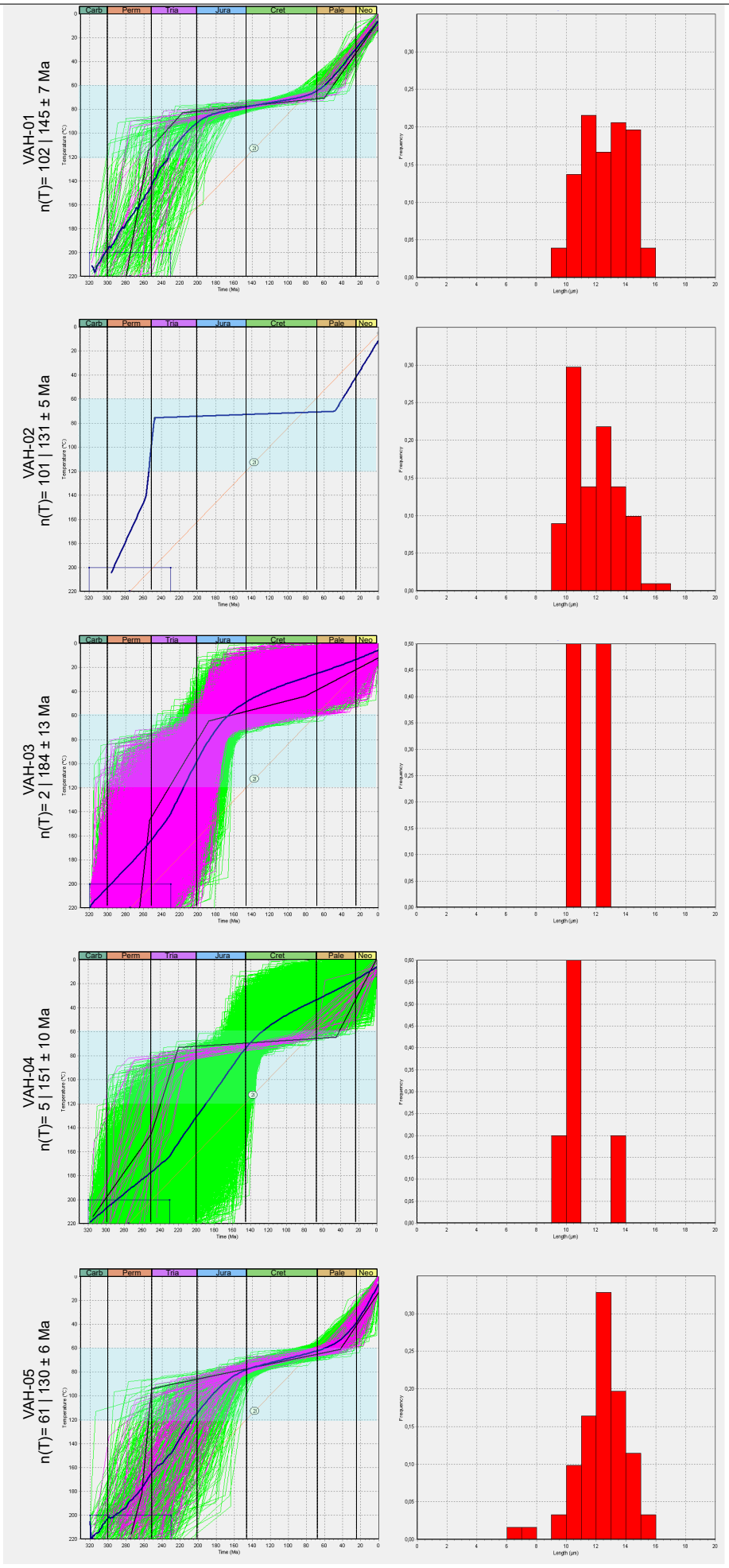
VAH-01
n(T)= 102 | 145 ± 7 Ma
VAH-02
n(T)= 101 | 131 ± 5 Ma
VAH-03
n(T)= 2 | 184 ± 13 Ma
VAH-04
n(T)= 5 | 151 ± 10 Ma
VAH-05
n(T)= 61 | 130 ± 6 Ma
Carb
Perm
Tria
Jura
Cret
Pale
Neo
Time (Ma)
Temperature (°C)
Length (µm)
Frequency

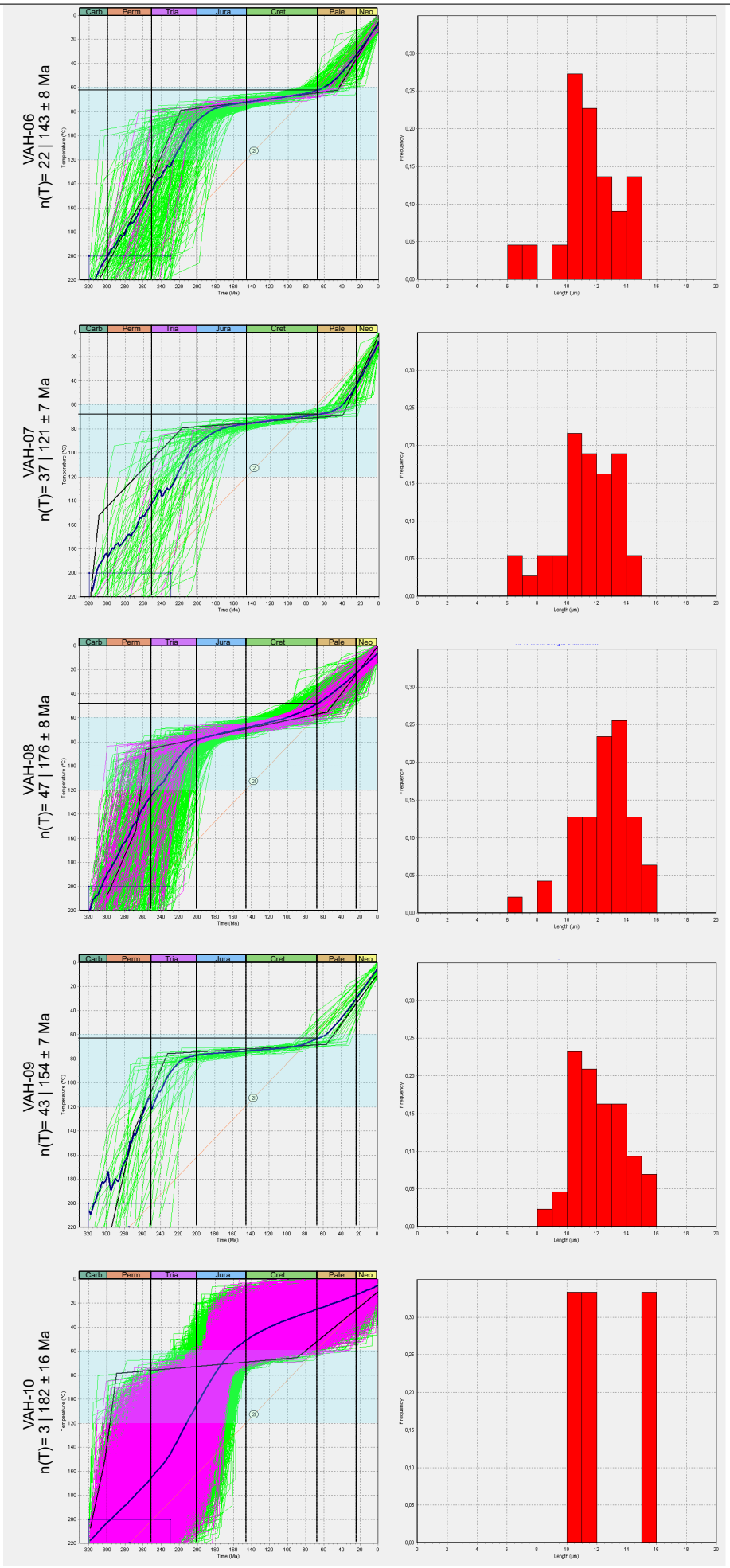
VAH-06
n(T)= 22 | 143 ± 8 Ma
VAH-07
n(T)= 37 | 121 ± 7 Ma
VAH-08
n(T)= 47 | 176 ± 8 Ma
VAH-09
n(T)= 43 | 154 ± 7 Ma
VAH-10
n(T)= 3 | 182 ± 16 Ma
Carb
Perm
Tria
Jura
Cret
Pale
Neo
Temperature (°C)
Time (Ma)
Frequency
Length (µm)

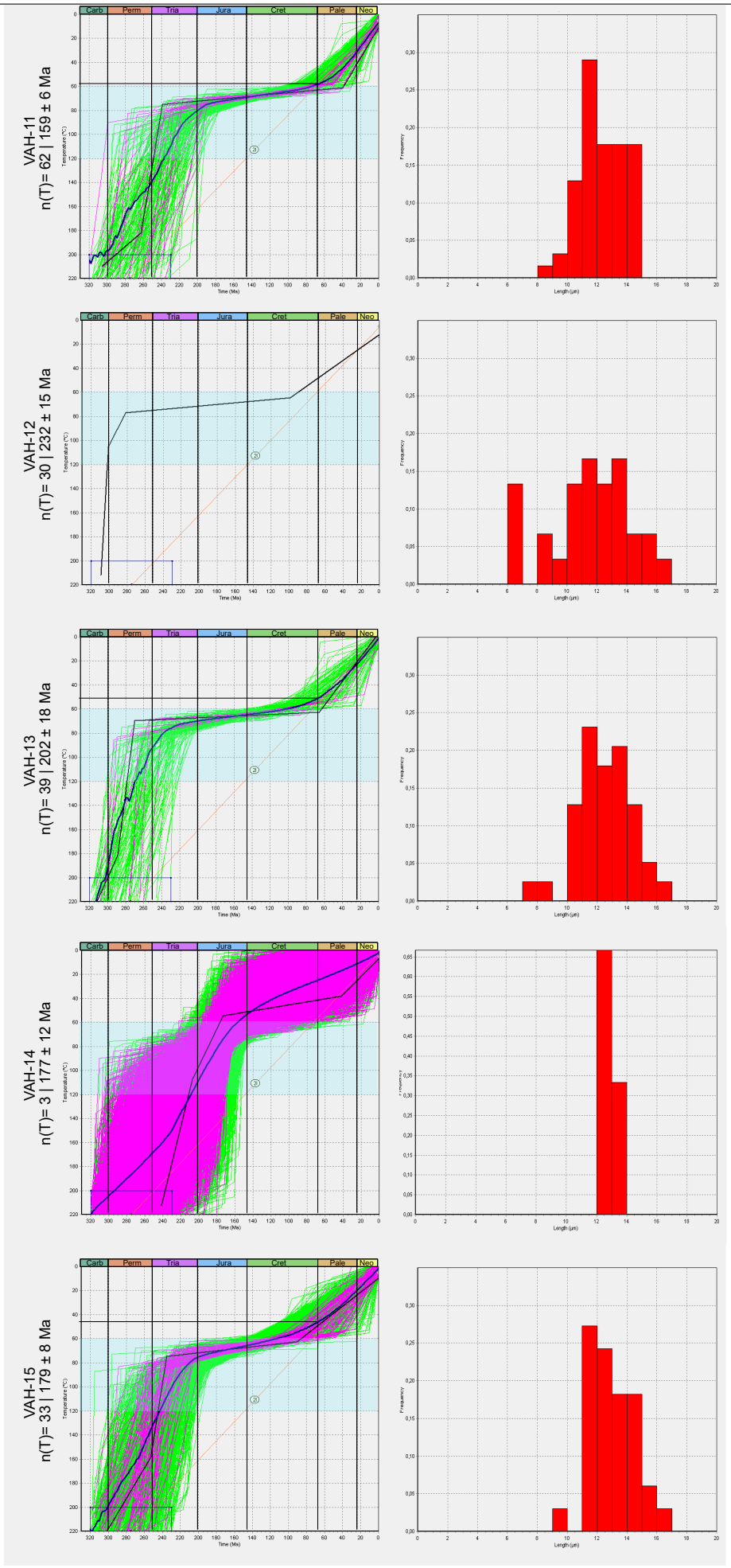
VAH-11
n(T)= 62 | 159 ± 6 Ma
VAH-12
n(T)= 30 | 232 ± 15 Ma
VAH-13
n(T)= 39 | 202 ± 18 Ma
VAH-14
n(T)= 3 | 177 ± 12 Ma
VAH-15
n(T)= 33 | 179 ± 8 Ma
Carb
Perm
Tria
Jura
Cret
Pale
Neo
Temperature (°C)
Time (Ma)
Frequency
Length (µm)

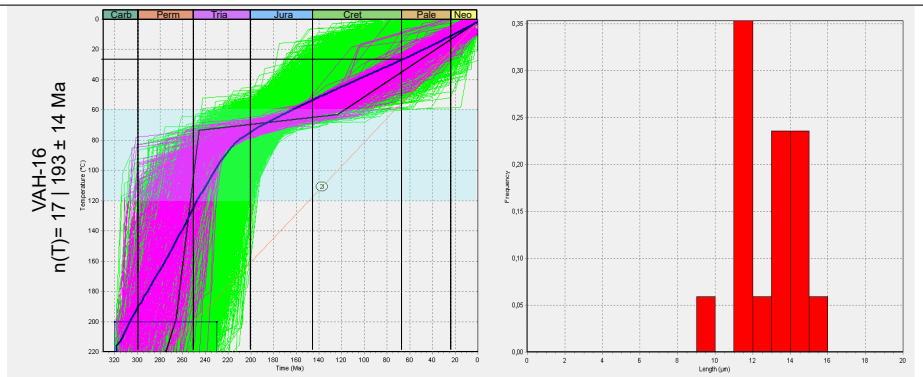
VAH-16
n(T)= 17 | 193 ± 14 Ma
Carb
Perm
Tria
Jura
Cret
Pale
Neo
Time (Ma)
Temperature (°C)
Length (µm)
Frequency

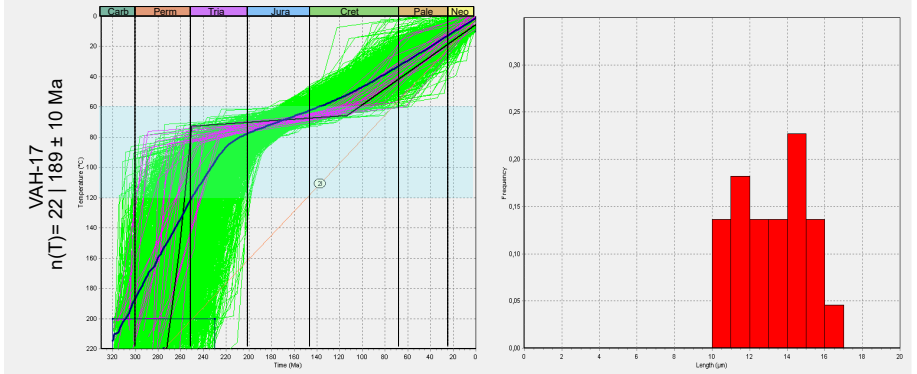
VAH-17
n(T)= 22 | 189 ± 10 Ma
Carb
Perm
Tria
Jura
Cret
Pale
Neo
Time (Ma)
Temperature (°C)
Length (µm)
Frequency

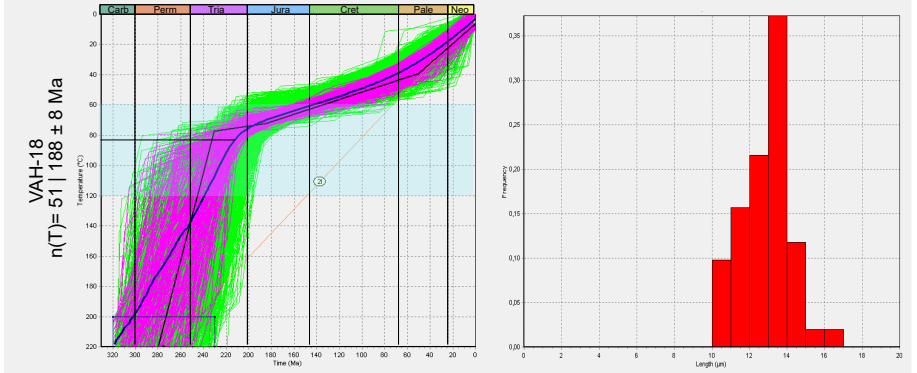
VAH-18
n(T)= 51 | 188 ± 8 Ma
Carb
Perm
Tria
Jura
Cret
Pale
Neo
Time (Ma)
Temperature (°C)
Length (µm)
Frequency

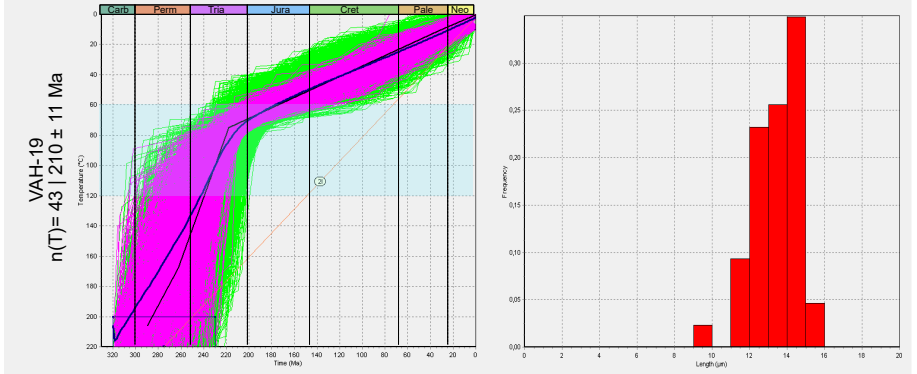
VAH-19
n(T)= 43 | 210 ± 11 Ma
Carb
Perm
Tria
Jura
Cret
Pale
Neo
Time (Ma)
Temperature (°C)
Length (µm)
Frequency

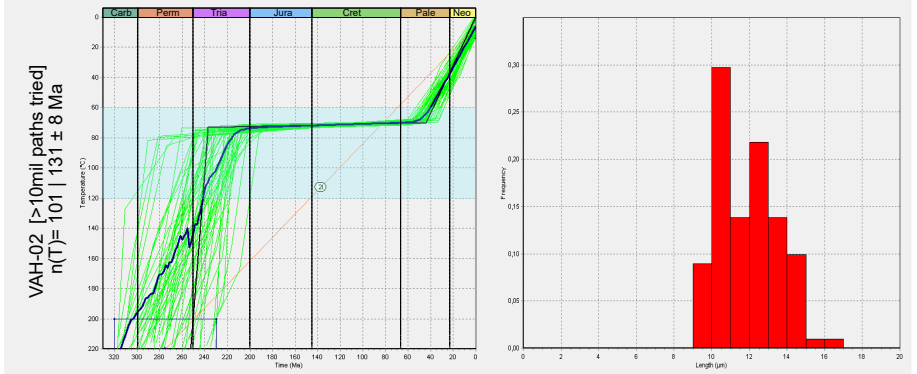
VAH-02 [>10mil paths tried]
n(T)= 101 | 131 ± 8 Ma
Carb
Perm
Tria
Jura
Cret
Pale
Neo
Time (Ma)
Temperature (°C)
Length (µm)
Frequency

Appendix C

Python Code for Isothermal warping

Modelling isotherm warping due to changes in topography - PythonCode

August 17, 2021

[1]:
```
import numpy as np
import pandas as pd
import matplotlib.pyplot as plt
import numpy.random as rnd

T0=5 #surface Temp
k=3 #thermal conductivity, typically between 2.5 and 3.5
pc=2700   #density of crustal rocks
H0=61*10**(-3)  #surface heatflow
qm=31*10**(-3)   #Mantle heatflow
hr=5400   #lower boundary

#depth
vector=np.vectorize(np.float)
z=np.linspace(1,1000,5)
z=vector(z)

T=T0+((qm*z)/k)+((pc*H0*(hr**2))/k)*(1-np.exp(-z/hr))

# plt.plot(T,-z)
```

[2]:
```
Tm=550
zm=35000
C1 = k*Tm/zm
T=C1/k*z+T0

plt.plot(T,-z)
```

[2]:
```
[<matplotlib.lines.Line2D at 0x25d9cb72588>]
```

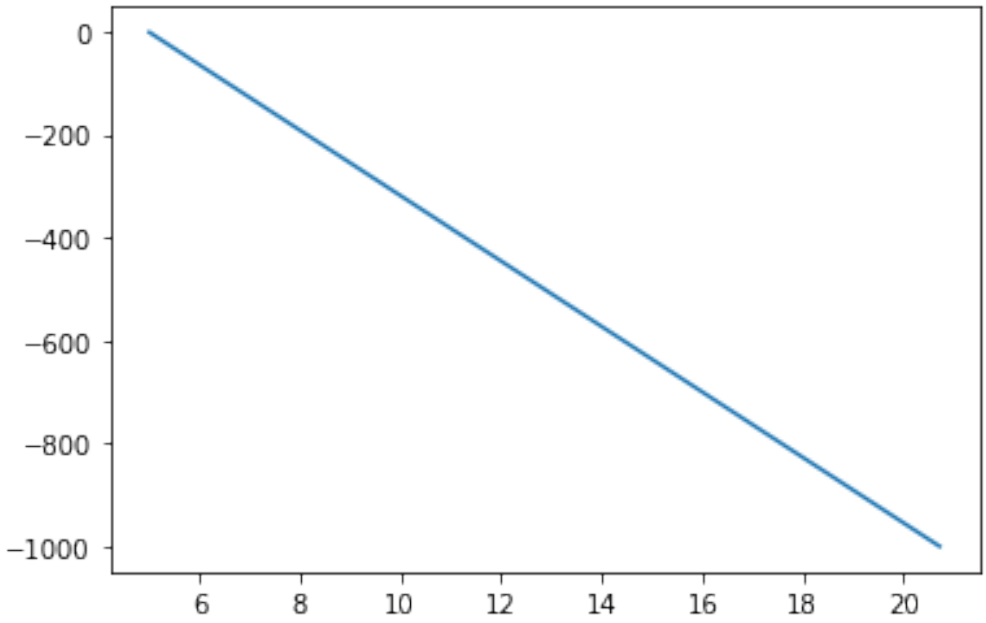

[3]:
```
##numerics
nz=100 #defines vektorlength
z=np.zeros(nz) #creates depth as vektor
temp=np.zeros(nz) #creates temperature

##physics
zm = 10e3 #defines max. depth in m
k = 3 #defines k (Maystrenko et al., 2021)
S = 4e-6 #defines heatproduction (Maystrenko et al., 2015 at 1500m depth)
Tm = 20*zm/1000 #max. Temperature with 20°C/km gradient
C1 = k*Tm/zm + S*zm/2 #defines constant C1

#space coordinate
dz=zm/(nz-1) #defines vektor increments of depth
for i in range(nz):
    z[i]=dz*(i-1) #calculates depth for every increment


##temperature calculation
for i in range(nz):
    temp[i]=-S/(2*k)*z[i]**2 + C1/k*z[i]

plt.plot(temp,-z)
```

[3]:
```
[<matplotlib.lines.Line2D at 0x25d9d2e0848>]
```

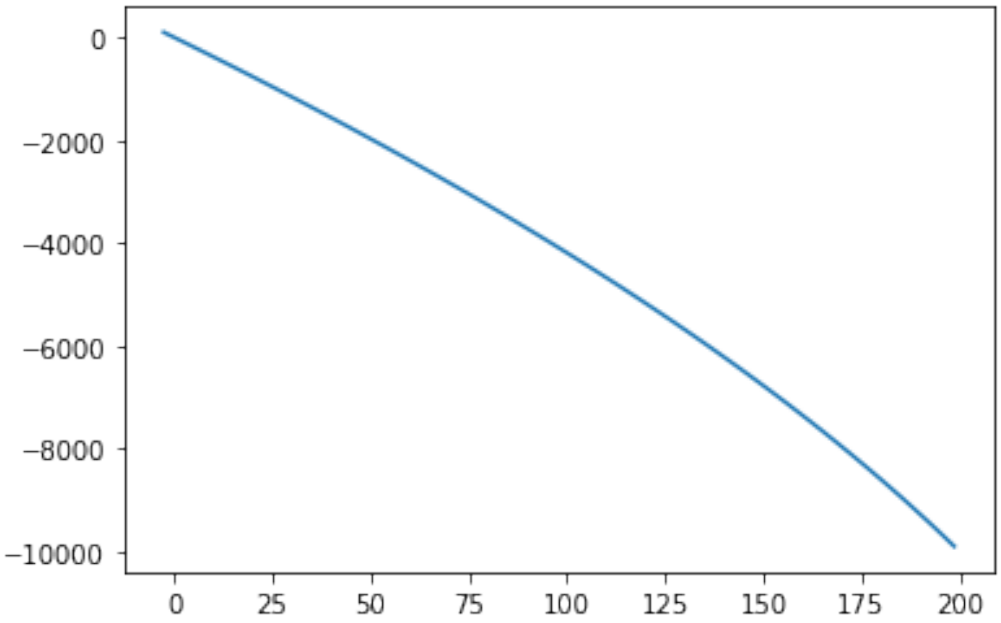

[4]:
```
## samples points
horiz=[0,
497.331,
756.086,
781.342,
1521.125,
2421.213,
3038.641,
3266.648,
3621.022,
3950.181,
4441.583]

depth=[63.29,
233.65,
396.10,
410.39,
716.54,
1078.52,
1395.89,
1494.85,
1553.46,
1690.86,
1840.82
]
trias=np.zeros(np.size(depth))
```

```
cret=np.zeros(np.size(depth))

for i in range (6):
    trias[i]=depth[i]-5000

for i in range (6,11):
    trias[i]=depth[i]-5625

for i in range (np.size(depth)):
    cret[i]=depth[i]-3000
```

[7]:
```
import math

# Triassic

# topo = np.arange(0, 10000, 10)
wav = 6000        #wavelength in m
length = 7200       #lenght of topography in m
topo = np.zeros(length)
A =  750        #amplitude (Gabrielsen et al., 2010, Sömme et al., 2013)

for i in range(length):
    topo[i]  = A*(math.cos((i*2*(math.pi))/wav+1.5))      #Stüwe 2007

##physics
zm = 10e3 #defines max. depth in m
k = 3 #defines k (Maystrenko et al., 2021)
S = 3e-6 #defines heatproduction (Maystrenko et al., 2015; 2021)
Tm = 175 #max. Temperature with 20°C/km gradient
C1 = k*Tm/zm + S*zm/2 #defines constant C1


temp = np.arange(0,150,20)
z = np.zeros((np.size(temp),np.size(topo)))

a=-S/(2*k)
b=C1/k
c=-temp
for h in range (length):
    z[0,h]=-topo[h]

for i in range (1,np.size(temp)):
    for h in range (length):
        z[i,h]=(-b+(b**2-4*a*c[i])**(0.5))/(2*a)
        z[i,h]=z[i,h]-(np.exp(-2*(z[i,h]/wav))*topo[h]) #Stüwe 2007

#plotting datapoints
```

```
plt.figure(num=1, figsize=(6, 6), dpi=160, facecolor='w', edgecolor='k')
# plt.grid(True)
plt.plot(np.arange(-1200,length-1200),topo,linewidth=5)

for i in range (np.size(temp)):
    plt.plot(np.arange(-1200,length-1200),-z[i,:], c='grey',ls='--')

plt.plot(horiz,trias, color='purple',ls=':',marker='o')
plt.xlim(-1200,6000)
plt.ylim(-6000,1200)
# plt.savefig('trias_heatflow.svg')
```

[7]: (-6000, 1200)

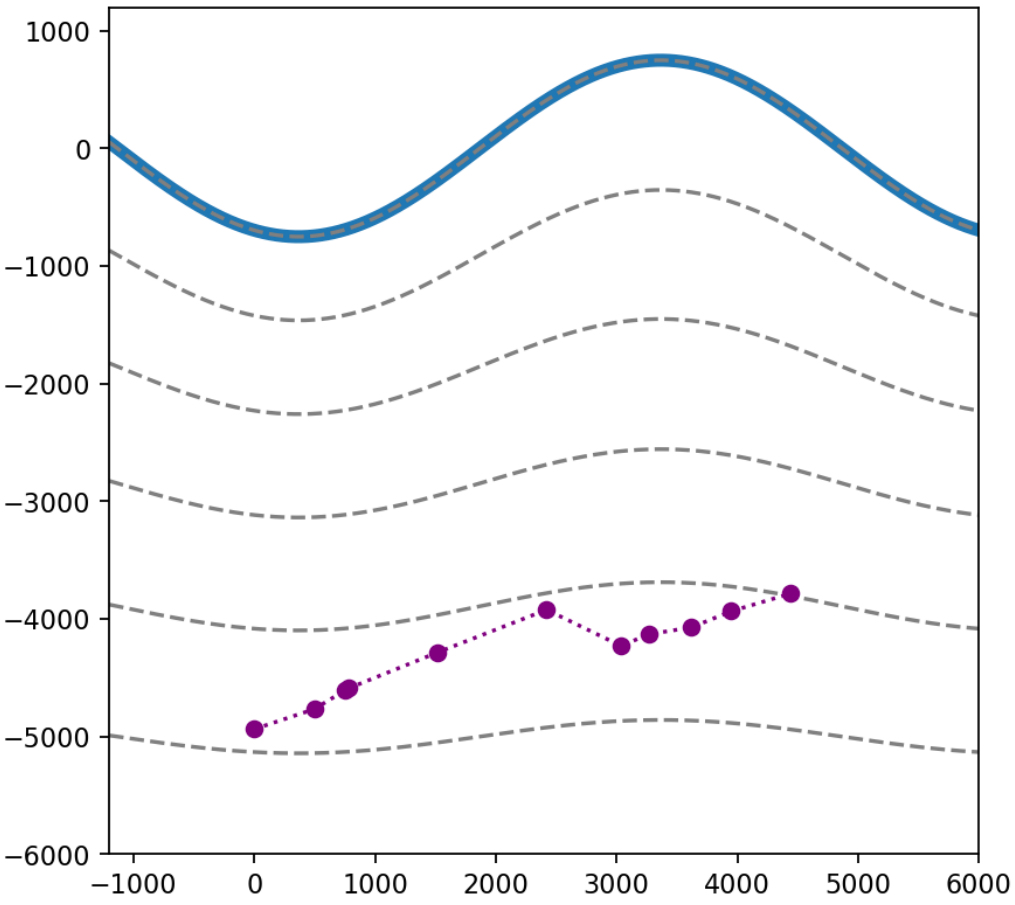

[6]:
```
import math

# Cretaceous
```

```
# topo = np.arange(0, 10000, 10)
wav = 4000        #wavelength in m
length = 7200       #lenght of topography in m
topo = np.zeros(length)
A =  150        #amplitude (Gabrielsen et al., 2010)

for i in range(length):
    topo[i]  = A*(math.cos((i*2*(math.pi))/wav+.5))      #Stüwe 2007

##physics
zm = 10e3 #defines max. depth in m
k = 3 #defines k (Maystrenko et al., 2021)
S = 3e-6 #defines heatproduction (Maystrenko et al., 2015; 2021)
Tm = 175 #max. Temperature with 20°C/km gradient
C1 = k*Tm/zm + S*zm/2 #defines constant C1


temp = np.arange(0,150,20)
z = np.zeros((np.size(temp),np.size(topo)))

a=-S/(2*k)
b=C1/k
c=-temp
for h in range (length):
    z[0,h]=-topo[h]

for i in range (1,np.size(temp)):
    for h in range (length):
        z[i,h]=(-b+(b**2-4*a*c[i])**(0.5))/(2*a)
        z[i,h]=z[i,h]-(np.exp(-2*(z[i,h]/wav))*topo[h]) #Stüwe 2007

#plotting datapoints
plt.figure(num=1, figsize=(6, 6), dpi=160, facecolor='w', edgecolor='k')
# plt.grid(True)
plt.plot(np.arange(-1200,length-1200),topo,linewidth=5)

for i in range (np.size(temp)):
    plt.plot(np.arange(-1200,length-1200),-z[i,:], c='grey',ls='--')

plt.plot(horiz,cret, color='orange',ls=':',marker='o')
plt.xlim(-1200,6000)
plt.ylim(-6000,1200)
# plt.savefig('cret_heatflow.svg')
```

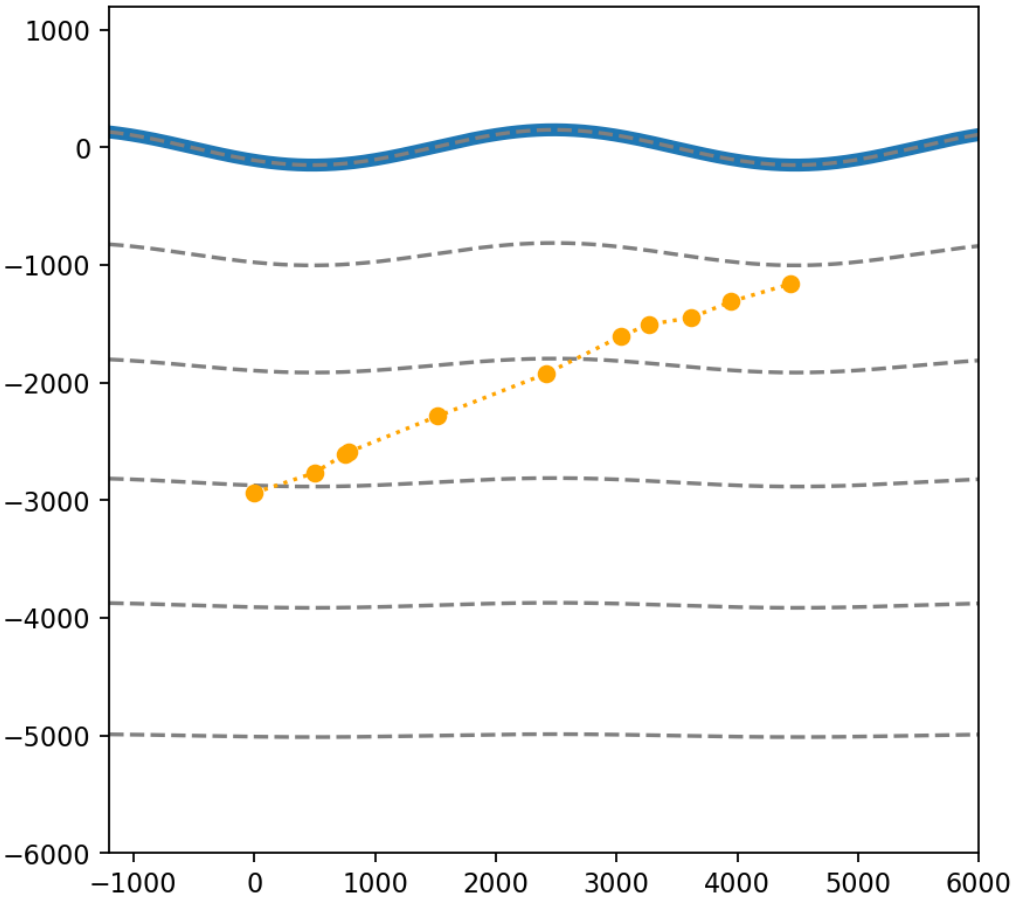
1000
0
−1000
−2000
−3000
−4000
−5000
−6000
−1000
0
1000
2000
3000
4000
5000
6000